TOWARDS HIGH EFFICIENCY AMORPHOUS SILICON SOLAR CELLS

November, 1987

Shinya Tsuda

TOWARDS HIGH EFFICIENCY AMORPHOUS SILICON SOLAR CELLS

Shinya Tsuda

DOC
1988
5
電気系

ABSTRACT

This thesis describes photovoltaic characteristics and reliability of hydrogenated amorphous silicon (a-Si) solar cells. The main purpose of the present study is to improve performance and reliability through the approaches of fabrication process, materials, and cell structures.

Concerning the fabrication process, a separated ultra-high vacuum (UHV) reaction chamber system, called the super chamber, has been newly developed to reduce impurities in a-Si films. A background pressure of 10^{-9} Torr was obtained, and an oxygen concentration of 2×10^{18} cm^{-3} was achieved, which is one to two orders of magnitude lower than in conventional chambers. It was found that film properties of a-Si, such as space charge density, ESR spin density, carrier diffusion length, and so on, can be improved by impurity reduction with the super chamber method. A conversion efficiency of 11.7 % was achieved for a pin type a-Si solar cell whose i-layer was prepared by the super chamber method.

As for materials, super structure a-SiC/a-Si films were fabricated by the photo-CVD method for the first time, as a high-quality wide-bandgap material which improves the short-wavelength collection efficiency. The quantization effect was observed in the dependence of the optical properties on the thickness of the well layer. The superiority of the photo-CVD method as a fabrication method for a-Si super structure films was shown. About a 30 % increase in the collection efficiency in the short-wavelength region was achieved for a pin a-Si solar cell whose p-layer was of the a-SiC/a-Si super structure.

Also concerning materials, hydrogenated-and-fluorinated amorphous silicon germanium (a-SiGe:H:F) was systematically investigated as a high-quality narrow-bandgap material which improves the collection efficiency

in the long-wavelength region. Microcrystalline (μc) Ge and Si were obtained with a certain reaction condition. Improvements were achieved in a-SiGe Schottky diode characteristics and in long-wavelength collection efficiency of a pin a-Si solar cell by optimizing the reaction conditions of a-SiGe:H:F.

As for cell structures, theoretical considerations were made on amorphous solar cells for the purposes of improving efficiency and evaluating the theoretical efficiency. In the case of conventional single-bandgap amorphous cells, the theoretical efficiency was estimated to be less than 15 %. In the case of multi-bandgap cells, which combine a wide-bandgap material and a narrow-bandgap material, however, it was estimated to be 21 % to 24 %. In order to realize high-efficiency multi-bandgap cells, material considerations were also made, including the new materials mentioned before.

With regard to reliability, light-induced degradation of a-Si solar cells was systematically investigated. Carrier recombination and impurities were found to be key factors of the degradation. In order to minimize the carrier recombination, a stacked type cell structure, such as a multi-bandgap structure, is effective because its thin i-layer causes a strong inner electric field. To minimize impurities, the super chamber method is clearly suitable.

Therefore, as a future solar cell, a high-efficiency and stable amorphous solar cell will be achieved with the multi-bandgap structure and the super chamber method.

ACKNOWLEDGEMENT

The author wishes to express his sincere gratitude to Professor Hiroyuki Matsunami for his kind guidance and hearty encouragement. He is grateful to Professor Akira Kawabata for his useful suggestions and constructive criticism of the manuscript. He also acknowledges Professor Shigeo Fujita for a critical reading of the manuscript and valuable comments.

This work has been done in the Functional Material Research Center of Sanyo Electric Co., Ltd., and supported in part by the Agency of Industrial Science and Technology, and also in part by the New Energy Development Organization (NEDO), both as a part of the Sunshine Project under the Ministry of International Trade and Industry.

The author would like to express his deep gratitude to Dr. M. Yamano, senior executive vice president of Sanyo Electric Co., Ltd., Dr. S. Oh-hara, executive director of the research and development headquarter, Dr. Y. Kuwano, the general manager of the Functional Material Research Center, T. Yazaki, the general manager of the AV Research Center, and Dr. S. Nakano, the manager of Thin Film Material Laboratory of the Functional Material Research Center, for their continuous support and advice. He is also grateful to Dr. Y. Nagata, the former general manager of the Applied Research Center, and Mr. M. Ohnishi, the manager of the Functional Material Research Center for their guidance and encouragement.

The author wishes to express his thanks to Messrs. Y. Nakashima, T. Takahama and M. Isomura concerning the super chamber, to Messrs. H. Tarui and T. Matsuyama concerning the super structure, to Messrs. H. Tarui, H. Haku, Y. Hishikawa and H. Dohjo concerning the a-SiGe:H:F films, and to

Messrs. N. Nakamura, M. Nishikuni and T. Takahama concerning the light-induced effect. He is grateful to all other research members of the amorphous silicon solar cell group of Sanyo Electric Co., Ltd. In particular, the author takes pleasure in acknowledging the hearty encouragement and continuous support by Drs. Y. Kuwano and S. Nakano.

CONTENTS

ABSTRACT

ACKNOWLEDGEMENT

Page

I. INTRODUCTION 1

1-1. Historical Background of Amorphous Silicon Solar Cells 1

1-2. Purpose and Significance of Present Work 4

References 7

II. PREPARATION AND PROPERTIES OF A-SI FILMS DEPOSITED WITH SUPER CHAMBER (SEPARATED ULTRA-HIGH VACUUM REACTION CHAMBER) 9

2-1. Introduction 9

2-2. Preparation Method and Impurity Concentrations 10

2-2-1. Preparation method 10

2-2-2. Impurity concentrations 15

2-3. Properties of a-Si Films Deposited in Super Chamber 15

2-3-1. Defect density near midgap 15

2-3-2. Defect density near tail states 18

2-3-3. Electrical properties 21

2-3-4. Discussion on film properties 24

2-4. Application to Solar Cells 24

2-5. Summary 26

References 28

III. SUPER STRUCTURE A-SI FILMS AS WIDE-BANDGAP MATERIALS FOR SOLAR CELLS 29

3-1. Introduction 29

3-2. Preparation and Structural Analysis 30

3-2-1. Preparation method and reaction condition 30

3-2-2. Structural analysis 30

3-3. Optical Properties of Super Structure Films 32

3-3-1. Optical bandgap 32

3-3-2. Photoluminescence 35

3-4. Comparison of Preparation Method 37

3-5. Electrical Properties Vertical to Interfaces 39

3-6. Application to Solar Cells 41

3-7. Summary 44

References 47

IV. A-SIGE:H:F FILMS AS NARROW-BANDGAP MATERIALS FOR SOLAR CELLS 48

4-1. Introduction 48

4-2. Preparation 48

4-3. Film Properties 49

4-3-1. GeF_4 Flow rate dependence 52

4-3-2. RF power dependence 55

4-3-3. Substrate temperature dependence 55

4-3-4. Discussion on film properties 57

4-4. Device Characteristics 59

4-4-1. I-V characteristics of Schottky diodes 59

4-4-2. Collection efficiency spectra of pin diodes 61

4-5. Summary 63

References 64

V. THEORETICAL ANALYSIS OF MULTI-BANDGAP A-SI SOLAR CELLS 65

5-1. Introduction 65

5-2. Calculation of Theoretical Conversion Efficiency for a-Si Solar Cell 65
5-2-1. Equivalent circuit 66
5-2-2. Sequence of calculation 68
5-2-3. Gap state distribution function 68
5-2-4. Poisson's equation 73
5-2-5. Continuity equation for minority carriers 76
5-2-6. Results of calculation 78
5-3. Calculation of Theoretical Conversion Efficiency for Single-Bandgap Amorphous Solar Cells 79
5-4. Calculation of Theoretical Conversion Efficiency for Multi-bandgap Amorphous Solar Cells 84
5-4-1. Cell structures 84
5-4-2. Calculation method 85
5-4-3. Optimization of each bandgap 87
5-5. Realization of Multi-bandgap Amorphous Solar Cells 89
5-5-1. Material consideration 89
5-5-2. Discussion 93
5-6. Summary 93
References 96

VI. STUDY ON LIGHT-INDUCED EFFECTS OF A-SI SOLAR CELLS 97
6-1. Introduction 97
6-2. Reliability of a-Si Solar Panels 97
6-2-1. Preparation 97
6-2-2. a-Si solar cell modules and panels 98
6-2-3. Environmental tests 98

6-2-4. Light-induced degradation in a-Si power generating system 100

6-3. Analysis of Light-Induced Degradation in a-Si Solar Cells ..104

6-4. Effect of Impurities 114

6-5. Summary 119

References 120

VII. CONCLUSIONS 121

APPENDIX A FERMI INTEGRAL 125

APPENDIX B STEP-BY-STEP METHOD 127

APPENDIX C SOLUTION OF CONTINUITY EQUATION 128

APPENDIX D EXPLANATION OF PHOTOCURRENTS 131

APPENDIX E NEWTON METHOD FOR CALCULATION OF I-V CHARACTERISTICS ..132

LIST OF PUBLICATIONS 133

I. INTRODUCTION

1-1. Historical Background of Amorphous Silicon Solar Cells

A photovoltaic effect was first observed in 1839 by a French physicist, Becquerel. He noted that voltage appeared when one of two identical electrodes in a weak conducting solution was illuminated. The photovoltaic effect in solids was first studied in 1877 by Adams and Day with a selenium cell. But selenium photovoltaic cells exhibited only 1 % efficiency in converting light to electricity, and they did not become practical as an energy converter.

In 1954, the first solar cell using crystalline silicon (c-Si) was developed by Chapin, Fuller, and Pearson of Bell Telephone Laboratories,[1] and a conversion efficiency of 6 % was soon obtained. In 1958, the U.S. Vanguard space satellite used c-Si solar cells to power its radio. The cells worked so well that solar cells were soon realized as an effective power source in space. As for terrestrial applications of solar cells, numerous schemes have been tried for 30 years to use them commercially. This is because solar energy for photovoltaic conversion into electricity is abundant, clean, and distributed relatively homogeneously compared with oil resources. Solar cells themselves require no fuel, and therefore, there is no pollution from exhaust gases. In addition, as solar cells do not have moving parts, they are silent in operation, and their lifetime is long.

The c-Si solar cell is the most popular cell at present, but the cost is so high that it cannot compete with conventional energy sources such as thermal-power generation. The main reason for the expensiveness of c-Si solar cells comes from their fabrication process. High temperature is required in the process of crystal growth and junction

formation. The necessity of slicing and polishing causes loss of materials. Therefore, expensive c-Si solar cells were utilized in restricted applications, such as satellites, lighthouses, and so on.

On the other hand, an impact in the field of semiconductor materials was made by Spear and LeComber of Dundee University in 1975. They succeeded in valency control of hydrogenated amorphous silicon (a-Si) deposited by a glow discharge method with silane (SiH_4).[2) As amorphous materials have no long-range ordering in their atomic arrangement, they possess redundancy in physical properties. This redundancy allows us to fabricate amorphous materials having tailor-made optical and electrical properties. But amorphous materials have a weak point of difficulty in the valency control because of a large density of gap states. This weak point was eliminated by the work of Spear and LeComber. They showed that the gap state density in their a-Si was reduced to the order of 10^{17} $eV^{-1}cm^{-3}$ at the midgap, which was two to three orders of magnitude lower than the previous a-Si deposited by evaporation methods. The reason for the decrease in the gap states was soon discovered that hydrogen atoms eliminated dangling bonds in a-Si deposited by the glow discharge method.

In 1976, the first a-Si solar cell was developed by Carlson and Wronski of RCA.[3) Compared with the c-Si solar cell, the a-Si solar cell has several characteristic features. Namely, the fabrication process is simple; the deposition temperature is low; the amount of required material is few because of a high optical absorption coefficient of a-Si, low-cost substrates can be utilized; and enlargement of the cell area is easy. The future cost of the a-Si solar cell is, therefore, thought to be considerably low, and the a-Si solar cell becomes the most hopeful candidate as low-cost solar cells for power generating systems.

After the development of a-Si solar cells, there have been several

important investigations on fabrication process, materials, and cell structures.

As for the depisition process, DC glow discharge[4] and RF glow discharge[5] were investigated at the initial stage, and the RF glow discharge method became the major preparation method. In 1970's, all deposition apparatus were based on single-chamber configuration, which had a problem of intermixing of impurities, resulting in deterioration of film quality. Then, a consecutive separated reaction chamber, which can reduce intermixing of impurities, was developed by Kuwano, Tsuda, et al. in 1982,[6] and photochemical vapour deposition (photo-CVD) was utilized as a fabrication process for a-Si solar cells by Saitoh et al.[7] and Inoue et al.[8] in 1983.

In addition to a-Si, various kinds of hydrogenated a-Si alloy materials, such as hydrogenated amorphous silicon carbide (a-SiC),[9] hydrogenated amorphous silicon nitride (a-SiN),[10] hydrogenated amorphous silicon germanium (a-SiGe),[11] and hydrogenated amorphous silicon tin (a-SiSn),[12] were studied. In 1980, a-SiGe was applied as an i-layer of a pin a-Si solar cell by Nakamura et al.,[11] and a-SiC was applied as a p-layer by Tawada et al. in 1982.[13]

Concerning the cell structures, various configurations, such as Schottky,[3] pin,[3] inverted pin,[14] MIS[15] and stacked types,[16] have been investigated. Now, the pin type cell structure is most widely utilized. In addition, integrated type cell structures, which connect with each cell in series on one substrate to generate high output voltage, have been developed by Kuwano, Tsuda, et al.[17]

With various innovations including the above mentioned studies, the conversion efficiency of a-Si solar cells was rapidly increased, and in application to consumer electronics, the a-Si solar cell is widly used

compared with the c-Si solar cell.[18)]

As for applying a-Si solar cells to power generating systems, the conversion efficiency is, however, almost half of that of c-Si solar cells, so c-Si solar cells have been mainly utilized. Therefore, improvements in the conversion efficiency of the a-Si solar cell are strongly required for its wide-spread use in power applications.

Staebler and Wronski also reported on light-induced degradation of electrical conductivity of a-Si films,[19)] caused by changes in the mobility-lifetime ($\mu\tau$) product and the position of the Fermi level after light exposure. Thus, reliability of a-Si solar cell characteristics, which is influenced by the $\mu\tau$ product and the position of the Fermi level, became a large problem for a-Si solar cells in outdoor use. Numerous research efforts have been conducted to investigate the origin of this light-induced degradation,[20-23)] but it is not yet clear, and effective countermeasures are not established at present. Development of the effective countermeasures with revelation of the origin of the light-induced effect is also a key factor for the application of the a-Si solar cells to power generating systems.

1-2. Purpose and Significance of Present Work

In order to apply a-Si solar cells as power sources, the improvement of the conversion efficiency is very much required. For this purpose, systematic investigations must be carried out with regard to three approaches: fabrication process, materials, and cell structure. In the fabrication process, deposition methods for high-quality a-Si films have to be improved, because a-Si films deposited by conventional methods have large defect density resulting in large carrier recombination and poor photovoltaic characteristics. Concerning materials, both wide-

bandgap and narrow-bandgap materials superior in the film quality to conventional materials must be developed, because the photosensitive wavelength-region of conventional a-Si solar cells is considerably narrow, compared with c-Si solar cells, resulting in low conversion efficiency. As for cell structure, theoretical consideration is required to establish the optimum cell structure with synthesizing the above mentioned improvements in fabrication process and materials.

The second problem in utilizing a-Si solar cells as power sources is to increase their reliability by preventing the light-induced degradation of their properties, as mentioned in the previous section. For this purpose, first, the behavior of the degradation has to be studied, and the origin of the degradation has to be analyzed. Second, based on these investigations, practical countermeasures which are not contradictory to the above mentioned efforts for high efficiency cells must be developed.

The purpose of this work is to carry out systematic investigations for improvements in the conversion efficiency and reliability of a-Si solar cells.

In Chapter II, a new deposition method for high-quality a-Si films, a separated ultra-high vacuum (UHV) reaction chamber called a super chamber, is described. The characteristics of the a-Si films deposited in the super chamber are investigated in detail, and the effect of impurity reduction is discussed.

Chapter III introduces a new material, a super structure a-Si film, in order to obtain superior characteristics to a-SiC alloy films as a window p-layer. The super structure a-Si film was deposited with the photo-CVD method for the first time, and the features of this film are made clear. An increase in the collection efficiency at the short-wavelength region is discussed for the new cell structure, an a-Si solar

cell with a super structure p-layer.

In Chapter IV, a narrow-bandgap material is systematically studied. This material, which widens the spectral sensitivity of a-Si solar cells, is fluorinated-and-hydrogenated amorphous silicon germanium (a-SiGe:H:F). The first observation of microcrystalline structure in a-SiGe:H:F films is described, and a high collection efficiency in the long-wavelength region is reported with an a-SiGe:H:F solar cell.

In Chapter V, a theoretical consideration for future a-Si solar cells is also carried out with multi-bandgap structures. Considering various characteristic properties of a-Si and related materials, the optimization of the bandgap is described.

In Chapter VI, some considerations on the origin of and countermeasures for light-induced degradation are discussed. The correlation between cell parameters and degradation behavior is discussed, and some effective methods to reduce the degradation are mentioned.

Finally, conclusions of the present study are made in Chapter VII.

References

1) D. M. Chapin, C. S. Fuller and G. L. Pearson : J. Appl. Phys., 25 (1954) 676.
2) W. E. Spear and P. G. LeComber : Solid State Comm. 17 (1975) 1193.
3) D. E. Carlson and C. R. Wronski : Appl. Phys. Lett. 28 (1976) 671.
4) D. E. Carlson and C. R. Wronski : J. Electron Mat. 6 (1977) 95.
5) J. C. Knights : Phil. Mag. 34 (1976) 663.
6) Y. Kuwano, M. Ohnishi, S. Tsuda, Y. Nakashima and N. Nakamura : Jpn. J. Appl. Phys. 21 (1982) 413.
7) T. Saitoh, S. Muramatsu, T. Shimada and M. Migitaka : Appl. Phys. Lett. 42 (1983) 678.
8) T. Inoue, M. Konagai and K. Takahashi : Appl. Phys. Lett. 43 (1983) 774.
9) D. A. Anderson and W. E. Spear : Philos. Mag. 35 (1977) 1.
10) H. Kurata, M. Hirose and Y. Osaka : Jpn. J. Appl. Phys. 20 (1981) L 811.
11) G. Nakamura, K. Sato, Y. Yukimoto and K. Shirahata : Proc. 3rd E. C. Photovoltaic Solar Energy Conf. (1980) 835.
12) S. Tsuda, H. Tarui, M. Ohnishi, S. Sakai, K. Uchihashi, T. Matsuoka, S. Nakano, S. Kiyama, H. Kawada and Y. Kuwano : J. Non-Crst. Solids 59 & 60 (1983) 1135.
13) Y. Tawada, K. Tsuge, H. Okamoto and Y. Hamakawa : J. Appl. Phys. 53 (1982) 5273.
14) D. E. Carlson : J. Non-Cryst. Solids 35&36 (1980) 707.
15) C. R. Wronski : Jpn. J. Appl. Phys. 17 (1978) Suppl. 17-1, p.299.
16) Y. Hamakawa, H. Okamoto and Y. Nitta : Appl. Phys. Lett. 35 (1979) 187.

17) Y. Kuwano, S. Tsuda, M. Ohnishi and T. Imai : Jpn. J. Appl. Phys. 20 (1981) Suppl. 20-2, p.213.

18) Y. Kuwano : Symposia Proc. Material Research Society 1986 Spring Meeting, Palo Alto (1986) p.455.

19) D. L. Staebler and C. R. Wronski : Appl. Phys. Lett. 31 (1977) 292.

20) D. L. Staebler, R. Crandall and R. Williams : Appl. Phys. Lett. 39 (1981) 733.

21) H. Okushi, M. Itoh, T. Okuno, Y. Hosokawa, S. Yamasaki and K. Tanaka : Proc. Int. Conf. Optical Effects in Amorphous Semiconducters, Snowbird, Utah (1984) p.251.

22) S. Tsuda, N. Nakamura, K. Watanabe, M. Nishikuni, M. Ohnishi, S. Nakano, Y. Kishi, H. Shibuya and Y. Kuwano : Tech. Digest Int. PVSEC-1, Kobe, Japan (1984) p.213.

23) M. Stutzmann, W. B. Jackson and C. C. Tsai : Phys. Rev. B32 (1985) 23.

II. PREPARATION AND PROPERTIES OF A-SI FILMS DEPOSITED WITH A SUPER CHAMBER (SEPARATED ULTRA-HIGH VACUUM REACTION CHAMBER)

2-1. Introduction

Hydrogenated amorphous silicon (a-Si) is gathering much attention as a new material for electronic devices such as solar cells, photosensors, photoreceptors, thin film transistors, and so on. In order to improve the performance of these devices, the quality of a-Si films must be improved. In a-Si films deposited by the conventional method, there is a large amount of impurities. For example, the oxygen concentration of the conventional a-Si films ranges from 10^{19} cm^{-3} to 10^{20} cm^{-3}.[1] Recently, impurities such as oxygen and nitrogen were found to cause an increase in the space charge density and the degradation ratio of the photoconductivity by the light-induced effect.[2] Therefore, the reduction of impurities is necessary from the viewpoint of both the fundamental studies of the light-induced effect and the improvement of device performance.

To reduce the impurities in a-Si films, we have developed the consecutive, separated reaction chamber system,[3] and have found that residual impurities can be reduced by using this system. But the impurity concentration in a-Si films deposited in the separated chamber was in the order of 10^{19} cm^{-3}. Tsai et al. reported some limited results, such as impurity concentration and ESR spin density in a-Si, obtained with a single UHV (ultra-high vacuum) reaction chamber.[4] But there has been no report on detailed results for a-Si films with low impurity concentration deposited in a separated UHV reaction chamber. These films are necessary for high quality a-Si devices. Thus a super chamber, based on the separated UHV reaction chamber system, was

developed, and the quality of a-Si film was investigated in detail with the super chamber for the first time.

In this chapter, the features of the super chamber, in which a-Si films of very low impurity concentration can be prepared, are described, and the properties of the a-Si films are reported in detail. The effect of impurity reduction on the light-induced effect is discussed in Chapter VI.

2-2. Preparation Method and Impurity Concentrations

In this section, the details of the super chamber (separated UHV reaction chamber) are described.

2-2-1. Preparation method

In order to achieve ultra-high vacuum, gas-supplying systems, chambers, and pumping systems of the super chamber were designed to reduce gas leakage from outside and out gas from walls as shown in Fig. 2-1. Its pumping systems, chambers, and gas-supplying systems are bakable, and they are entirely separated from each chamber, thus completely avoiding undesirable mixing of residual gases and reaction gases. In conventional chambers, out gas from the internal surface of chamber walls and gas-supplying systems is very large, which mainly causes high impurity concentrations in a-Si films. This is because the internal surface is not smooth and many voids exist in the material of the chambers and the gas-supplying systems, and impurity gas remains on the rough surface and in the voids. In the super chamber, mirror-polished stainless steel was used as the material of the chamber walls and the gas-supplying systems, and the voids in the material were examined by X-ray photographs to reduce them. Furthermore, high-purity

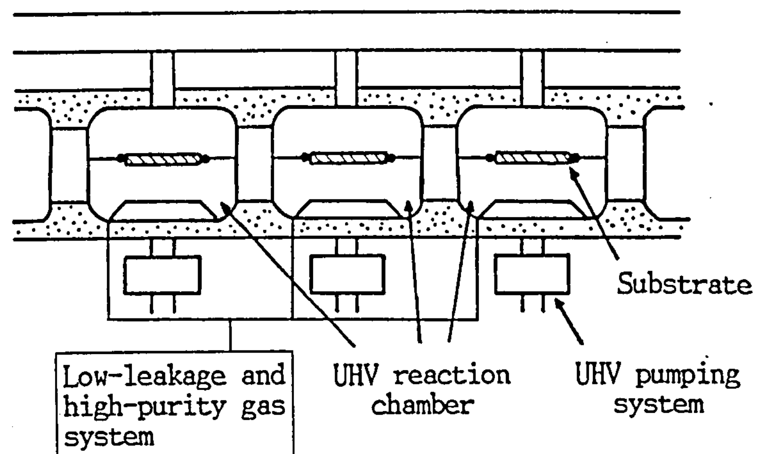

Fig. 2-1 Block diagram of the super chamber (separated UHV reaction chamber).

silane (SiH_4), whose impurity concentration was less than 1 ppm except for hydrogen, was used. Other parts of the super chamber are similar to those of the consecutive separated reaction chamber system.[3] In depositing a-Si films, capacitively-coupled radio frequency (13.56 MHz) glow discharge is used; other reaction conditions shown in Table 2-1 are the same as those in conventional chambers.

Table 2-2 shows background pressure, leakage and out gas in both the super chamber and the conventional separated chamber. The background pressure, and the leakage and out gas in the super chamber were improved from 10^{-6} - 10^{-7} Torr to 10^{-8} - 10^{-9} Torr and from 10^{-5} - 10^{-6} Torr l/sec to 10^{-7} Torr l/sec, respectively, as compared with the conventional separated chamber. It is clear that the super chamber is effective in achieving UHV.

In order to analyze the amount of the residual gases in each chamber, the components of the exhaust gases were measured by a quadrapole GMA (gas mass analyzer, AGA-100, ANELVA). The mass spectra measured by the GMA in each chamber are shown in Fig. 2-2, which are in the case of background pressure (a) and in the case of flowing SiH_4 in the chamber (b). Many peaks appear on the mass spectrum for the conventional chamber in the both cases, for example, H_2, H_2O, CO or N_2, O_2 and CO_2 which have mass numbers of 2, 18, 28, 32 and 44, respectively, and the H_2O peak is especially large. These peaks do not appear in the case of the super chamber. These results suggest that a-Si films deposited in the super chamber may be expected to contain a less amount of impurities, especially oxygen, compared with the a-Si films deposited in a conventional chamber.

Table 2-1 Typical reaction conditions in the super chamber.

Electrode	Parallel type capacitively coupled
RF power	35 mW/cm^2
RF frequency	13.56 MHz
Material gas	SiH_4
Flow rate	5 sccm
Substrate temperature	200°C
Pressure	0.05 Torr

Table 2-2 Comparison of chamber.

	Super chamber	Conventional separated chamber
Back ground pressure (Torr)	$10^{-8}\sim10^{-9}$	$10^{-6}\sim10^{-7}$
Out gas + leakage (Torr·l/s)	$\sim10^{-7}$	$10^{-5}\sim10^{-6}$

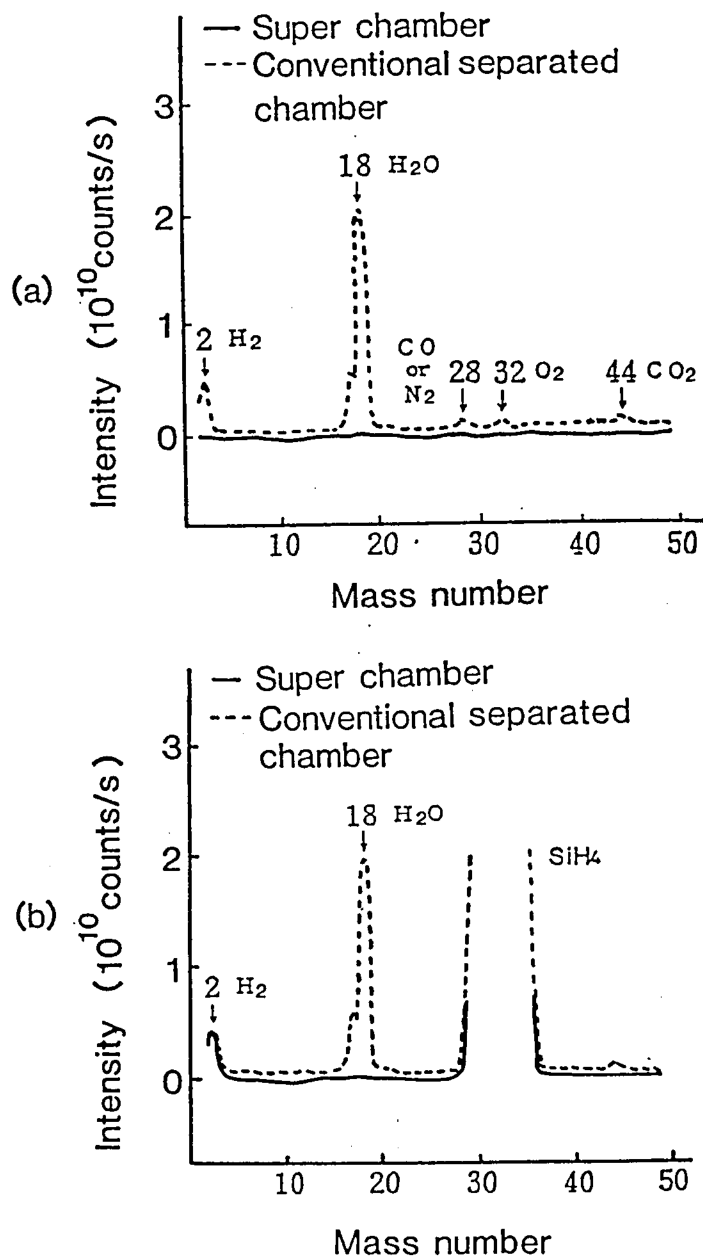

Fig. 2-2 GMA mass spectra of exhaust gases
(a) background (b) flowing SiH_4.

2-2-2. Impurity concentrations

Impurities contained in a-Si films deposited in the super chamber were investigated by IMA (ion microanalyzer) and were compared with those in films deposited in a conventional single chamber and a separated chamber, as shown in Fig. 2-3. The impurity concentrations of oxygen, nitrogen and carbon decreased in the order with the single chamber, conventional separated chamber, and super chamber. The concentrations of oxygen, nitrogen, and carbon were reduced to be 2 x 10^{18} cm^{-3}, 1 x 10^{17} cm^{-3}, and 2 x 10^{18} cm^{-3}, respectively, in the a-Si films deposited in the super chamber. Especially the oxygen concentration in the a-Si films deposited in the super chamber decreased one order of magnitude as compared with the conventional separated chamber.

It is suggested that the decrease in the leakage and out gas contributes to the decrease in the impurity concentrations in a-Si films. Especially, the residual H_2O is thought to be related to the oxygen concentration in a-Si films from the comparison of Fig. 2-2 and Fig. 2-3.

2-3. Properties of a-Si Films Deposited in the Super Chamber

In this section, the properties of a-Si films deposited in the super chamber method are described.

2-3-1. Defect density near the midgap

Figure 2-4 shows the ESR (electron spin resonance) signals measured for a-Si films deposited in the super chamber and in the conventional separated chamber. The a-Si films were deposited on quartz substrates and the thickness was about 1 μ m. The volume of the a-Si films was about 1 x 10^{-3} cm^3. The ESR measurements were carried out at room

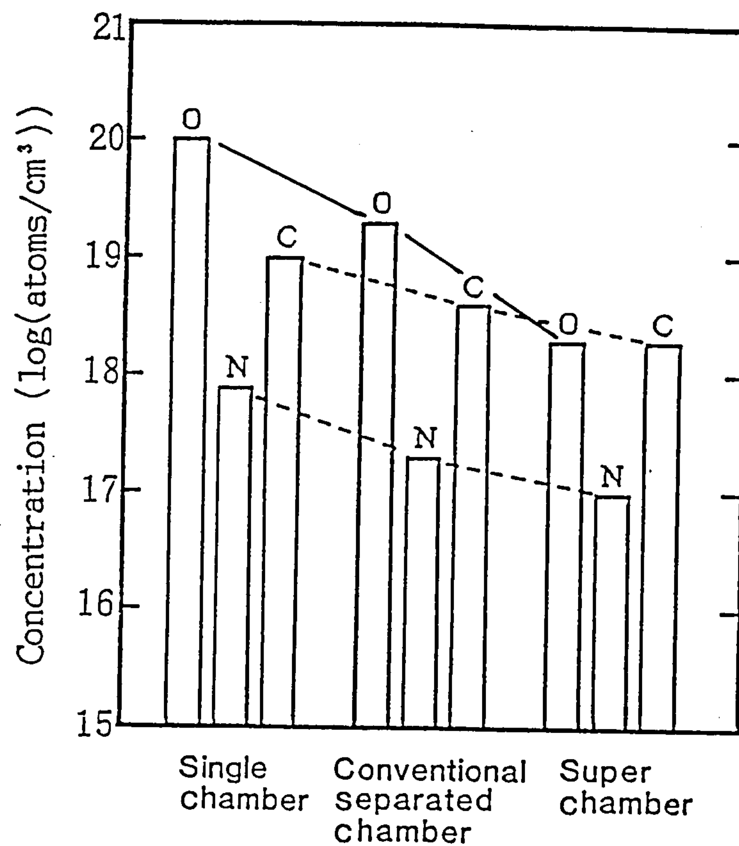

Fig. 2-3 Impurity concentrations in a-Si films deposited in various chambers.

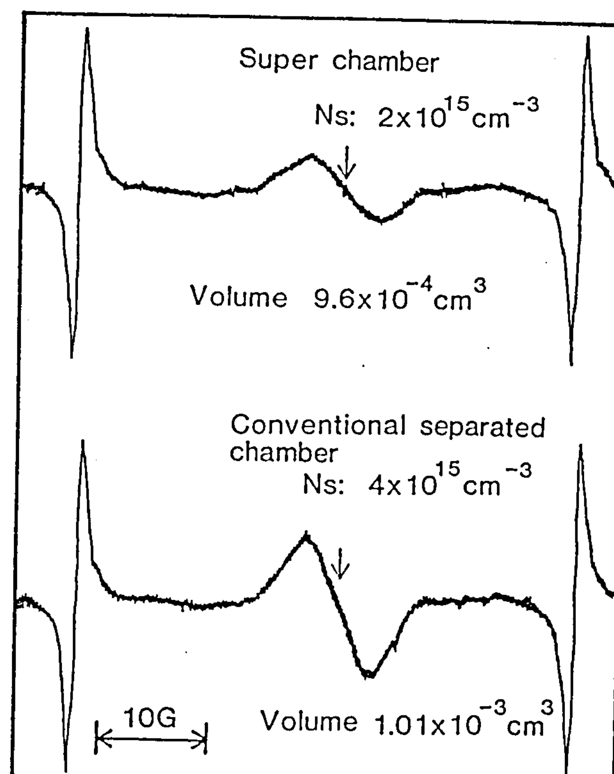

Fig. 2-4 ESR signals of a-Si films deposited in various chambers. The arrows show the middle point of the ESR spectrum corresponds to neutral dangling bonds.

temperature and the microwave frequency was 9 GHz. In Fig. 2-4, the two sharp signals on the both sides of the ESR spectrum were obtained from a standard manganese sample to estimate the ESR spin density and g-value, as a reference. The arrows in Fig. 2-4 show the middle point of the ESR spectrum corresponds to neutral dangling bonds. The ESR spin densities N_s were estimated as 2×10^{15} cm^{-3}, in the case of the super chamber, and 4×10^{15} cm^{-3}, in the case of the conventional separated chamber. The N_s of the a-Si films deposited in the super chamber is the smallest value at present among all previously reported a-Si films.

Figure 2-5 shows the plot of the reciprocal values of the square of capacitance versus bias voltage for Au/i-a-Si/n-c-Si Schottky diodes, where c-Si means crystalline silicon, and the resistivity of c-Si is less than 0.01 Ω cm. The sample structure, measurement conditions, and the measurement circuit are shown in the left part of Fig. 2-5. The thickness of the a-Si film was about 1 μ m, and the modulation frequency was 0.01 Hz. From the slopes of these lines, we can obtain the space charge density N_I which can be expressed by the following equation.

$$\frac{d(1/C^2)}{dV} = \frac{2}{q \varepsilon_0 \varepsilon_r N_I} \qquad (2\text{-}1)$$

In eq. (2-1), q, ε_0, and ε_r are electronic charge, permittivity of vacuum, and relative permittivity of a-Si, respectively. ε_r is assumed to 11.[5] In Fig. 2-5, capacitance C can be obtained as follows. Variation ratio k for voltage can be written as follows,

$$k = \frac{dV}{dt} = 2fV_{pp} \qquad (2\text{-}2)$$

where f and V_{pp} are frequency and peak-to-peak voltage for bias voltage,

respectively. Then C can be obtained as follows,

$$C = \frac{dQ}{dV} = \frac{1}{k} \cdot \frac{dQ}{dt} = \frac{1}{2fVpp} \cdot \frac{\Delta I}{2} = \frac{\Delta I}{4fVpp} \qquad (2\text{-}3)$$

where Δ I means the change in output current.

Reduction of N_I is also effective for improving conversion efficiency. N_I was calculated as 5.1×10^{14} cm^{-3} in the case of the super chamber, and 1.74×10^{15} cm^{-3} in the case of the conventional separated chamber. The value for the super chamber is the smallest for all previously reported undoped a-Si films at present.

As both the N_s and the N_I are related with the density of states near the midgap, these results show that the density of states near the midgap have a relation to impurity concentrations.

2-3-2. Defect density near the tail states

Photoluminescence of a-Si films deposited in the super chamber and the conventional separated chamber was measured at 77 K. The photoluminescence was obtained by excitation with an argon laser operating at a wavelength of 514.5 nm for samples held in liquid nitrogen. The a-Si films were deposited on roughened glass substrates with a thickness of 1 μm to avoid the interference effect. In the case of the super chamber, the peak energy position of the photoluminescence spectrum, close to 1.4 eV, was higher than that in the case of the conventional separated chamber, as shown in Fig. 2-6. As the optical bandgap was the same (1.7 eV) for the both films, the shift of the peak to high energy was thought to indicate a reduction of the density of states near the band tail.

Optical absorption coefficients were measured, including the absorption coefficients for below the bandgap (-1.7 eV) region. They

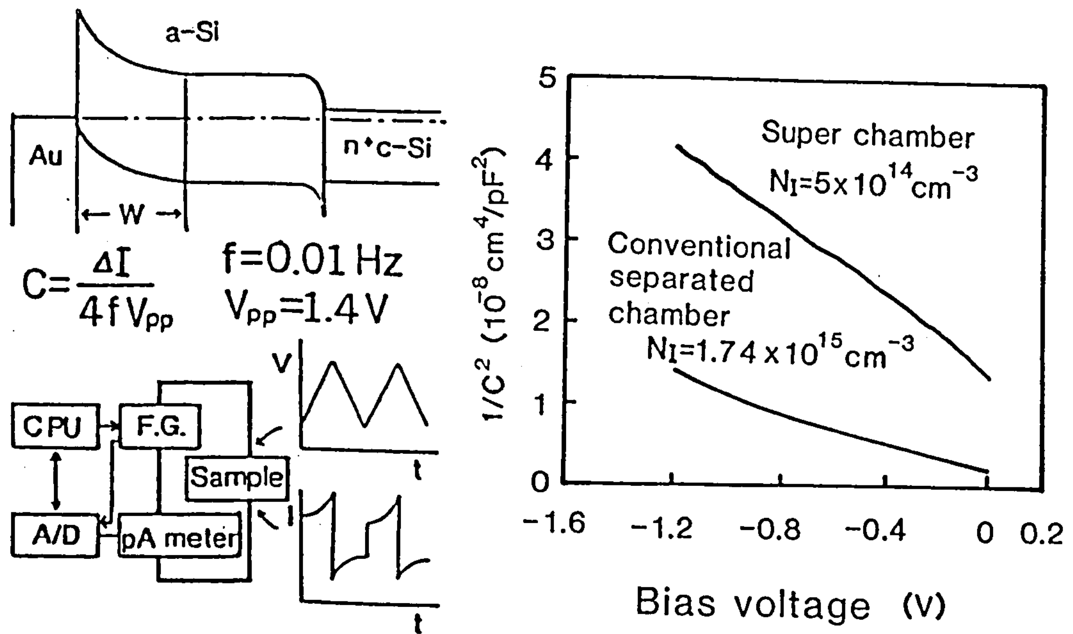

Fig. 2-5 $1/C^2$ versus V plots for estimation of the space charge density N_I.

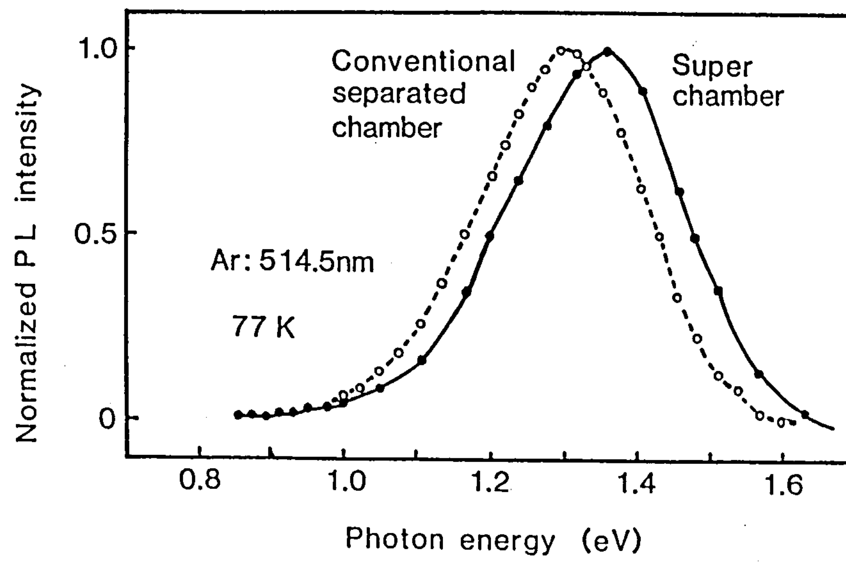

Fig. 2-6 Photoluminescence spectra of a-Si films deposited in various chambers.

were determined by the constant photocurrent method[6], assuming that all absorbed photons are contributes to the observed photocurrent. Co-planar type electrodes were used, and the thickness of the samples was 1 μm. In the case of the super chamber, the optical absorption coefficient below 1.5 eV is smaller than that of the conventional separated chamber, as shown in Fig. 2-7.

These results suggest that the density of tail states also has a possitive correlation with impurity concentrations, and that it can be reduced in the case of a-Si films deposited in the super chamber.

2-3-3. Electrical properties

Electrical properties were also investigated as follows. Figure 2-8 shows dark conductivity (σd) and photoconductivity (σph) of a-Si films deposited in the super chamber as a function of pressure during the deposition. It seemed that the dark and photoconductivities of a-Si films deposited in the super chamber were similar to those of a-Si films deposited in the conventional separated chamber.

Hole diffusion length L of the both a-Si films was estimated by the surface photovoltage method[7], by measuring the correlation between the photovoltage and the optical absorption coefficient α. White bias light of AM-1 100 mW/cm^2 was irradiated during the measurement in order to realize the operating condition as a material for a solar cell. The hole diffusion length of a-Si films deposited in the super chamber was about 1 μm, which was 60 % larger than that of a-Si films deposited in the conventional separated chamber, as shown in Fig. 2-9.

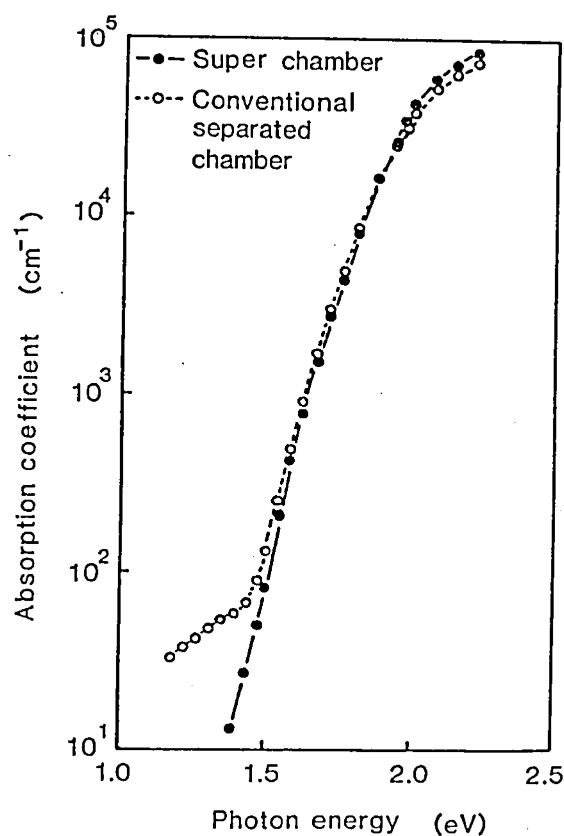

Fig. 2-7 Optical absorption coefficients of a-Si films deposited in various chambers.

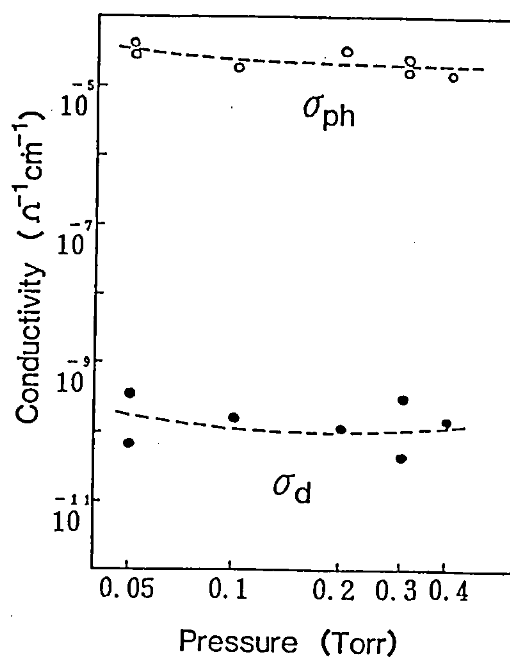

Fig. 2-8 Photoconductivity (σ_{ph}) and dark conductivity (σ_d) of a-Si films deposited in the super chamber as a function of pressure.

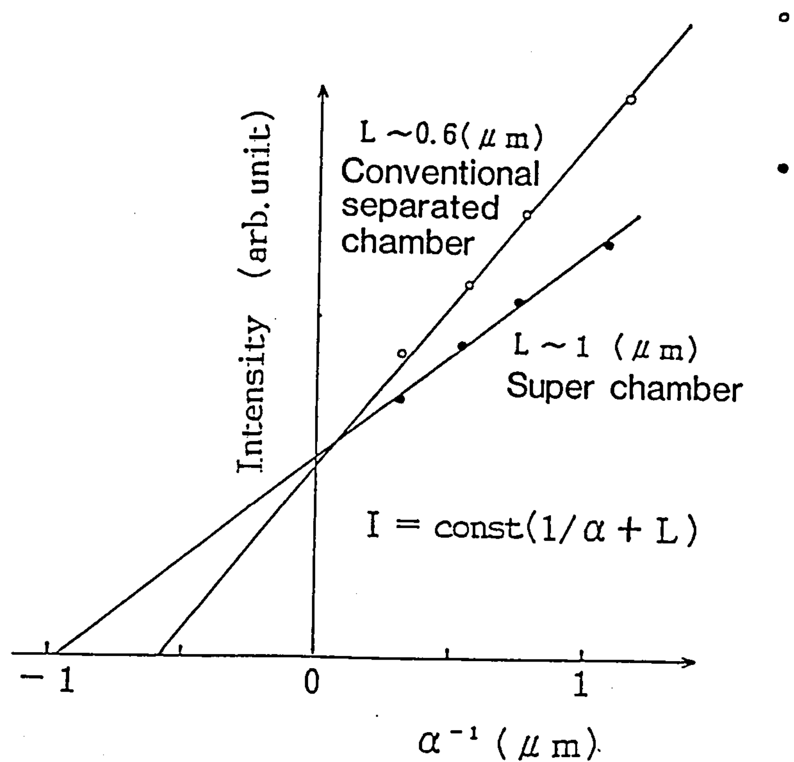

Fig. 2-9 Light intensity versus α^{-1} (α : optical absorption coefficient) plots for estimation of the hole diffusion length L by the surface photovoltage method.

2-3-4. Discussion on film properties

There are several reports on the corelation between the properties of a-Si films and the impurity concentrations in the film.[2,4,8,9] The author reported that the space charge density N_I increased in proportional to the square root of the nitrogen or oxygen concentration in the a-Si films[2] and the detail is discussed in Section 6-4. The reduction of N_I in the a-Si films deposited in the super chamber is also thought to show the same tendency. Namely, the charged states were decreased by the reduction of impurities.

The reason for the reduction of the ESR spin density N_s with decrease in the impurity concentration is not clear. But the incorporation of the impurities is thought to cause the increase in microscopic distortion of the atomic network, which creates a part of dangling bonds. As described in 2-3-2, reduction of the density of tail states, which corresponds to the extent of microscopic disorder, also shows the change in the microscopic distortion with impurities.

As a result, high-quality a-Si films with low density of states and large hole diffusion length were obtained by the super chamber method.

2-4. Application to Solar Cells

As mentioned above, high-quality a-Si films can be deposited in the super chamber, which is an important factor in the improvement of characteristics of a-Si devices. With this in mind, a-Si solar cells were fabricated by the super chamber method.

The illuminated I-V characteristics and the cell structure are shown in Fig. 2-10. A textured TCO (Transparent Conductive Oxide) film was deposited on a glass substrate. Then the p-type a-SiC:H was deposited in the reaction chamber of a conventional type (not UHV) with

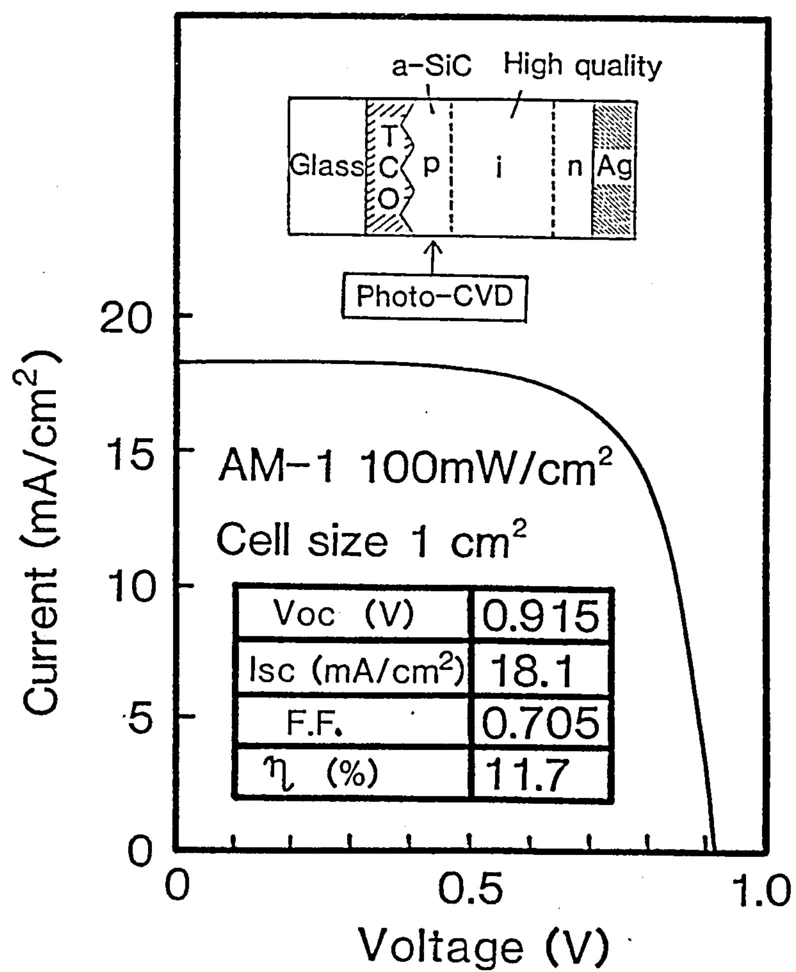

Fig. 2-10 Illuminated I-V characteristics of an a-Si solar cell fabricated in the super chamber.

the photo-CVD method with Si_2H_6 + C_2H_2 + B_2H_6 in order to prevent the contamination of oxygen from the TCO caused by ion attack during the following deposition of i-layer with a glow discharge method. The i-layer and the n-layer are a-Si:H deposited in the glow discharge method with SiH_4 and SiH_4 + PH_3, respectively. And finally, a silver back electrode was deposited. The quality of the i-layer was improved by the super chamber method, as mentioned above. The open circuit voltage (V_{oc}), short circuit current density (I_{sc}), and fill factor (F.F.) were 0.915 V, 18.1 mA/cm^2, and 0.705, respectively. A conversion efficiency of 11.7 % was obtained with a cell size of 1 cm^2, under illumination of AM-1, 100 mW/cm^2. For comparison, an a-Si solar cell with the same structure was fabricated in the conventional separated reaction chamber, and a conversion efficiency of 10.8 % was obtained, where the V_{oc}, I_{sc}, and F.F. were 0.902 V, 17.9 mA/cm^2 and 0.671, respectively. The difference of the both cell is the difference in the impurity concentration of the i-layer, which mainly affect the F.F.

Therefore, it is concluded that high performance a-Si solar cells can be fabricated with the super chamber method.

2-5. Summary

The separated UHV (ultra-high vacuum) reaction chamber system, called the super chamber, was developed for the first time. A background pressure of 10^{-9} Torr, which is two to three orders lower than that obtained with a conventional separated reaction chamber, was achieved, and a gas leakage level of 10^{-7} Torr l/sec was also achieved. The exhausted gas was investigated by GMA, and there were no signs of N_2, H_2O and so on, which did appear in the GMA spectra of the conventional chamber.

The a-Si films deposited in the super chamber were systematically studied. Impurity concentrations of oxygen, nitrogen, and carbon, measured by an ion microanalyzer, were 2×10^{18} cm^{-3}, 1×10^{17} cm^{-3}, and 2×10^{18} cm^{-3} , respectively. These values were three to ten times lower than the impurity concentrations of a-Si films deposited in the conventional separated reaction chamber. The ESR spin density and hole diffusion length of a-Si films deposited in the super chamber were 2×10^{15} cm^{-3} and 1 μ m, respectively, which were about two times superior to those of a-Si films deposited in the conventional separated reaction chamber.

A conversion efficiency of 11.7 % was obtained for a glass/textured TCO/pin/Ag a-Si solar cell, whose i-layer was deposited in the super chamber.

References

1) D.E. Carlson: J. Vac. Sci. & Technol. 20 (1982) 290.

2) S. Tsuda, N. Nakamura, M. Nishikuni, K. Watanabe, T. Takahama, Y. Hishikawa, M. Ohnishi, S. Nakano and Y. Kuwano: J. Non-Crst. Solids 77 & 78 (1985) 1465.

3) Y. Kuwano, M. Ohnishi, S. Tsuda, Y. Nakashima and N. Nakamura: Jpn. J. Appl. Phys. 21 (1982) 413.

4) C.C. Tsai, J.C. Knights, R. Lujan, B. Wacker, B.L. Stafford and M.J. Thompson: J. Non-Crst. Solids 59 & 60 (1983) 731.

5) W. E. Spear, P. G. LeComber and A. J. Snell : Phil. Mag. B38 (1978) 303.

6) G. Moddel, D.A. Anderson and W. Paul: Phys. Rev. B22 (1980) 1918.

7) J. Dresner, D.J. Szostak and B. Goldstein : Appl. Phys. Lett. 38(1981) 998.

8) N. Nakamura, S. Tsuda, T. Takahama, M. Nishikuni, K. Watanabe, M. Ohnishi and Y. Kuwano : AIP conf. Proc. No.120, Optical Effects in Amorphous Semiconductors, Snowbird, Utah, (1984) p.303.

9) C.C. Tsai, M. Stutzmann and W.B. Jackson : AIP Conf. Proc. No.120, Optical Effect in Amorphous Semiconductors, Snowbird, Utah (1984) p.242.

III. SUPER STRUCTURE A-SI FILMS AS WIDE-BANDGAP MATERIALS FOR SOLAR CELLS

3-1. Introduction

Amorphous silicon (a-Si) solar cells have been rapidly coming into practical use. The conversion efficiency of the a-Si solar cell was improved to 11.7 % with a high quality i-layer deposited with the super chamber method and a highly conductive p-layer deposited with the photo-CVD method [1]. To apply the a-Si solar cell as an electric power source, further improvement in the conversion efficiency is required.

One of the key points for improving conversion efficiencies is the effective utilization of incident light. However, there is one problem with the film properties of p-type a-SiC:H films which are used in pin a-Si solar cells. Namely, the photoconductivity of the p-type a-SiC:H film decreases as the optical bandgap increases in excess of 2.0 eV [2], and both high photoconductivity and large optical bandgap are required for the p-layer of the high-efficiency a-Si solar cell.

The a-Si super structure film was expected to show several interesting new properties [3,4]. In the previous work, the super structure films were deposited with the glow discharge (GD) method. In the GD method, deterioration of interface properties by plasma damage was suggested [5,6]. Therefore, a super structure a-Si film was deposited with the photo-CVD method for the first time in order to prevent the plasma damage to interfaces of super structure films. It was found that films of high photoconductivity can be obtained with a wide optical bandgap. Then a new type of solar cell was developed with using the super structure as the p-layer of an a-Si solar cell, also for the first time.

In this chapter, the structural, optical and electrical properties of a-Si super structure films are described, and the difference between the photo-CVD method and the glow discharge method as a preparation process for a-Si super structure films is discussed. Furthermore, the first application of a-Si super structure films to the window layers of a-Si solar cells is reported.

3-2. Preparation and Structural Analysis

3-2-1. Preparation method and reaction condition

a-Si super structure films were deposited with the photo-CVD method for the first time. For comparison, similar films were also deposited with the GD method. Typical reaction conditions are shown in Table 3-1. The structure of samples was periodically alternated with a-Si:H (well layers) and a-SiC:H (barrier layers). In the photo-CVD method, direct photolysis[6)] of source gases was used. The light sources were emission light of 184.9 nm and 253.7 nm from low-pressure mercury lamps with light intensities of 5 mW/cm^2 and 30 mW/cm^2, respectively. The reaction gas was Si_2H_6 + C_2H_2 for a-SiC layers, and Si_2H_6 for a-Si layers. In the case of the GD method, conventional reaction conditions were used, as shown in Table 3-1. In the super structure films mentioned below, both the well layers and the barrier layers were basically undoped films if not mentioned.

3-2-2. Structural analysis

In order to analyze the structure of a super structure film, a-Si:H layers of 25 Å and a-SiC:H layers of 25 Å were alternately deposited by the photo-CVD method. The depth profiles of composition atoms (Si, C) were measured by AES (Auger electron spectroscopy). The atomic

Table 3-1 Typical reaction conditions.

	Photo-CVD method		Glow discharge method	
	Barrier layer a-SiC	Well layer a-Si	Barrier layer SiC	Well layer a-Si
Gas flow rate(SCCM)	Si_2H_6 30 C_2H_2 10	Si_2H_6 30	SiH_4 10 CH_4 10	SiH_4 30
Substrate temp. (°C)	300	300	200	200
Pressure (Pa)	100	100	30	30
Depo. rate (Å/min)	25	25	20	50
Decomposition	light source 184.9 nm:5 mW/cm^2 253.7 nm:30 mW/cm^2 (low pressure mercury lamp)		RF power: 30 mW/cm^2 (13.56 MHz) capacitively coupled	

concentration of Si and C varies periodically, in accordance with our design, as shown in Fig. 3-1. The sharpness of the AES signal is determined by the limit of the depth resolution of the AES measurement system.

Figure 3-2 shows the X-ray diffraction of an a-Si super structure film in which a-Si:H film of 50 Å and a-SiC:H film of 30 Å were stacked alternately by the photo-CVD method. The Bragg reflection peak is 1.10 degrees, which corresponds to the periodical structure of 80 Å as given by eq.(3-1).

$$\sin\theta = \frac{\lambda}{2L}, \qquad (3\text{-}1)$$

where : θ is the diffraction angle, λ is the wavelength of the X-ray (1.54 Å), and L is the repeat distance of each layer. The thickness fluctuation of the interfaces between a-Si:H and a-SiC:H was estimated to be less than 7 Å from the fact that the full width at half maximum of the peak was less than 9 % of the diffraction angle of the peak.

Therefore, the periodicity of the amorphous super structure film prepared by the photo-CVD method was thought to be sufficient, which quantum effect can be expected.

3-3. Optical Properties of Super Structure Films

3-3-1. Optical bandgap

Figure 3-3 shows the optical bandgap (E_{opt}) and the B-value as a function of the well layer (a-Si:H) thickness. The E_{opt} and the B-value were determined by the Tauc plot ($h\nu - \sqrt{\alpha h\nu}$ plot), as expressed by eq.(3-2).

$$\sqrt{\alpha h\nu} = B(h\nu - E_{opt}). \qquad (3\text{-}2)$$

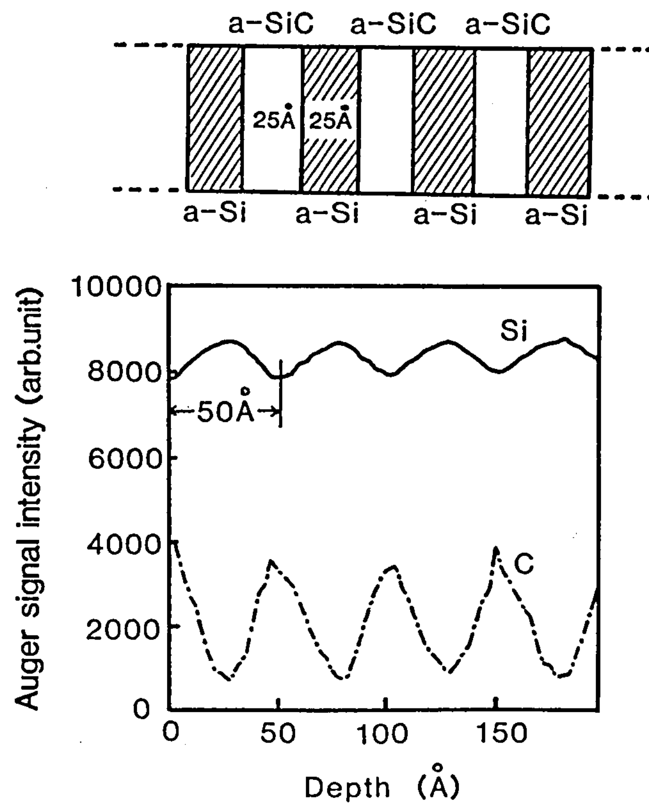

Fig. 3-1 Depth profiles of Si and C in an a-Si/a-SiC super structure film measured by AES (Auger electron spectroscopy).

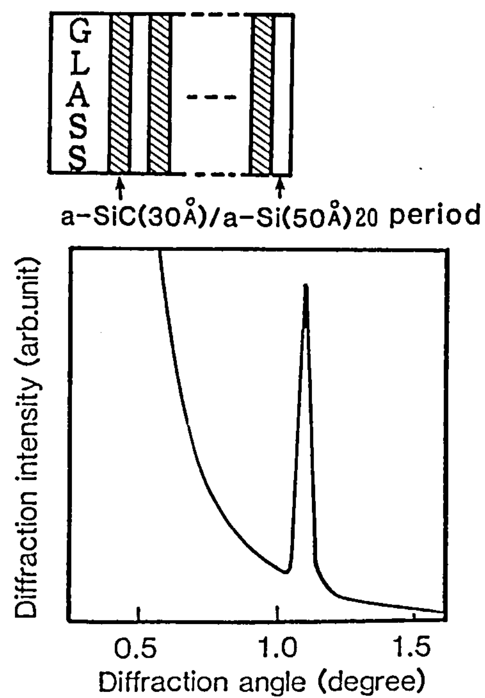

Fig. 3-2 X-ray diffraction of an a-Si/a-SiC super structure film.

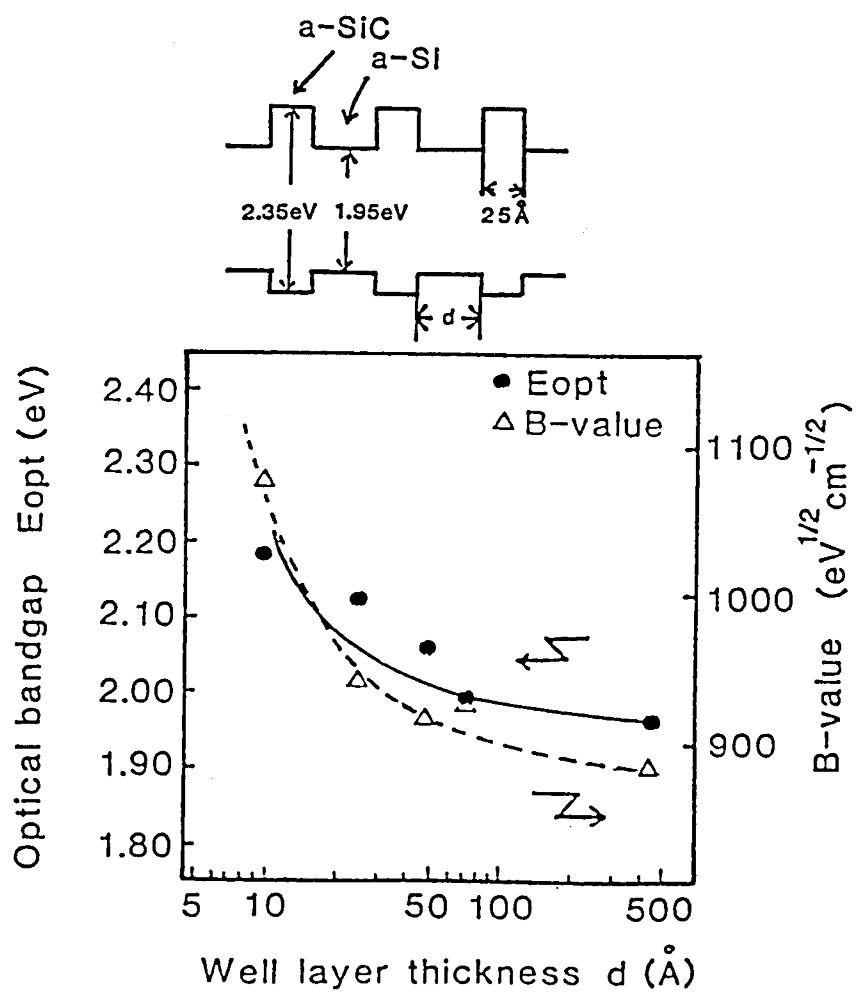

Fig. 3-3 E_{opt} and B-value of a-Si/a-SiC super structure films deposited with the photo-CVD method as a function of well layer thickness.

The barrier layer (a-SiC:H) thickness was fixed at 25 Å, and the well layer thickness was varied from 8 Å to 500 Å. Eopt of the barrier layer and the well layer were 2.35 eV and 1.95 eV, respectively. E_{opt} of the well layer is large compared with that of the conventional a-Si film prepared by the glow discharge method. The large E_{opt} is always observed for the a-Si film prepared by the direct photo-CVD method.[7] As the well layer thickness decreased below 50 Å, the E_{opt} increased from 2.0 eV to 2.2 eV and the B-value increased from 900 to 1100 ($eV^{1/2}$ $cm^{-1/2}$). The blue shift in E_{opt} of the a-Si super structure films prepared by the photo-CVD method was thought to be caused by the separation of the lowest quantum effect level in the Kronig-Penny model as given by eq.(3-3)

$$E = \frac{\hbar^2}{2 m_e^*} \left(\frac{\pi}{d} \right)^2 , \tag{3-3}$$

where, E, m_e* and d are energy level, effective mass of electron, and well layer thickness, respectively. The m_e^* was assumed to be 0.8 m_e, where m_e is electron mass. In this model, the effect of hole quantum level on the increase in the Eopt is not included for simplification, and the assumed value of the m_e* is relatively large compared with the value of a previous report (m_e* = 0.6 m_e) which included the effect of hole quantum level.[8] This model showed good agreement with the experimental values shown in Fig. 3-3, and the quantization effect was confirmed.

3-3-2. Photoluminescence

Photoluminescence (PL) spectra of the super structure films were measured with the irradiation of Ar^+ laser (5145 Å) at 77 K. The peak energy of the PL as a function of the well layer thickness is shown in Fig. 3-4. The peak energy increases with the decrease in the well layer

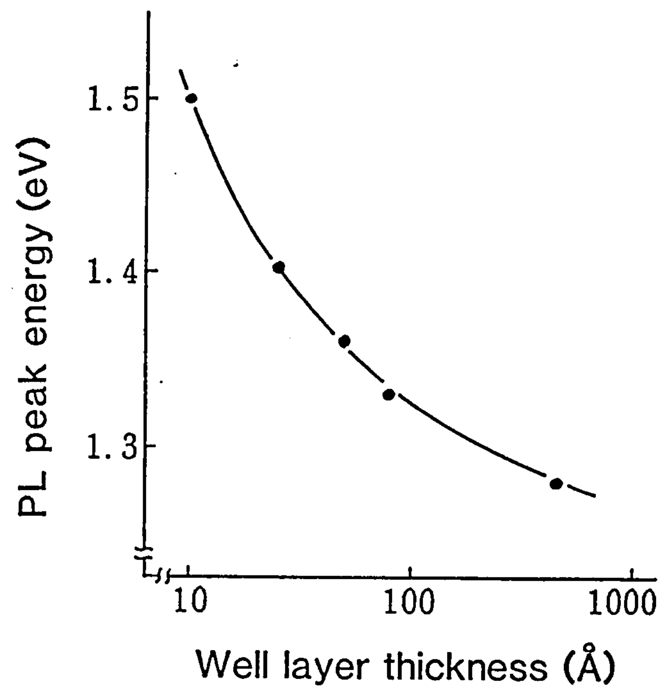

Fig. 3-4 Peak energy of the PL (Photoluminescence) of a-Si/a-SiC super structure films as a well layer thickness.

thickness, which is the blue shift of the PL. The blue shift was observed for the super structure a-Si films prepared with the GD method.[4] The origin of the blue shift is thought to come from the formation of mini-band in the conduction band by the quantization effect.

3-4. Comparison of Preparation Method

a-Si films prepared with the GD method are affected by high-energy particles in the plasma. It is possible to obtain a-Si films with less damage by using the photo-CVD method.[5] In order to investigate the effect of plasma damage on interfaces in a-Si super structure films, the absorption spectra and the PL spectra were measured for an a-SiC alloy and a super structure film, both deposited by the glow discharge method, and a super structure film deposited by the photo-CVD method. In order to clarify the difference in the PL intensity, boron was doped to the barrier layers, because it increases non-radiative recombination and the intensity of the PL from the barrier layer will become negligibly small. The gas flow rate ratio of $B_2H_6/(Si_2H_6 + C_2H_2)$ (photo-CVD) or $B_2H_6/ (SiH_4 + CH_4)$ (GD) was 1 %. In the a-SiC alloy, the gas flow rate was the average of the gas flow rates which were used for the deposition of the well layer and the barrier layer in the super structure film prepared with the GD method.

Figure 3-5 shows the Tauc plots of these samples. In the case of the super structure films, E_{opt} increases to a small extent and the B-value increases extensively.

In the PL spectra, differences among these samples are very great, as shown in Fig. 3-6. The PL intensity of the super structure film is about 100 times larger than that of the alloy. In addition, the PL intensity of the super structure film prepared with the photo-CVD method

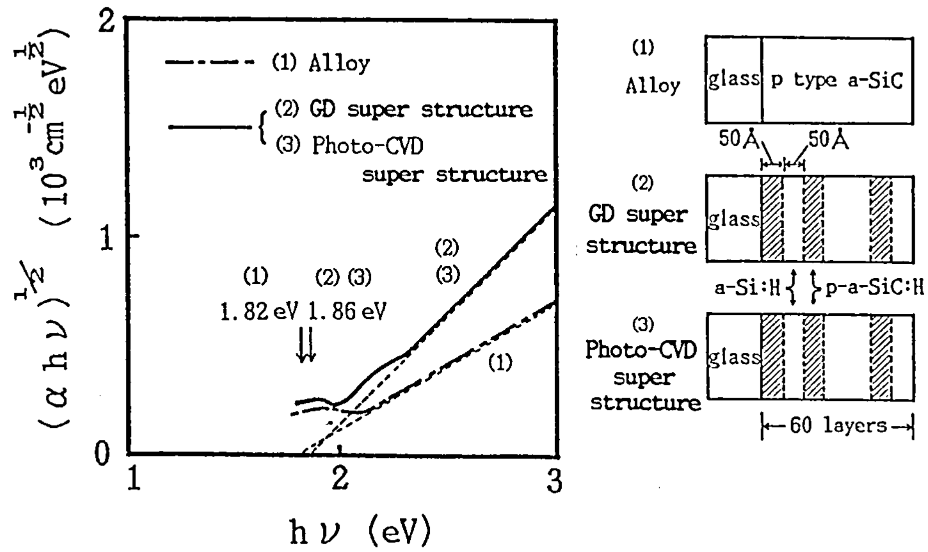

Fig. 3-5. Cross section and $\sqrt{\alpha h\nu}$ - hν plots of a-Si/a-SiC super structure films and an a-SiC alloy film.

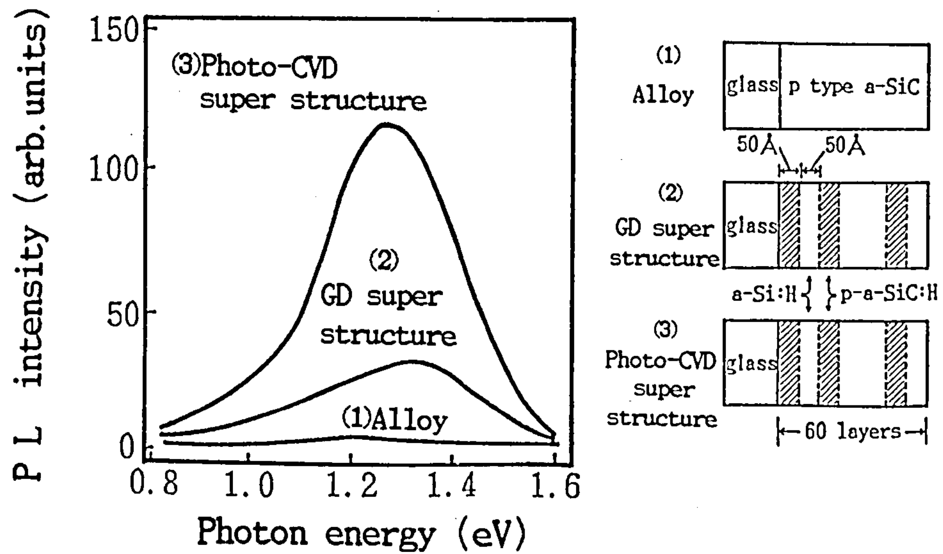

Fig. 3-6. Cross section and PL spectra of super structure films and an alloy film.

is about 4 times larger than that of film prepared by the GD method. These results may suggest that the photo-CVD method causes less damage to the interface than the GD method because of the decrease in non-radiative recombination. Good super structure film with many interfaces was thus obtained by using the photo-CVD method.

3-5. Electrical Properties Vertical to the Interfaces

The transport properties vertical to the interfaces of the super structure films were also investigated. The current-voltage characteristics vertical to the interfaces of the super structure films are shown in Fig. 3-7. The experimental values, indicated by black dots, correspond well to the calculated values from curve fitting, shown by the solid line, which are based on the tunneling transport as given by eqs.(3-4) and (3-5).

$$I \alpha V^2 \exp(-b/V) \qquad (3\text{-}4)$$

and

$$b = \frac{4\sqrt{2 m_e^*}(q \phi_B)^{3/2}}{3 q h}, \qquad (3\text{-}5)$$

where ϕ_B is the barrier height of a-SiC:H to a-Si:H, and m_e* was assumed to be 0.8 m_e, as mentioned in 3-3-1. The barrier height ϕ_B estimated from the slope of the $I/_V2$ vs. $1/_V$ plot was 0.3 eV.

The activation energies of dark conductivity for both the a-Si (well layer) and a-SiC (barrier layer), were larger than 0.7 eV, but the activation energy of the super structure films was smaller than 0.4 eV. Therefore, the carrier transport mechanism of the super structure films is not the sum of that of each layer, and it is thought to be tunneling effect because of the low activation energy compared with the activation

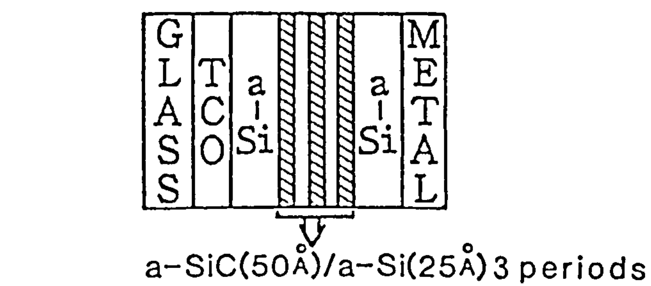

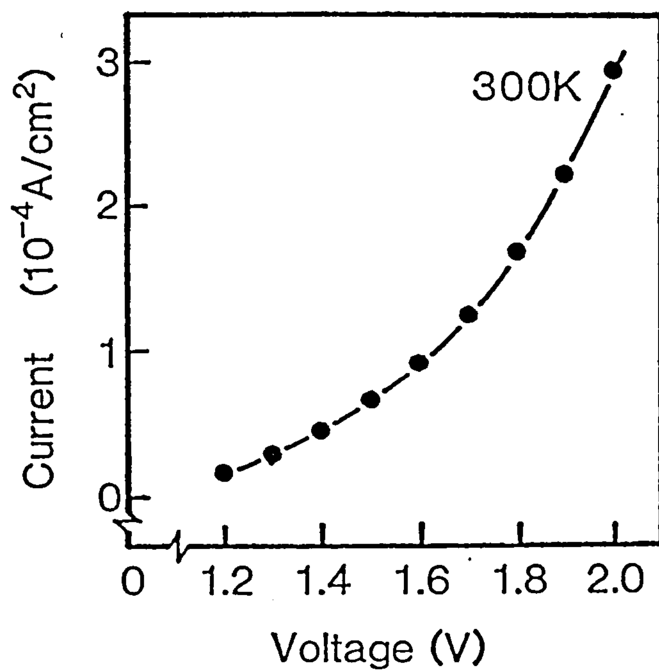

Fig. 3-7 Current-voltage characteristics vertical to interfaces of the super structure film.

energy of each layer in the super structure films.

These results indicate that the carrier transport mechanism in dark is mainly the tunneling effect in the super structure films.

The photoconductivity (σ_{ph}) and dark conductivity (σ_{d}) vertical to the interfaces of the a-Si/a-SiC super structure films were measured. The results are shown in Fig. 3-8 as a function of E_{opt}. If boron is doped to the barrier layer, narrowing of E_{opt} occures, and the difference in E_{opt} between the barrier layer and the well layer will become small. Then, for the application to the window layers of a-Si solar cells described later, 1 % boron was doped into a-Si films (well layer) in the doped super structure films. In the region of $E_{opt} > 2eV$, the photoconductivity of the super structure films was much higher than that of a-SiC films prepared by the glow discharge method, even in doped super strucutre films.

The a-Si/a-SiC superlattice structure film was found to show good properties as a wide bandgap material.

3-6. Application to Solar Cells

A new type of solar cell using the superlattice structure has been developed. In a pin a-Si solar cell, high conductivity and a wide-bandgap are required for the p-layer in order to obtain a high conversion efficiency. As mentioned earlier, the a-Si/a-SiC super structure p-layer prepared by the photo-CVD method shows excellent conductivity in the region of wide-bandgap compared with the conventional p-a-SiC alloy. For this reason, a super structure film was used as the p-layer for an a-Si solar cell for the first time. The cell structure was glass/TCO(Transparent Conductive Oxide)/super structure p-i-n/Metal, as shown in Fig. 3-9, and the cell size was 1 cm^2. The super structure

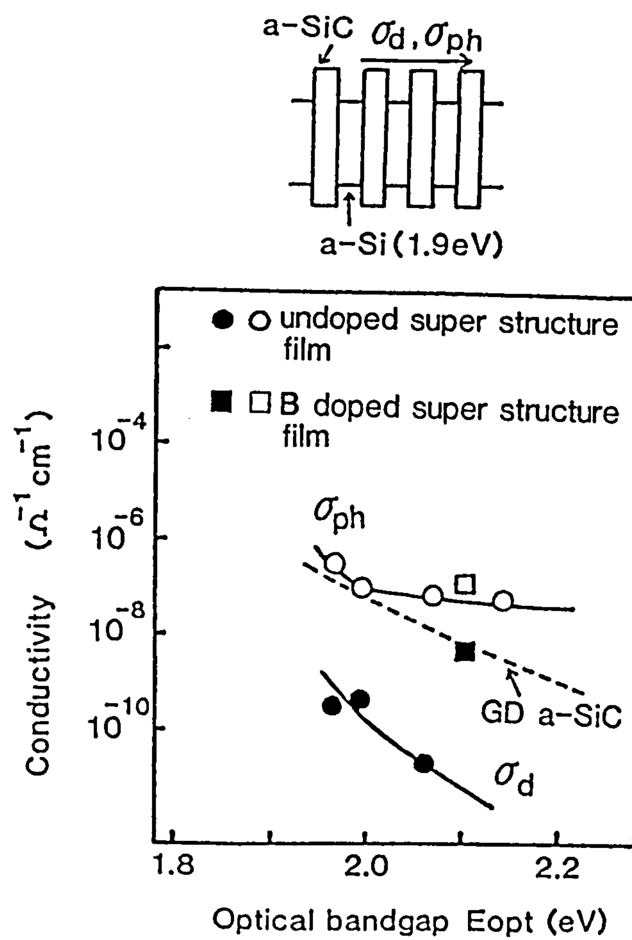

Fig. 3-8. Photoconductivity (σ_{ph}) and dark conductivity (σ_d) of the super structure film as a function of optical bandgap.

p-layer was prepared by the photo-CVD method, and it was composed of three a-Si layers (25 Å) and three a-SiC layers (25 Å) stacked alternately. The a-Si i-layer (5000 Å) and n-layer (400 Å) were prepared by the glow discharge method.

An example of the collection efficiency spectrum of the solar cell is shown in Fig. 3-10 with a typical collection efficiency spectrum of a conventional a-Si solar cell. As for boron doping, the difference in E_{opt} between the barrier layer and the well layer will become small if boron is doped to the barrier layer. In this case, therefore, 1 % boron was doped only to the a-Si layers in the super structure p-layer. The collection efficiency at short wavelengths was remarkably high, and the short circuit current density (I_{sc}) was 17.9 mA/cm^2, which is a relatively large value compared with Isc of the conventional solar cell (16 mA/cm^2). But the open circuit voltage V_{oc} (0.752 V) and the fill factor F.F. (0.623) were low, and the conversion efficiency was only 8.39 % under AM-1, 100 mW/cm^2.

In order to increase V_{oc} and F.F., boron was doped to both the a-Si layers (B_2H_6/Si_2H_6=0.1 %) and the a-SiC layers (B_2H_6/Si_2H_6=0.5 %) to increase hole density by increasing total acceptor density in the p-layer. The illuminated I-V characteristics of this type of solar cell are shown in Fig. 3-11. I_{sc} was 17.3 mA/cm^2, which is small compared with the cell mentioned in the previous paragraph because of the increase in the light absorption in the p-layer, but V_{oc} and F.F. were improved to 0.872 V and 0.694, respectively, and a conversion efficiency of 10.5 % was obtained.

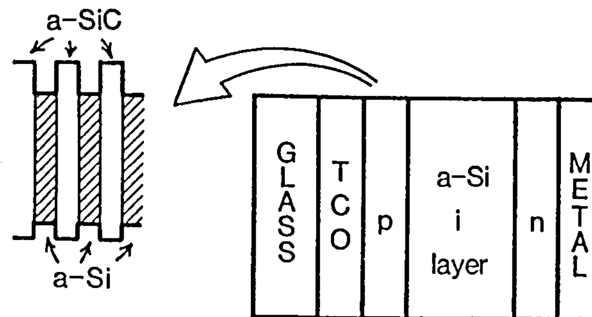

Fig. 3-9. Cross section of the super structure p-layer a-Si solar cell.

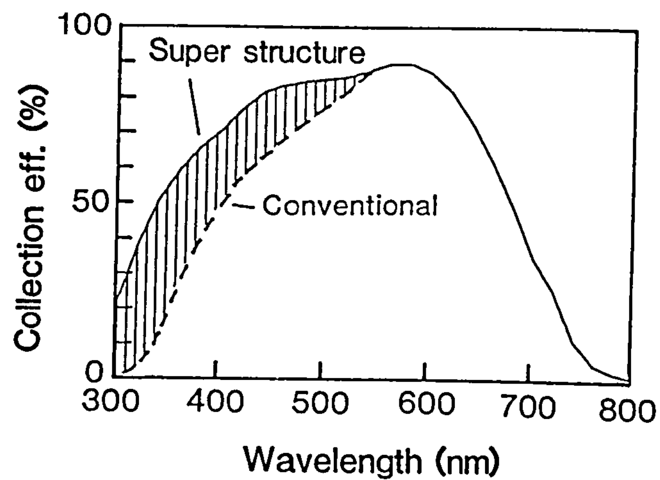

Fig. 3-10. Collection efficiency spectra of an super a-Si solar cell with a structure p-layer and a conventional a-Si solar cell.

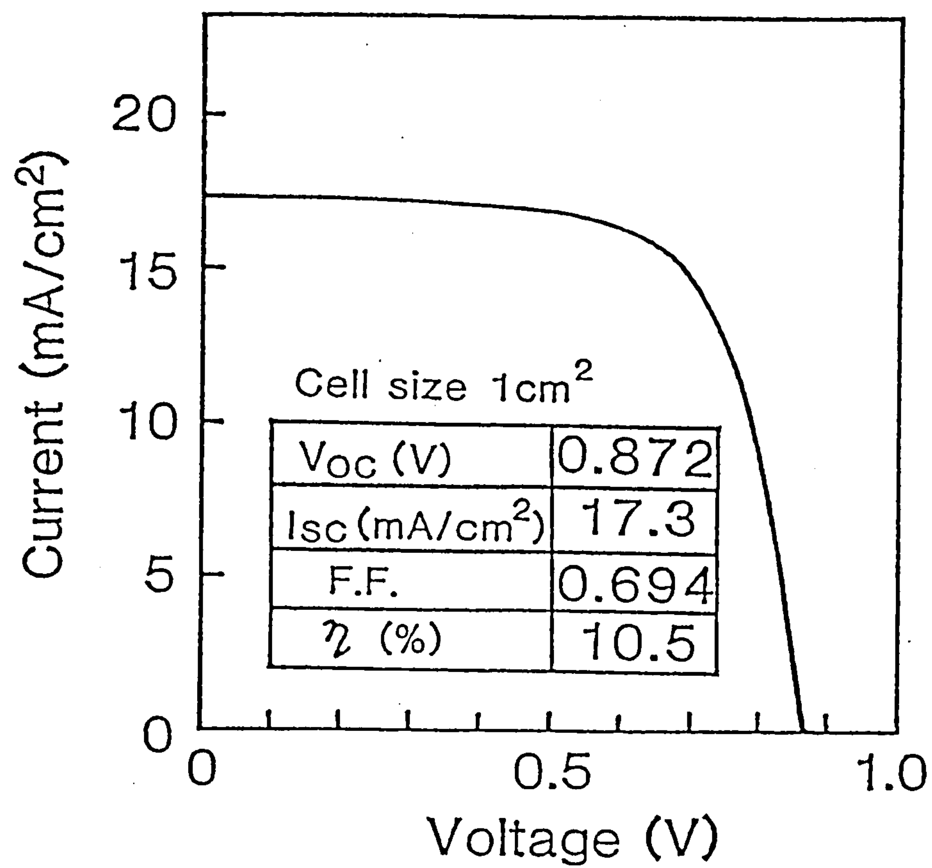

Fig. 3-11. Illuminated I-V characteristics of the super structure p-layer a-Si solar cell.

3-7. Summary

Amorphous silicon super structure films were prepared by the photo-CVD method for the first time. The periodicity of the structure of the a-Si/a-SiC super structure film was confirmed by AES and Bragg reflection of X-ray. The thickness fluctuation of the interfaces of the film was estimated to be 7 Å. The quantization effect was observed in the dependence of the optical band gap and the B-value on the thickness of well layer. It was found that the photoluminescence intensity of super structure films prepared by the photo-CVD method was about four times larger than that of similar films prepared by the glow discharge method. It shows the superiority of the photo-CVD method for the preparation of super structure films, compared with the glow discharge method. The carrier transport mechanism vertical to interfaces of the super structure film was thought to be mainly the tunneling transport in dark from I-V characteristics.

A new type of solar cell was also developed using the super structure as the p-layer of an a-Si solar cell for the first time. A remarkable increase in the collection efficiency in the short-wavelength region was observed, and a conversion efficiency of 10.5 % was obtained for a glass/TCO/p-super structure/in/metal a-Si solar cell.

References

1) S. Tsuda, T. Takahama, M. Isomura, H. Tarui, Y. Nakashima, Y. Hishikawa, N. Nakamura, T. Matsuoka, H. Nishiwaki, S. Nakano, M. Ohnishi and Y. Kuwano : Jpn. J. Appl. Phys. 26 (1987) 33.

2) Y. Tawada, M. Kondo, H. Okamoto and Y. Hamakawa : Solar Energy Material 6 (1982) 299.

3) B. Abeles and T. Tiedje : Phys. Rev. Lett. 51 (1983) 2003.

4) M. Hirose and S. Miyazaki : J. Non-Cryst. Solids 66 (1984) 327.

5) T. Saitoh, S. Muramatsu, T. Shimada and M. Migitaka : Appl. Phys. Lett. 42 (1983) 678.

6) T. Inoue, M. Konagai and K. Takahashi : Appl. Phys. Lett. 43 (1983) 774.

7) A. Yoshikawa and S. Yamaga : Jpn. J. Appl. Phys. 23 (1984) 91.

8) T. Tiedje, C. R. Wronski, P. Persans and B. Abeles : J. Non. Cryst. Solids. 77&78 (1985) 1031.

IV. A-SIGE:H:F FILMS AS NARROW-BANDGAP MATERIALS FOR SOLAR CELLS

4-1. Introduction

In the field of a-Si solar cells, the conversion efficiency has been improved to 11.7 %.[1] But, in order to use a-Si solar cells for power-generating systems, much higher conversion efficiency is desired. Therefore, multi-bandgap a-Si solar cells, which can utilize wide spectrum of sunlight, have been investigated. The most important problem in the development of a multi-bandgap a-Si solar cell is the preparation of high-quality wide-bandgap and narrow-bandgap layers. Concerning wide-bandgap material, a-Si super structure films were found to have good properties,[2] as described in detail in Chapter III. As for narrow-bandgap materials, a-SiGe:H[3] and a-SiSn:H[4] have been investigated; however, the film quality of these materials was not sufficiently high. Recently, Shimizu et al. have proposed a-SiGe:H:F, which can be prepared by a glow discharge in SiF_4 + GeF_4 + H_2, as a high-quality narrow-bandgap material,[5] and Wagner et al. reported a-SiGe:H:F prepared by a glow-discharge method.[6] However, there are few reports on a-SiGe:H:F in which the preparation condition was widely studied.

In this chapter, the preparation condition of a-SiGe:H:F was widely investigated. Here, atomic configuration is discussed. The device properties, including interface characteristics, were also mentioned for use in solar cells.

4-2. Preparation

a-SiGe:H:F films were deposited with capacitively coupled RF (radio frequency) glow discharges in SiF_4 + GeF_4 + H_2, which is the same

reported by Nozawa et al[5]. The schematic diagram of the experimental apparatus and the reaction conditions are shown in Fig. 4-1 and Table 4-1, respectively. A consecutive separated reaction chamber apparatus was used because the intermixing of impurities could be reduced.[7] The substrate temperature T_s ranged from 150 to 250°C, the RF power from 30 to 100 W, the pressure from 0.1 to 1.0 Torr, the flow rate of SiF_4 from 50 to 250 sccm, the flow rate of GeF_4 from 0.5 to 2.0 sccm, and the flow rate of H_2 ranged from 10 to 50 sccm.

Under the reaction conditions, the gas flow rate of GeF_4 was remakably small since the incorporation efficiency of Ge atoms from GeF_4 was so high. For a-SiGe:H:F prepared under the standard reaction condition, the substrate temperature was 180°C, the RF power 50 W, the pressure 0.3 Torr, and the SiF_4 flow rate 100 sccm. The atomic concentration of each element in the a-SiGe:H:F films was analyzed by Auger electron spectroscopy (Fig. 4-2). The germanium and the fluorine concentrations of this film were estimated to be about 60 % and about 0.6 %, respectively, from the spectrum in Fig. 4-2.

4-3. Film Properties

As for the film property of a-SiGe:H:F, Shimizu et al. reported carrier transport characteristics of a-SiGe:H:F prepared with restricted reaction conditions, and observed a non-dispersive hole transport[8]. There has been no report, however, on the structural properties of a-SiGe:H:F an film. Furthermore, there has been no report on film properties of a-SiGe:H:F prepared with a wide range of reaction conditions. From the viewpoint of improving film quality, both investigations on the structural properties and on the reaction condition dependence of film properties are extensively required. These are the

Table 4-1 Reaction conditions for a-SiGe:H:F.

T_s		150～250°C
RF Power		30～100 W
Pressure		0.1～1.0 Torr
	SiF_4	50～250 sccm
Flow rate	GeF_4	0.5～2.0 sccm
	H_2	10～50 sccm

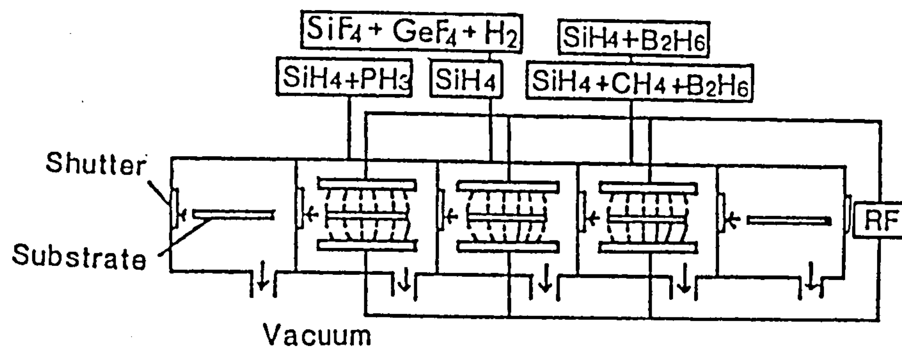

Fig. 4-1. Consecutive separated reaction chamber apparatus for the deposition of a-SiGe:H:F films and devices.

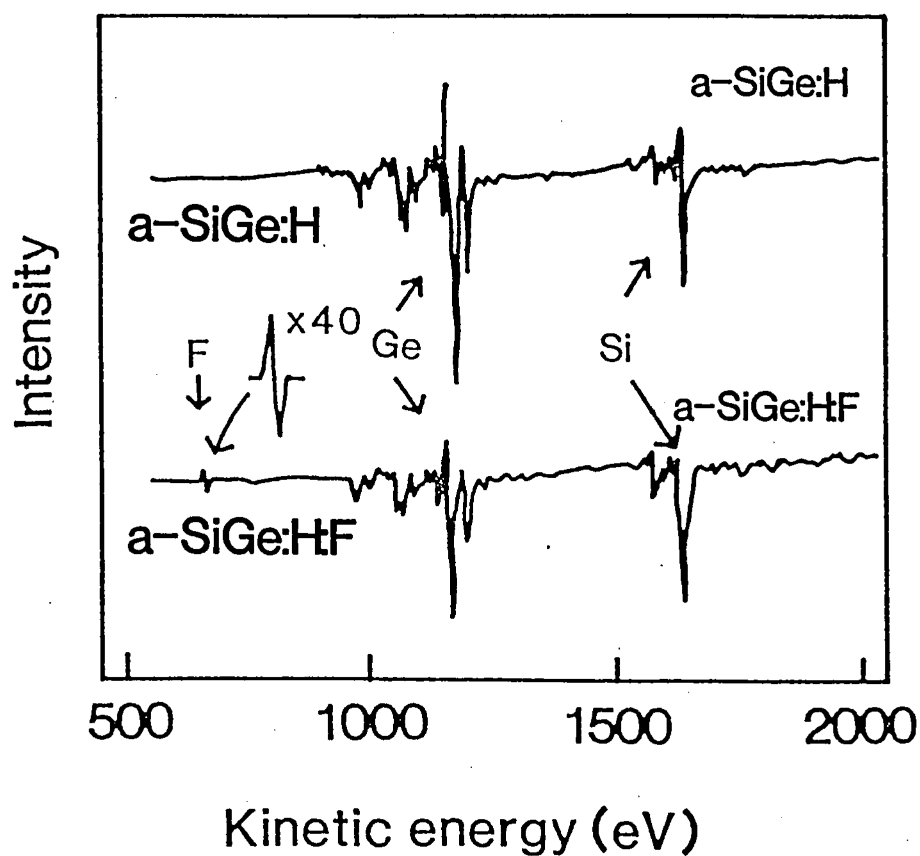

Fig. 4-2 Auger electron spectra of a-SiGe:H and a-SiGe:H:F.

purpose of this section.

In order to optimize the reaction conditions of a-SiGe:H:F, the flow rate ratio, RF power and substrate temperature were varied as parameters. Also, when one of these parameters was varied as described below, the others were kept at the values of the standard conditions mentioned in the previous section. The dark conductivity (σ_d) was measured with electrodes of co-planar type on a glass substrate; the photoconductivity (σ_{ph}) was also measured with the same configuration under illumination of AM-1, 100 mW/cm^2, and the optical bandgap (E_{opt}) and Raman spectra were measured for a-SiGe:H:F deposited on a glass substrate.

4-3-1. GeF_4 flow rate dependence

The σ_d, σ_{ph} and E_{opt} of a-SiGe:H:F are shown in Fig. 4-3 as a function of the flow rate ratio of $GeF_4/(SiF_4 + GeF_4)$.

As shown in Fig. 4-3, a boundary appears between $GeF_4/(SiF_4 + GeF_4)$ = 0.8 % and 0.6 %, that is, at about 0.7 %. In the case of $GeF_4/(SiF_4 + GeF_4)$ = 0.7 %, the σ_{ph} and the σ_d was almost the same, and E_{opt} was around 1.0 eV. The Raman spectrum of the film which corresponds to a GeF_4 flow rate ratio = 0.8 % has only one peak at 305 cm^{-1}, as shown in Fig. 4-4(a). This shows that the film is microcrystalline germanium (μ c-Ge) rather than a-SiGe:H:F. Wagner et al. reported that the SiGe:H:F films deposited with DC (Direct Current) glow discharge were amorphous in the case of GeF_4 $(SiF_4 + GeF_4)$ = 20 %, and that the difference between RF and DC deposition in the boundary of flow rate ratio for microcrystalline mainly comes from the difference in the electrode geometry.[5)]

In the case of $GeF_4/(SiF_4 + GeF_4)$ = 0.7 %, the Raman spectrum of this film indicates that it was amorphous (Fig. 4-4(b)) when the flow rate ratio was 0.6 %. For comparison, the Raman spectrum of a

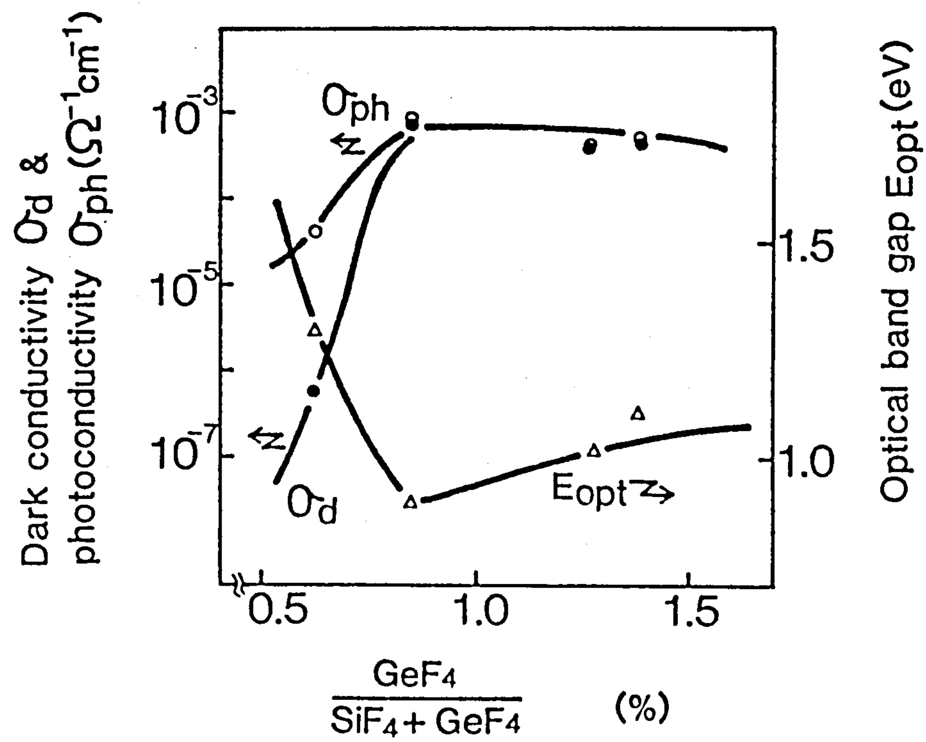

Fig. 4-3 Dark conductivity (σ_d), photoconductivity (σ_{ph}), and optical bandgap (E_{opt}) of a-SiGe:H:F as a function of flow rate ratio of $GeF_4/(SiF_4 + GeF_4)$.

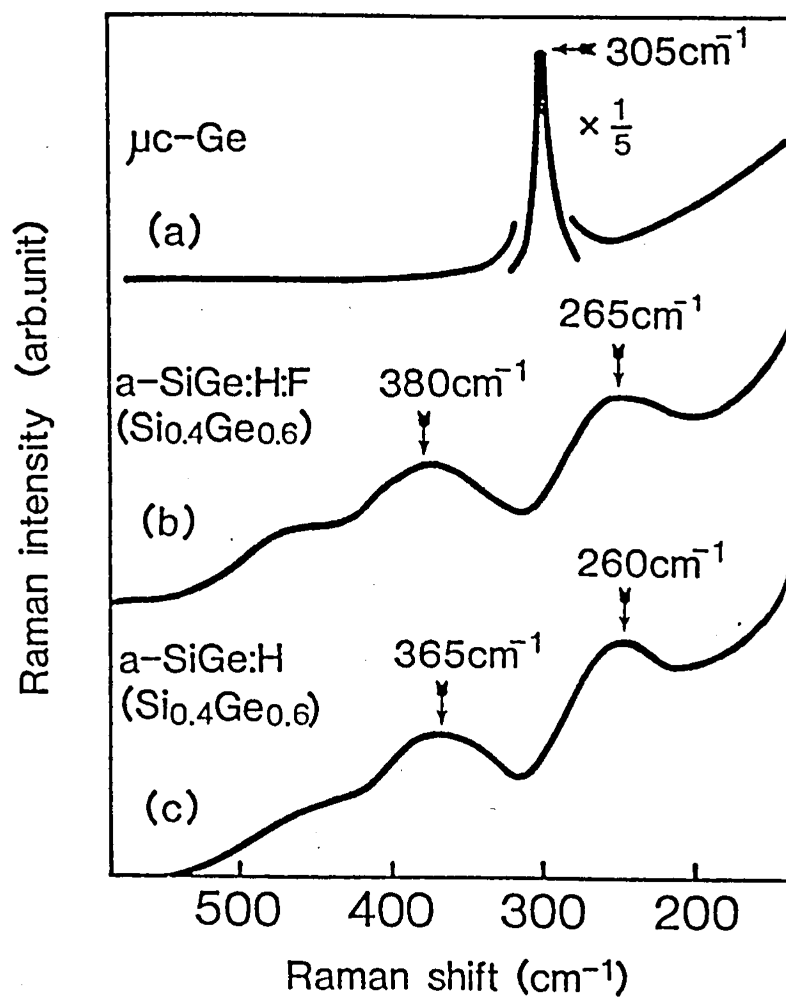

Fig. 4-4 Raman spectra of μc-Ge, a-SiGe:H:F, and a-SiGe:H.

conventional a-SiGe:H deposited with the glow discharge decomposition of $SiH_4 + GeH_4 + H_2$ is shown in Fig. 4-4(c), where the Ge concentration was 60 % and the E_{opt} was 1.4 eV. The peak positions for TO phonon of Si-Ge (380 cm^{-1}) and Ge-Ge (265 cm^{-1}) of a-SiGe:H:F were shifted to the higher values compared with those of a-SiGe:H, but the whole Raman spectrum of a-SiGe:H:F was almost similar to that of a-SiGe:H. Although the fluorine atoms may cause some changes in local atomic configuration in a-SiGe films, the whole atomic bonding structure of a-SiGe:H:F did not show a large difference from that of a-SiGe:H.

4-3-2. RF power dependence

The σ_d, σ_{ph}, and E_{opt} of a-SiGe:H:F were shown in Fig. 4-5 as a function of RF power during glow discharge deposition. E_{opt} of a-SiGe:H:F increases with the increase of RF power, which suggested that the gas decomposition ratio of SiF_4 and GeF_4 was varied with RF power. Namely, in the low RF power region, the GeF_4 gas decomposed well but the SiF_4 gas did not decompose well; an increase in germanium contents in a-SiGe:H:F caused a decrease in E_{opt}. In the high RF power region, the SiF_4 gas also decomposed well; a decrease in germanium contents in a-SiGe:H:F caused an increase in E_{opt}. These results suggest that the RF power dependence of E_{opt} comes from the difference of the decomposition energy between SiF_4 and GeF_4[9].

4-3-3. Substrate temperature dependence

The σ_d, σ_{ph}, and E_{opt} of a-SiGe:H:F films are shown in Fig. 4-6 as a function of the substrate temperature T_s. The σ_{ph} was about 1×10^{-4} Ω^{-1} cm^{-1} and was not remarkably changed with T_s. The σ_d, however, increased with an increase in T_s.

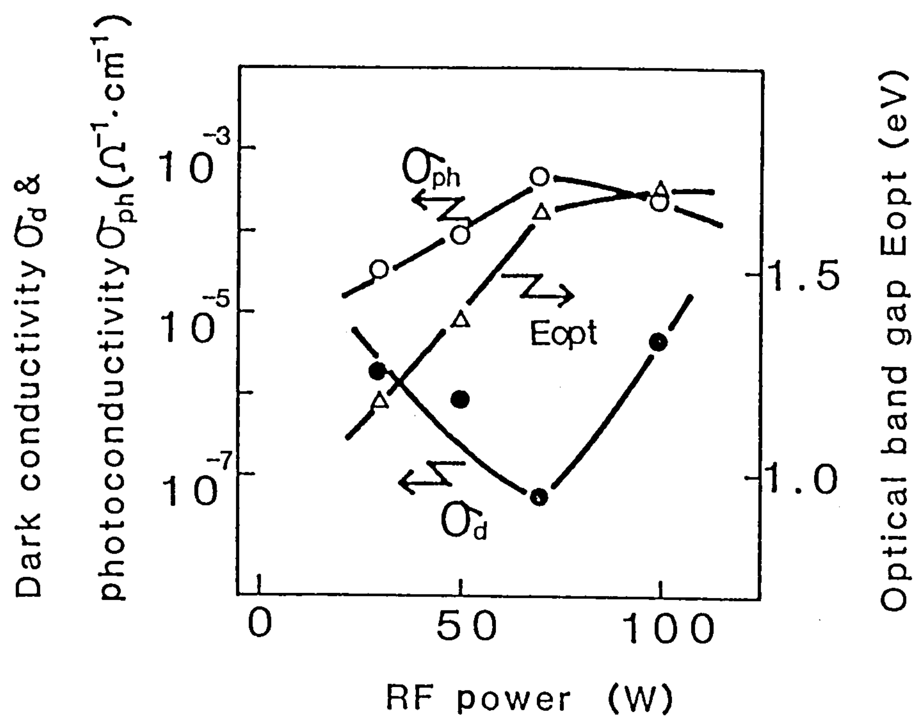

Fig. 4-5 σ_d, σ_{ph}, and E_{opt} of a-SiGe:H:F as a function of RF power.

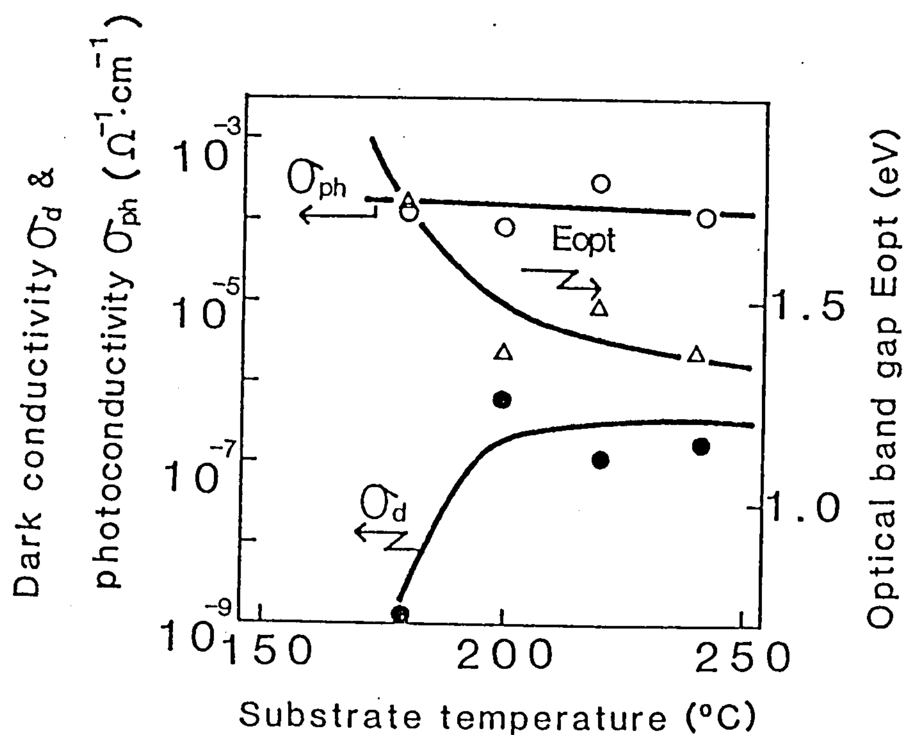

Fig. 4-6 σ_d, σ_{ph}, and E_{opt} of a-SiGe:H:F as a function of substrate temperature T_s.

The Raman spectra of three a-SiGe:H:F films deposited at different T_s are shown in Fig. 4-7. All the spectra have three broad peaks which originate from Si-Si bonds ($\sim$480 cm^{-1}), Si-Ge bonds ($\sim$400 cm^{-1}) and Ge-Ge bonds ($\sim$250 cm^{-1}) in a-SiGe:H:F. In addition to these broad peaks, the spectra of T_s = 220°C and T_s = 240°C show narrow peaks at 500 cm^{-1}, which indicate that the silicon atoms in a-SiGe:H:F films partially microcrystallize when T_s is higher than 220°C.

4-3-4. Discussion on film properties

The above mentioned dependence of a-SiGe:H:F film properties on deposition conditions were investigated as follows.

The sharp dependence of film properties on the gas flow rate ratio of $GeF_4/(SiF_4 + GeF_4)$ can be explained by a change in the atomic network. As mentioned earlier, when the flow rate ratio of $GeF_4/(SiF_4 + GeF_4)$ increased from 0.6 to 0.8 %, the sharp peak of μc-Ge was observed and the peaks of Si-Si bonds, Si-Ge bonds, and Ge-Ge bonds disappeared in the Raman spectrum. This result shows that a drastic change occurs in the atomic network when the GeF_4 flow rate increases from 0.6 to 0.8 %, (Figs. 4-3 and 4-4). Both the remarkable increase in the dark conductivity and the decrease in E_{opt} are thought to be caused by the formation of μc-Ge.

From the view point of reaction process, the reaction kinetics for the formation of μc-Ge is not clear. As for μc-Si prepared with the glow discharge in $SiH_4 + H_2$, the key factor for the formation of an μc-Si structure is the high dilution with hydrogen, and drastic change in the conductivity with the gas flow rate ratio of $H_2/(SiH_4 + H_2)$ was also reported.[10] In the case of a-SiGe:H:F, a high dilution with hydrogen is required (Table 4-1); a drastic change in the conductivity

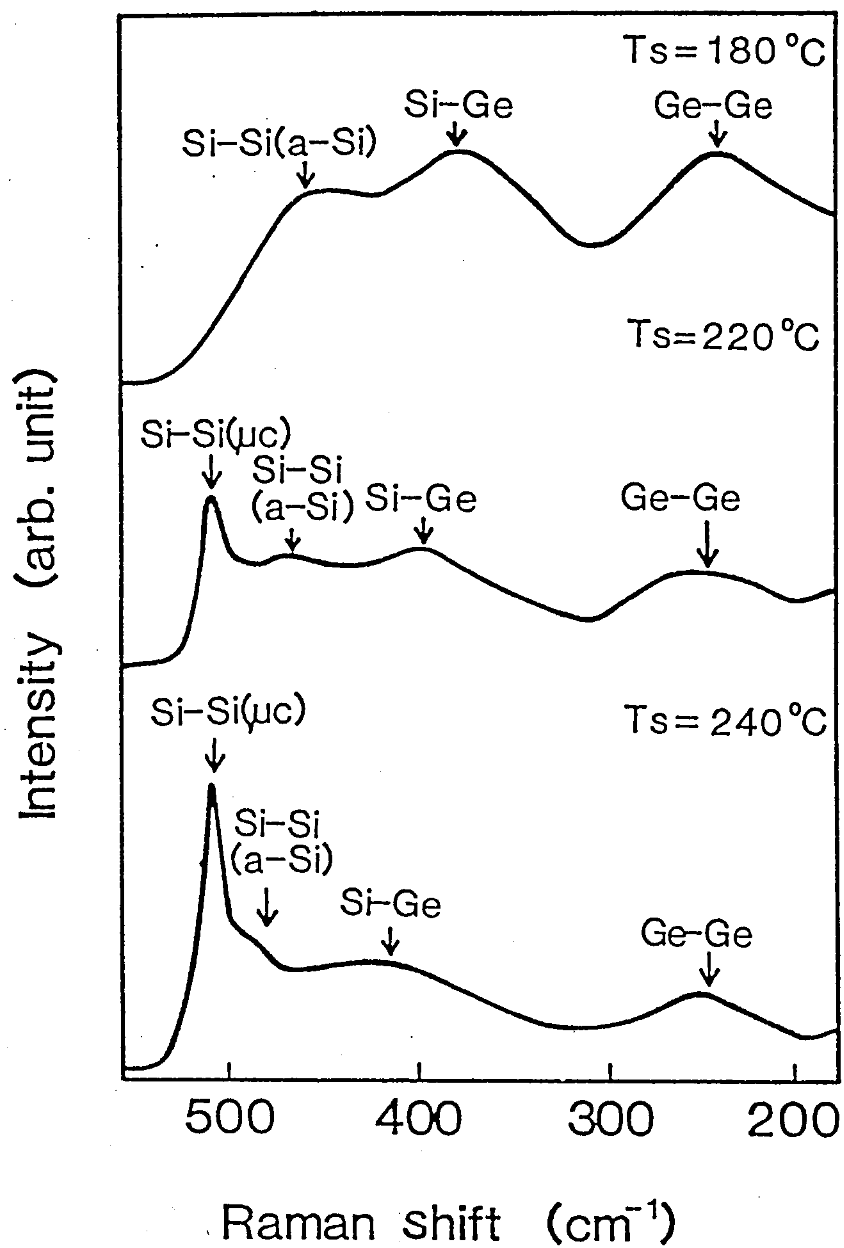

Fig. 4-7 Raman spectra of a-SiGe:H:F as a function of T_s.

was also observed as shown in Fig. 4-3. These tendencies indicate the similarity between μc-Si and μc-Ge in the reaction kinetics.

The dependence of the film properties on the substrate temperature (Fig. 4-6) also indicates a change in the atomic network. In this case, the peak of μc-Si appeared in the Raman spectra when the substrate temperature increased to more than 200 °C; however , the peaks of the Si-Si, Si-Ge and Ge-Ge bonds did not disappear. This result indicates that the amorphous Si-Ge network does exist, even if μc-Si appears. As σ_{ph} and σ_d are almost constant when the substrate temperature increases to more than 200 °C, they are thought to be determined by not μc-Si but Si-Ge network.

After optimizing the reaction condition, σ_{ph}, σ_d and E_{opt} were $10^{-4}\,\Omega^{-1}\,cm^{-1}$, $10^{-7}\,\Omega^{-1}cm^{-1}$, and 1.4 eV, respectively, for a high-quality a-SiGe:H:F film, where the substrate temperature was 180 °C. The germanium concentration of this film was 60 %.

4-4. Device Characteristics

4-4-1. I-V characteristics of Schottky diodes

In order to examine the electrical characteristic of a-SiGe devices, Schottky diodes were fabricated. a-SiGe:H:F and a-SiGe:H were deposited on n^+type crystalline silicon (c-Si) substrates, and Au (gold) electrodes were evaporated as a barrier metal. The current-voltage (I-V) characteristics of these diodes are shown in Fig. 4-8, where E_{opt} of both films was 1.4 eV.

In the case of a-SiGe:H:F, which is represented by solid lines, the rectification ratio was more than 10^7 at a bias voltage of 1 V. This value was two orders higher than the rectification ratio of the a-SiGe:H diode. The diode quality factor n and the reverse saturation current

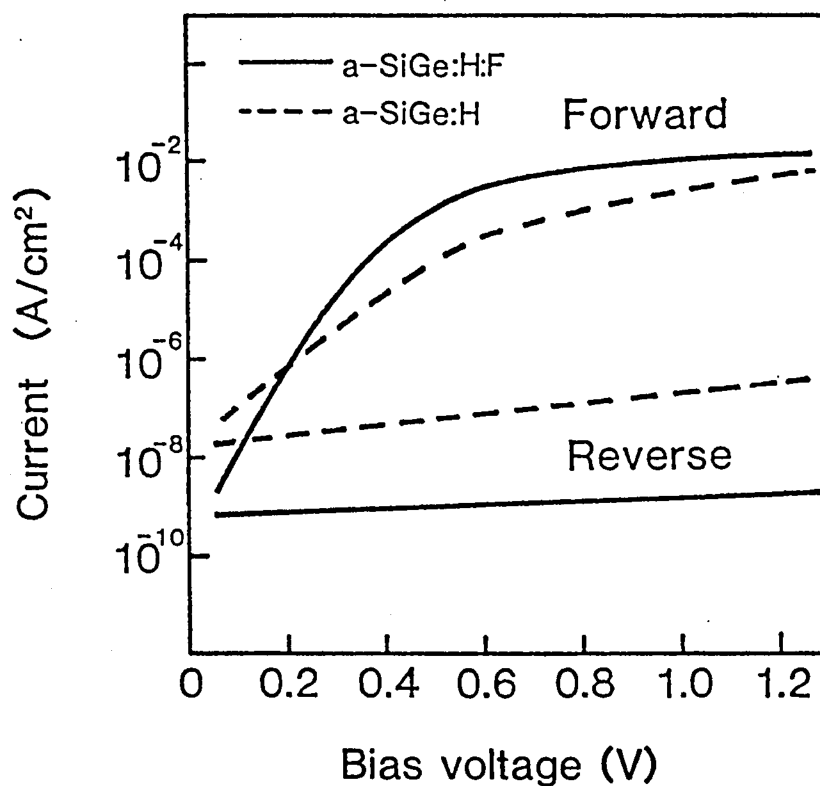

Fig. 4-8 Dark current-voltage characteristics of a-SiGe Schottky diodes.

Table 4-2 Diode characteristics of Schottky diodes.

	a-SiGe:H	a-SiGe:H:F
n	1.88	1.12
I_0 (A/cm^2)	5×10^{-9}	4×10^{-10}

density I_0 (A/cm^2) are shown in Table 4-2. These two values also indicate the small carrier recombination rate in the a-SiGe:H:F diode.

4-4-2. Collection efficiency spectra of pin diodes

In order to apply a-SiGe:H:F to solar cells, pin diodes with i-layers of a-SiGe:H:F were fabricated. A p-layer (a-Si:H) of 150 Å was deposited on a glass/SnO_2 substrate, then an i-layer of 5000 Å and an n-layer (a-Si:H) of 400 Å were deposited.

During the deposition of a-SiGe:H:F, a large number of fluorinated radicals exist in the glow-discharge plasma; they can affect the previously deposited p-layer. The conventional p-layer for a pin cell whose i-layer is a narrow bandgap material (such as a-SiGe:H) was a-Si:H, because the difference of E_{opt} between p type a-Si:H and a-SiGe:H was not very large. In the case of the p type a-Si:H, the p-layer may be deteriorated by fluorinated radicals. Therefore, a-SiC:H was proposed to use for p-layer of a pin cell whose i-layer was a-SiGe:H:F.

The collection efficiency spectra are shown in Fig. 4-9; the solid line is for p(a-SiC:H)-i(a-SiGe:H:F)-n(a-Si:H), and the broken line is for p(a-Si:H)-i(a-SiGe:H:F)-n(a-Si:H). The collection efficiency of the proposed cell structure was much higher than that of the conventional cell structure. It was also higher than that of the p(a-SiC:H)-i(a-Si:H) -n(a-Si:H) cell which is the standard cell structure of a single bandgap a-Si solar cell in the long-wavelength region. Although the conversion efficiency of the p(a-SiC:H)-i(a-SiGe:H:F)-n(a-Si:H) cell is low (~5 %), the collection efficiency at the wavelength of 800 nm was improved to 32 %, where the collection efficiency at the same wavelength was about 20 % in the case of a pin solar cell whose i-layer was a-SiGe:H.

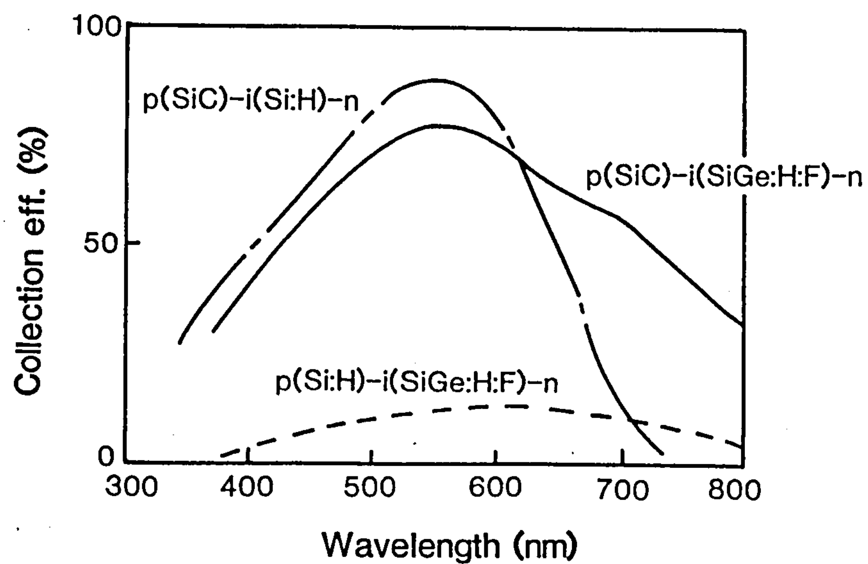

Fig. 4-9 Collection efficiency spectra of p(a-SiC)-i(a-Si)-n(a-Si), p(a-Si)-i(a-SiGe:H:F)-n(a-Si), and p(a-SiC)-i(a-SiGe:H:F)-n(a-Si) diodes.

4-5. Summary

a-SiGe:H:F films were widely investigated as a high-quality narrow-bandgap material. μc-Ge can be obtained when the gas flow rate ratio of $GeF_4/(SiF_4 + GeF_4)$ is more than 0.7 %;μc-Si can be observed in a-SiGe:H:F when substrate temperature Ts is more than 220 °C. As for the optimum reaction condition, T_s is 180 °C and the germanium concentration was 60 %. Using the optimum reaction condition, a rectification ratio greater than 10^7 was obtained for an a-SiGe:H:F Schottky diode at a bias of 1 V. A collection efficiency of 32 % was obtained at a wavelength of 800 nm with a p(a-SiC:H)-i(a-SiGe:H:F)-n(a-Si:H) diode.

References

1) S. Tsuda, T. Takahama, M. Isomura, H. Tarui, Y. Nakashima, Y. Hishikawa, N. Nakamura, T. Matsuoka, H. Nishiwaki, S. Nakano, M. Ohnishi and Y. Kuwano: Jpn. J. Appl. Phys. 26 (1987) 33.

2) S. Tsuda, H. Tarui, T. Matsuyama, T. Takahama, S. Nakayama, Y. Hishikawa, N. Nakamura, T. Fukatsu, M. Ohnishi, S. Nakano and Y. Kuwano : Jpn. J. Appl. Phys. 26 (1987) 28.

3) G. Nakamura, K. Sato, Y. Yukimoto and K. Shirahata: Proc. 3rd E. C. Photovol. Solar Energy Conf., 1980, Cannes, France, (D. Reidel Publishing Co., Boston, London, Dordrecht 1981) p.835.

4) Y. Kuwano, M. Ohnishi, H. Nishiwaki, S. Tsuda, T. Fukatsu, K. Enomoto, Y. Nakashima and H. Tarui: Proc. 16th IEEE Photovol. Specialists Conf., 1982, San Diego, (IEEE Inc., New York, 1982) p.1338.

5) K. Nozawa, Y. Yamaguchi, J. Hanna and I. Shimizu: J. Non-Cryst. Solids 59 & 60 (1983) 533.

6) D. Slobodin, J. Kolodzey, S. Ajishi, Y. Okada, V. Chu, D. S. Shen, R. Schwarz and S. Wagner: Proc. 18th IEEE Photovol. Specialists Conf., 1985, Las Vegas, (IEEE Inc., New York, 1985) p.1505.

7) Y. Kuwano, M. Ohnishi, S. Tsuda, Y. Nakashima and N. Nakamura: Jpn. J. Appl. Phys. 21 (1982) 413.

8) S. Oda, S. Ishihara, N. Shibata, S. Takagi, H. Shirai, A. Miyauchi and I. Shimizu: J. Non-Cryst. Solids 77&78 (1985) 877.

9) R. Wash: Acc. Chem. Res., 14 (1981) 246.

10) A. Matsuda: J. Non-Cryst. Solids 59&60 (1983) 767.

V. THEORETICAL ANALYSIS OF MULTI-BANDGAP A-SI SOLAR CELLS

5-1. Introduction

Hydrogenated amorphous silicon (a-Si) solar cells have been gathering much attention as low cost solar cells. One of the most important problems, however, has been their low conversion efficiency compared with crystalline silicon (c-Si) solar cells. Recently, the conversion efficiency of the a-Si solar cells has been improved to exceed 11 %[1,2] with the progress of research on new window materials, such as a-SiC. The theoretical efficiency was calculated for the pin a-Si solar cell with an optical bandgap of 1.7 eV, and estimated to be 12.5 % under AM-1 sunlight.[3] Since the energy loss is mainly due to imcomplete use of incident light, effective use of the incident light is the most important point in improving the conversion efficiency of a-Si solar cells. There have been few reports on systematic studies for the effective use of the incident light in a-Si solar cells.

In this chapter, a theoretical calculation of output characteristics of an a-Si solar cell is described. Next, the theoretical conversion efficiency of amorphous solar cells is discussed, when optical bandgap of bulk material is varied. Based on the above results, a new structure called a multi-bandgap solar cell, in which amorphous solar cells with different optical bandgaps are stacked in series, is described. Its optimization is studied to calculate the theoretical conversion efficiency of the multi-bandgap solar cell. Finally, materials needed to realize the optimized multi-bandgap solar cell are investigated.

5-2. Calculation of Theoretical Conversion Efficiency for a-Si Solar Cell

In this section, a basic procedure to obtain the theoretical output characteristics of a pin type a-Si solar cell is described.

5-2-1. Equivalent circuit

An equivalent circuit of a solar cell used here is shown in Fig. 5-1. In the figure, I_{ph}, I_d, I_{sh}, I and V are photocurrent, dark diode current, shunt current, output current, and output voltage, respectively, where R_s and R_{sh} are series and shunt resistances, respectively.

There are two kinds of photocurrents in a solar cell : diffusion current and drift current. In the case of a c-Si solar cell, the diffusion length of minority carriers is much longer than the width of the depletion layer, and so, I_{ph} is mainly produced outside of the depletion layer, and the output voltage dependence of I_{ph} is negligibly small. On the other hand, in the case of an a-Si solar cell, since the diffusion length of minority carriers is almost the same as the width of the depletion layer, I_{ph} is mainly produced in the depletion layer, and thus I_{ph} strongly depends upon the output voltage. Therefore, in the analysis of the energy conversion process of the a-Si solar cell, the output voltage dependence of I_{ph} must be considered.

The output current I(V) under illumination is

$$I(V) = I_{ph}(V) - I_d(V) - I_{sh}(V) \tag{5-1}$$

where the dark diode current is represented as follows:

$$I_d(V) = I_0 \left\{ \exp \frac{q(V + I R_s)}{n k T} - 1 \right\} \tag{5-2}$$

In eq. (5-2), I_0, q, n, k, and T are reverse saturation current, electronic charge, diode quality factor, Boltzmann's constant, and absolute temperature, respectively. I_{sh} can be written as follows:

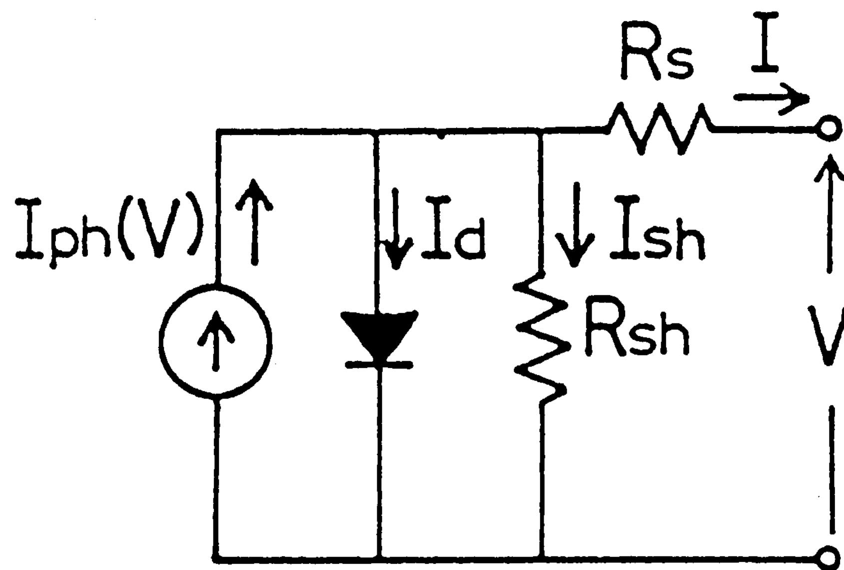

Fig. 5-1 Equivalent circuit of a pin a-Si solar cell.

$$I_{sh} = \frac{V + I R_s}{R_{sh}} \tag{5-3}$$

In the a-Si solar cell, R_{sh} is varied with light intensity, whereas R_{sh} is constant in the c-Si solar cell. Therefore, R_{sh} in this study is assumed to be the value under solar irradiation (AM-1, $100mW/cm^2$).

5-2-2. Sequence of calculation

As mentioned above, the output voltage dependence of the photocurrent $I_{ph}(V)$ is required for the calculation of the theoretical output characteristics of the a-Si solar cell. $I_{ph}(V)$ is determined by the electric field distribution in the depletion layer, so one must calculate the charge distribution, which is influenced by the gap state, to solve Poisson's equation.

Therefore, the sequence of the calculation begins with the determination of the gap state distribution in a-Si, as shown in Fig. 5-2. In the following subsections, each step of the flow chart shown in Fig. 5-2 is described.

5-2-3. Gap state distribution function

The distributions of potential energy and electric field in an a-Si solar cell are obtained by solving Poisson's equation, in which the charge density distribution, indicated by ρ , is represented by the Fermi integrals as a function of the electric potential ϕ :

$$\rho(\phi) = p^+(\phi) - n^-(\phi), \tag{5-4}$$

$$p^+(\phi) = \int_{-\infty}^{\infty} \frac{g_v(\varepsilon)\, d\varepsilon}{1 + \exp[\{(\varepsilon_f - \phi) - \varepsilon\}/kT]} \tag{5-5}$$

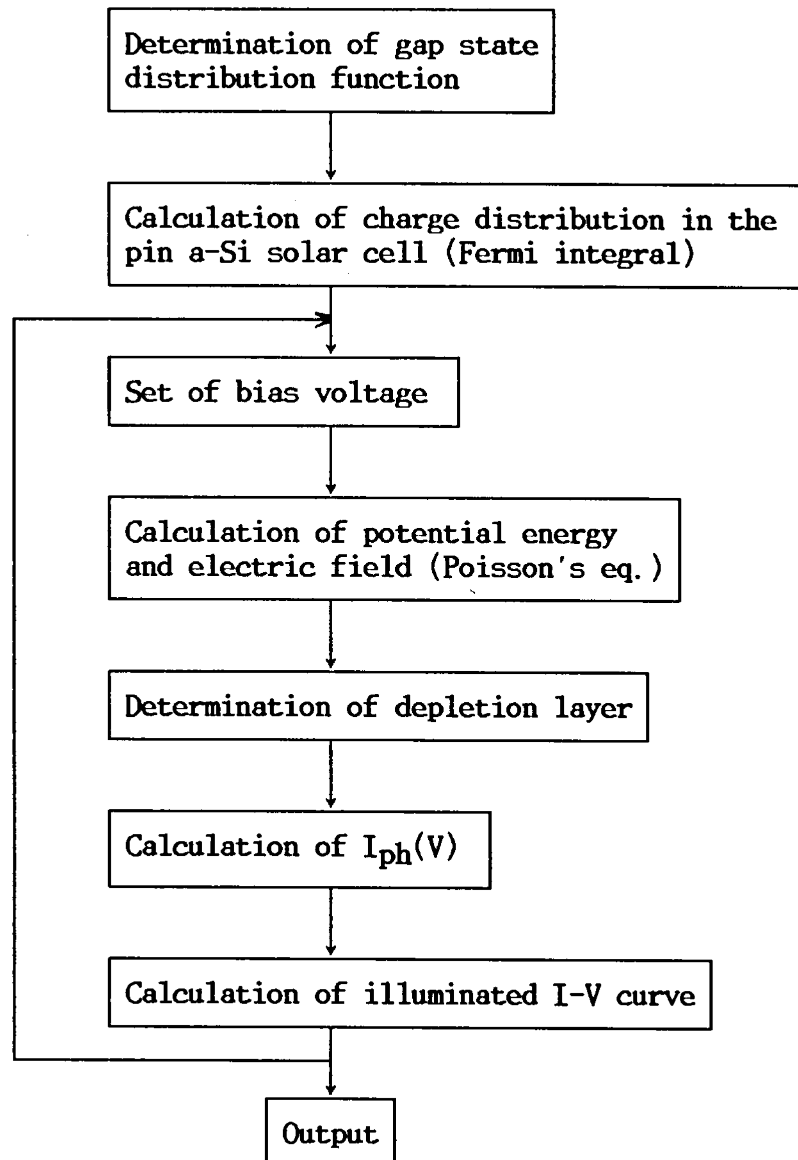

Fig. 5-2 Flow chart for the calculation of the theoretical output charcteristics of a pin a-Si solar cell.

and

$$n^{-}(\phi)=\int_{-\infty}^{\infty}\frac{g_c(\varepsilon)\,d\varepsilon}{1+\exp[\{\varepsilon-(\varepsilon_f-\phi)\}/kT]} \qquad (5\text{-}6)$$

where $p^{+}(\phi)$ and $n^{-}(\phi)$ represent the densities of the ionized donors and acceptors, respectively, and ε_F, the Fermi level. $g_v(\varepsilon)$ means distribution of donor-like states which extend from the side of the valence band ε_v into the gap. The donor-like states are thought to be neutral when they are occupied. Assuming the Fermi-Dirac distribution function at zero temperature, the donor-like states will give a positive charge above ε_f. $g_c(\varepsilon)$ means distribution of acceptor-like states which extend from the side of the conduction band ε_c into the gap, and the acceptor-like states will give a negative charge below ε_f with the same assumption. The most significant difference between properties of c-Si and a-Si is the density of gap states in the forbidden band. As for the i-layer of c-Si, the density of gap states is negligibly small in the calculation of the charge distribution. On the other hand, as for the i-layer of a-Si, the density of gap states is so large that the electric field is strongly affected by the ionized gap states.

For this reason, the determination of the gap states is important. Several examples of the distribution of the gap states are shown in Fig. 5-3. In the figure, (a) refers to the experimentally determined distribution for undoped a-Si reported by Spear et al.[4) As for a computational model for the distribution of the gap state in the calculation of theoretical efficiency of a-Si solar cells, Shur et al. used the V distribution in their model.[5) Konagai et al. assumed the 'U' distribution[6) as shown in Fig. 5-3 (b) to compensate for a faulty point in the V distribution model with regard to the fact that the density of states near the Fermi level is overestimated in comparison with the

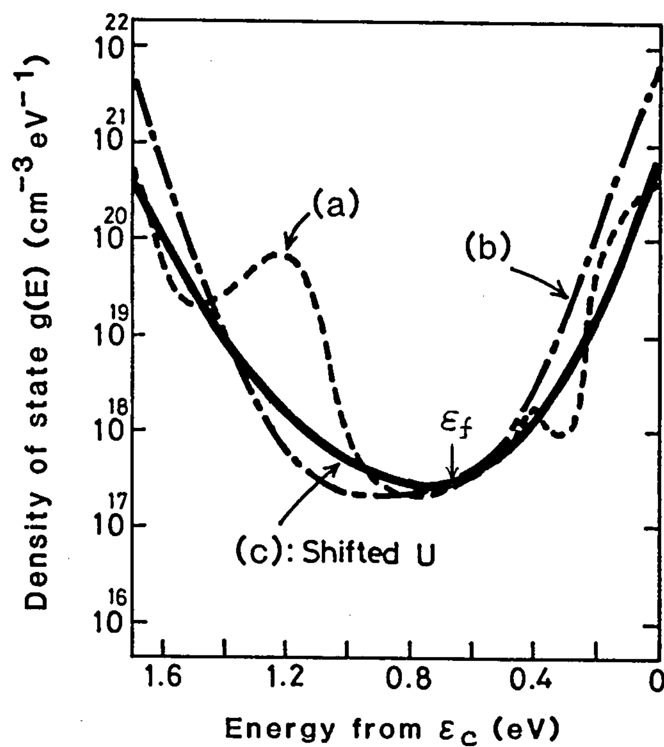

(a) Spear et al

(b) $$g(E) = g_{min1} \cosh \frac{E}{E_{01}} + g_{min2} \cosh \frac{E}{E_{02}}$$

$\left(\begin{array}{l} E_{01} = 250 \text{ meV} \\ E_{02} = 50 \text{ meV} \end{array} \right.$

(c) $$g(E) = g_1(E) + g_2(E)$$

$$g_1(E) = g_{min1} \left\{ \exp \frac{E}{E_{01}} + (\exp - \frac{E}{UE_{01}}) \right\}$$

$$g_2(E) = g_{min2} \left\{ \exp \frac{E}{E_{02}} + (\exp - \frac{E}{UE_{02}}) \right\}$$

$\left(\begin{array}{ll} E_{01} = 225 \text{ meV} & U = 1.5 \\ E_{02} = 45 \text{ meV} & \end{array} \right.$

Fig. 5-3 Gap state distribution in a-Si.

experimental result.

Both the V and U distributions are represented by a linear combination of the exponential functions, which allows us to treat the Fermi integrals analytically. The position of the Fermi level determined after integration, however, lies at the center of the forbidden band, which differs from the experimental result.

Then "Shifted U" distribution function is introduced by ourselves to solve these problems. As shown in Fig. 5-3, "Shifted" means the shift of the Fermi level from the midgap to the observed value. The shifted U distribution function is defined by the following equations:

$$g_c(E) = g_{min\,1}\, exp\left(\frac{E}{E_{01}}\right) + g_{min\,2}\, exp\left(\frac{E}{E_{02}}\right) \tag{5-7}$$

$$g_v(E) = g_{min\,1}\, exp\left(-\frac{E}{U E_{01}}\right) + g_{min\,2}\, exp\left(-\frac{E}{U E_{02}}\right) \tag{5-8}$$

In these expressions E_{01}, E_{02}, and U are parameters whose values, as shown on the right-hand side of Fig. 5-3, are determined to agree with the experiment.[7] In eq.(5-8), U is introduced to shift the Fermi level, and the same value is used in the first and second terms as the first approximation. In these equations, E=0 means the bottom of the density distribution of the gap states, which corresponds to $g_v(\varepsilon) = g_c(\varepsilon) = g_{minl} + g_{minl2}$.

The "Shifted U" model gives again an analytical expression for the charge density with band bending $\Delta\varepsilon$ (See Appendix A):

$$\rho(\phi) = g_{\min 1} kT\pi \left[\frac{\exp\left(\frac{\phi+\Delta\varepsilon}{UE_{01}}\right)}{\sin\left(\frac{kT}{UE_{01}}\pi\right)} - \frac{\exp\left(-\frac{\phi+\Delta\varepsilon}{E_{01}}\right)}{\sin\left(\frac{E_{01}}{kT}\pi\right)} \right] + g_{\min 2} kT\pi \left[\frac{\exp\left(\frac{\phi+\Delta\varepsilon}{UE_{02}}\right)}{\sin\left(\frac{kT}{UE_{02}}\pi\right)} - \frac{\exp\left(-\frac{\phi+\Delta\varepsilon}{E_{02}}\right)}{\sin\left(\frac{E_{02}}{kT}\pi\right)} \right] \tag{5-9}$$

The computed Fermi level using eq. (5-9) with the values shown in Fig. 5-3 is equal to 0.66 eV from ε_c, which agrees fairly well with the experimental value as shown by the arrow in Fig. 5-3.

5-2-4. Poisson's equation

In an a-Si solar cell, the electric potential satisfies the following Poisson's equation:

$$\frac{d^2\phi}{dx^2} = \frac{e}{\varepsilon_o \varepsilon_r}\rho(\phi) \tag{5-10}$$

where ε_0, and ε_r are the permittivity of vacuum and the relative permittivity of a-Si, respectively. e means a negative charge of electron. The electric field E(x) is also determined by the following:

$$E(x) = \frac{1}{e}\frac{d\phi}{dx} \tag{5-11}$$

In order to obtain a numerical solution of eq.(5-10), a step-by-step method has been used.[7] In this method, an initial value of electric field E(0) is assumed, and then E(0 + Δx) is calculated for small distance Δx. This calculation procedure is iterated to obtain E(x) for

the whole region. However, there is a large flexibility to set the initial value, resulting in some ambiguity (See Appendix B).

Hence, another approach based on a boundary value problem has been introduced to overcome the problem mentioned above. Integrating both sides of eq.(5-10) after multiplied by $d\phi/dx$, we obtain the following equation:

$$\frac{d\phi}{dx} = -e\sqrt{\frac{2}{\varepsilon_o \varepsilon_r}\int_0^{\phi} \rho(\zeta)\, d\zeta + C^2} \tag{5-12}$$

Then, the thickness of a-Si layer W is expressed as follows:

$$W = \frac{1}{e}\int_{\phi_n}^{\phi_p} \frac{d\phi}{\sqrt{\frac{2}{\varepsilon_o \varepsilon_r}\int_0^{\phi} \rho(\zeta)\, d\zeta + C^2}} \tag{5-13}$$

In this equation, ϕ_p and ϕ_n are the boundary potentials that are determined from the activation energies of dark conductivity for p- and n-type specimens, respectively. Regarding the integral constant C as an unknown variable, eq.(5-13) may be solved for a fixed value of W, and hence C can be determined. Then, substituting C into eq.(5-12), the equation can be solved as the first order nonlinear differential equation for the potential.

The usual method for this type of equation, the Runge-Kutta equation, may give a numerical solution of the potential ϕ as a function of x. Examples of the result of this calculation are shown in Fig. 5-4 for the cases where the bias voltage V_b=0 (short circuit) and V_b=0.8 V.

Once the potential is thus computed, the electric field E(x) can be determined by eq.(5-11). Varying the potentials ϕ_p and ϕ_n according to an applied bias voltage, this procedure is continued until whole profiles of $\phi(x)$ and E(x) become apparent.

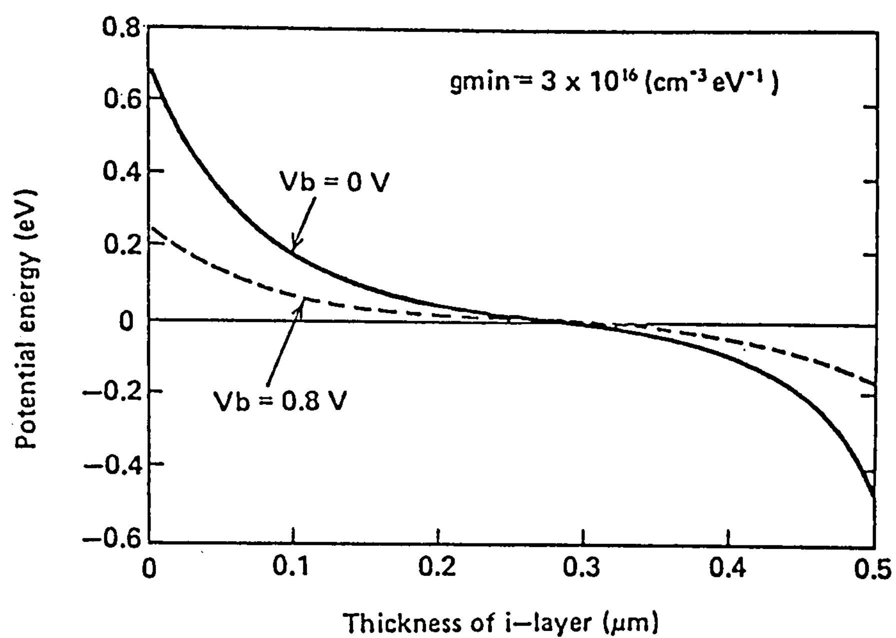

Fig. 5-4 Calculated potential energy distribution in a pin a-Si solar cell.

5-2-5. Continuity equation for minority carriers

The photocurrent generated in the a-Si solar cell is obtained by solving the continuity equation for the minority carriers with the calculated electric field, which is relatively high in the whole region of the i-layer. The electric field is determined as a function of both bias voltage and x.

As mentioned before, in the case of the c-Si solar cell, the generated photocurrent can be determined mainly by the diffusion current. On the other hand, in the case of the a-Si solar cell, the generated photocurrent can be determined mainly by the drift current, but to neglect the diffusion current causes underestimation of the photocurrent. For this reason the effect of the diffusion current should be included for the calculation of the photocurrent in the low-electric field region, as shown in Fig. 5-5. In practical calculation, a threshold level E_{th} of the electric field is introduced. In the W_s and W_b regions in Fig. 5-5, where the electric field exceeds E_{th}, the drift current is assumed to be dominant, where the transit time of the minority carrier is shorter than its lifetime. Therefore, E_{th} is determined as $E_{th} = W/\mu\tau$, where μ and τ are mobility and lifetime of the minority carriers, respectively. In the other region, W_n in Fig. 5-5, where the electric field is lower than E_0, the diffusion current is assumed to be dominant, because the lifetime of the minority carrier is shorter than its transit time.

The photocurrent $I_{ph}(V)$ is determined by the sum of $I_s(V)$, $I_n(V)$, and $I_b(V)$, which are generated in the W_s, W_n, and W_b, respectively:

$$I_{ph}(V) = I_s(V) + I_n(V) + I_b(V). \tag{5-14}$$

$I_s(V)$, $I_n(V)$, and $I_b(V)$ are obtained by solving the continuity equation for minority carriers.[6] This is solved analytically, and the

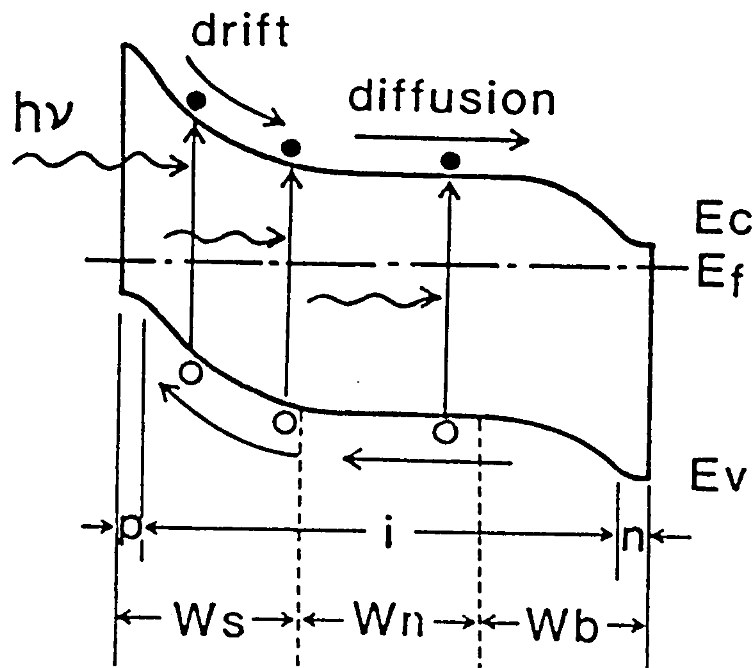

Fig. 5-5 Energy band diagram of a pin a-Si solar cell under short-circuit condition.

results are as follows (See Appendix C):

$$I_s(V) = e\int N_{in}(\lambda)[1+\exp\{-\alpha(\lambda)(W_s+2W_n+2W_b)\}] \times[1-\exp\{-\alpha(\lambda)W_s\}]\,d\lambda, \tag{5-15}$$

$$I_n(V) = -eL_p\int \frac{N_{in}(\lambda)\alpha(\lambda)}{1-L_p^2\alpha^2(\lambda)} e^{-\alpha(\lambda)W_s} \times\left[\frac{\{1+e^{-2\alpha(\lambda)W_b}\}e^{-\alpha(\lambda)W_n}-\{1+e^{-2\alpha(\lambda)(W_n+W_b)}\}\cosh(W_n/L_p)}{\sinh(W_n/L_p)} +\alpha(\lambda)L_p\{1-e^{-2(\lambda)(W_b+W_n)}\}\right]d\lambda, \tag{5-16}$$

$$I_b(V) = e\int N_{in}(\lambda)e^{-\alpha(\lambda)(W_s+W_n)}[1+e^{-\alpha(\lambda)W_b}][1-e^{-\alpha(\lambda)W_b}]\,d\lambda \tag{5-17}$$

where λ, α, N_{in}, and L_p are the wavelength of the applied illumination, absorption coefficient, incident photon density, and hole diffusion length, respectively. In eq. (5-15), $(W_s + 2W_n + 2W_b)$ comes from the assumptions of R_r (reflection coefficient of rear surface) = 1 and single reflection at rear surface.

5-2-6. Results of calculation

Thus, photocurrent is obtained as a function of applied bias voltage, and the substitution of I_{ph} into eq. (5-1), which represents the theoretical output characteristics of the a-Si solar cell, is also calculable.

Examples of the calculation are shown in Fig. 5-6. The diffusion length L_p and the minimum density of states g_{min} are assumed to be 0.15 μm and 3 x 10^{16} $cm^{-3}eV^{-1}$, respectively. The voltage dependence of the photocurrent is influenced by the i-layer thickness, because the electric

potential is determined by the i-layer thickness. In the case of an i-layer thickness of 0.3 μm, the photocurrent doesn't depend on the voltage, because the depletion layer spreads over the i-layer. In other cases, it depends on the voltage. The illuminated I-V characteristics are strongly influenced by the voltage dependence of the photocurrent, as shown in Fig. 5-6.

5-3. Calculation of Theoretical Conversion Efficiency for Single-Bandgap Amorphous Solar Cells

From the viewpoint of improving the conversion efficiency by means of the effective use of the incident light, E_{opt} should be changed. In this section, the theoretical efficiency as a function of E_{opt} is discussed.

When E_{opt} is changed, the absorption characteristics and the diode characteristics of the solar cells are changed. From the absorption characteristics, the theoretical efficiency η can be calculated with the following equation.

$$\eta = E_{opt} \times \int_{\lambda_0}^{\lambda_1} I_a(\lambda)\eta(\lambda)\,d\lambda / P_{in}, \tag{5-18}$$

where

$$I_a(\lambda) = q\,N_{in}(\lambda)\{1 - R(\lambda)\}. \tag{5-19}$$

In these equations, λ_0, λ_1, $N_{in}(\lambda)$, P_{in}, $R(\lambda)$, and $\eta(\lambda)$ are the shortest wavelength of the incident light, the absoption edge of the material, incident photon density (AM-1, 100 mW/cm^2), incident light power, reflection coefficient, and quantum efficiency. Assuming $\eta(\lambda)$

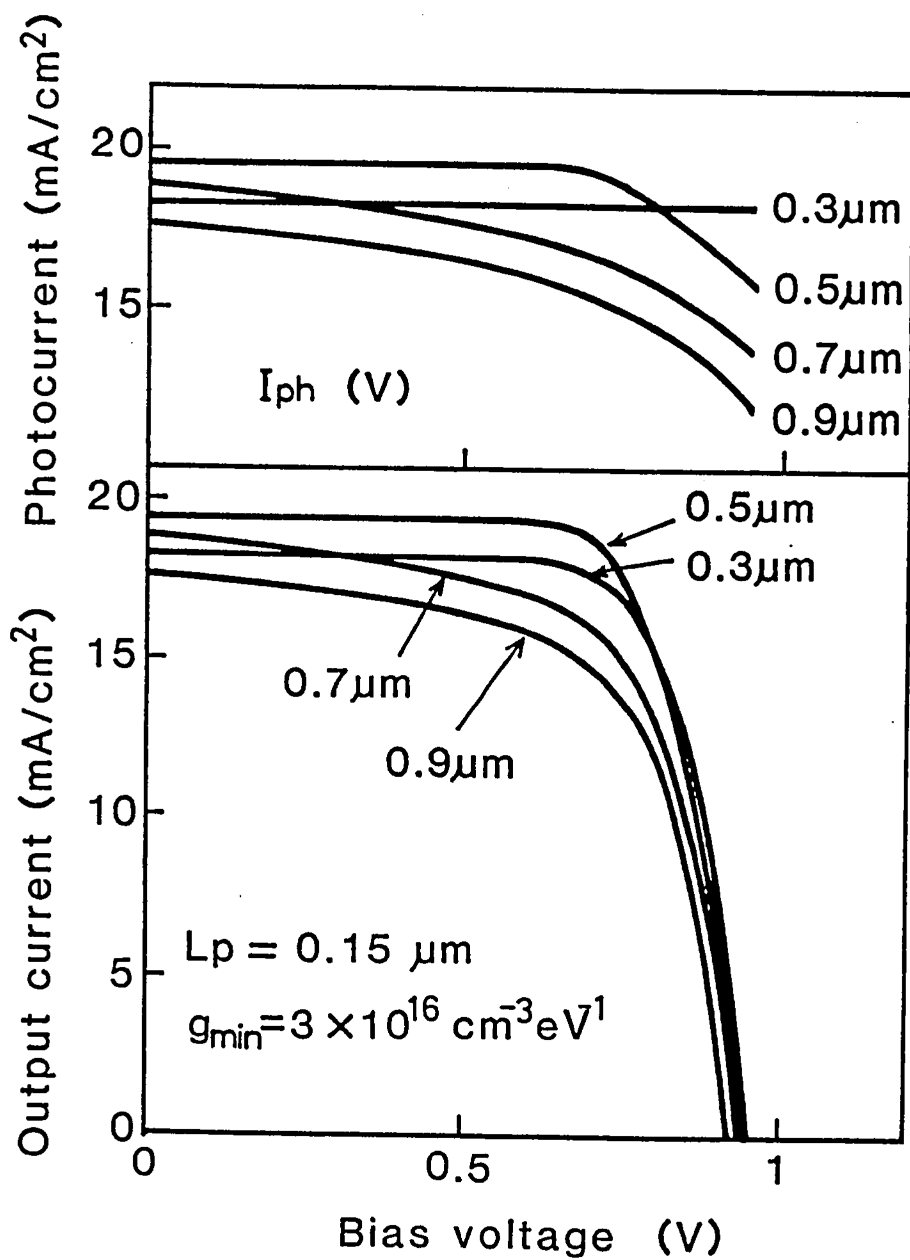

Fig. 5-6 Voltage dependence of (a) photocurrent (I_{ph}) and (b) output current (I).

=1 at $\lambda_0 < \lambda < \lambda_1$, the maximum efficiency of 46 % was obtained at E_{opt}= 1.05 eV as shown in Fig. 5-7 (a).

Then the diode characteristics are considered. The diode saturation current I_0 depends on the material properties, and it is difficult to calculate I_0 strictly as a simple function of E_{opt}. In the case of a-Si and related material, the experimential expression,

$$I_0 = 75.9 \exp\left(-\frac{E_{opt}}{2kT}\right), \tag{5-20}$$

was reported.[8] The form and values in eq. (5-20) were determined experimentally for various amorphous alloys. For simplification, this equation is used in the following discussion. Including the energy loss caused by the diode characteristics calculated, the I-V characteristics are expressed as follows:

$$I(V) = \int_{\lambda 0}^{\lambda 1} I a(\lambda) \eta(\lambda) d(\lambda) - I_0 \{\exp(qV/nkT) - 1\} \tag{5-21}$$

where n is assumed to be 1.6. From eq. (5-21) with eqs. (5-19) and (5-20), the maximum efficiency can be calculated as a function of E_{opt}, and curve (a) in Fig. 5-7 changes into curve (b) in the same figure. In this case the maximum efficiency of 27 % was obtained at E_{opt}=1.4 eV.

In the case of the calculated efficiency shown in curves (a) and (b) in Fig. 5-7, all incident photons having a larger energy than E_{opt} are assumed to be absorved. Next the practical light absorption is considered.

In the case of amorphous solar cells, the absorption characteristics can be experimentally written as follows:

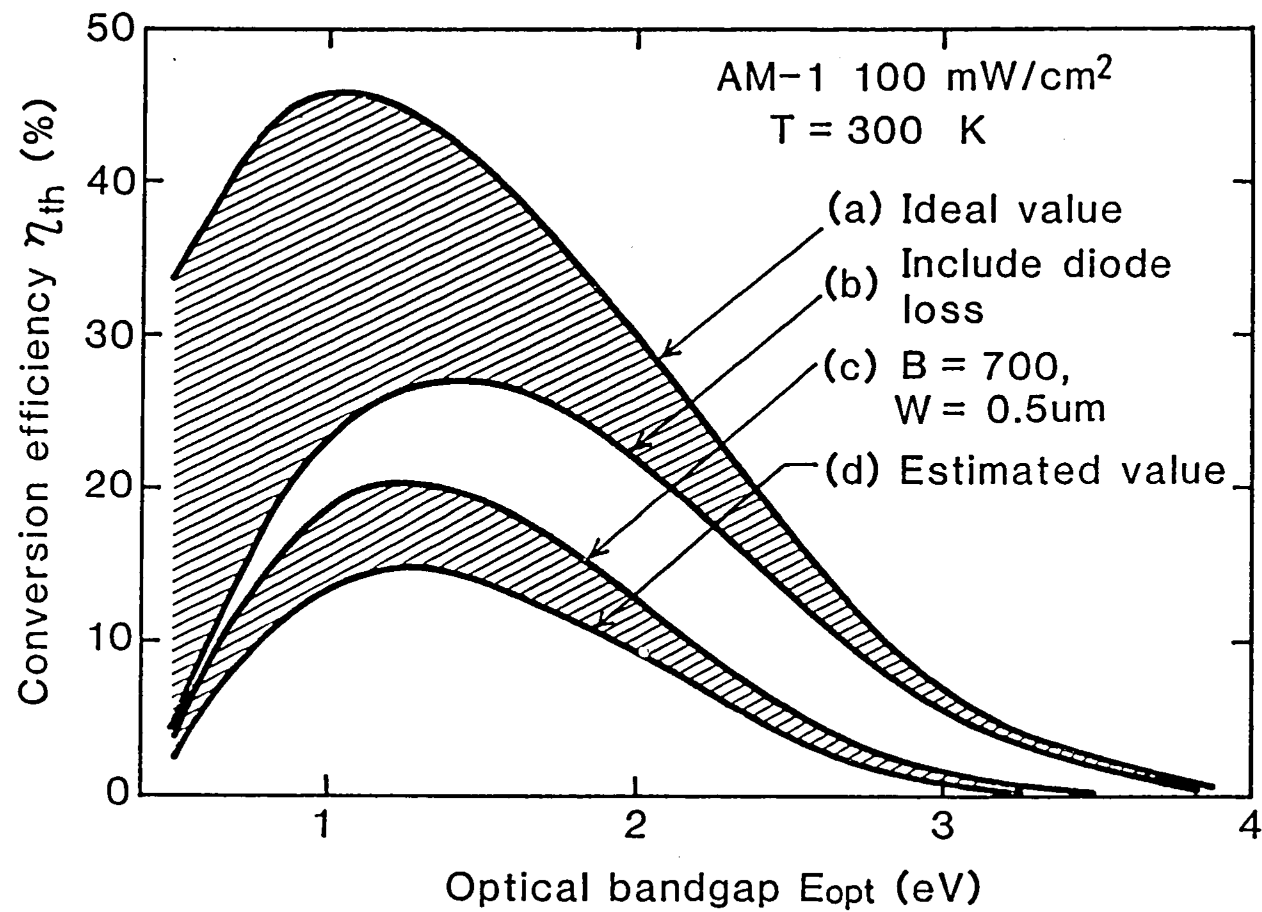

Fig. 5-7 Calculated conversion efficiency as a function of optical bandgap in the case of single bandgap solar cells.

$$\sqrt{\alpha h \nu} = B(h\nu - E_{opt}), \qquad (5\text{-}22)$$

where $h\nu$ is the incident photon energy. Although the B value has some correlation with material property, the actual value for typical a-Si alloy materials ranges from 600 to 800 ($eV^{-1/2}cm^{-1/2}$). So the B value of 700 ($eV^{-1/2}cm^{-1/2}$) was chosen for the calculation. Then the absorved light can be calculated with the thickness W of the amorphous layer and the absorbtion coefficient α determined by eq. (5-22). Then, $I_a(\lambda)$ in eq. (5-21) becomes as follows:

$$I_a(\lambda) = q N_{in}(\lambda)\{1 - R(\lambda)\}\{1 - \exp(-2\alpha W)\} \qquad (5\text{-}23)$$

where the value of 2 in the exponential term comes from the assumptions of R_r (reflection coefficient of rear surface) = 1 and single reflection. From eqs. (5-21) and (5-23), the maximum efficiency can be calculated as a function of E_{opt}. In the case of W = 0.5 μm, the calculated efficiency is shown in Fig. 5-7 (c). The maximum efficiency of 20 % was obtained at E_{opt} = 1.3 eV.

Finally, a calculated efficiency which includes effects of R_s (assumed to be 0.5 Ω/cm^2), R_{sh} (assumed to be 1000 Ω/cm^2), and $I_{ph}(V)$ is obtained from eq. (5-1) with eqs. (5-2), (5-3) and (5-4), where $I_{ph}(V)$ is

$$I_{ph}(V) = q N_{in}(\lambda)\{1 - R(\lambda)\}\{1 - \exp(-2\alpha W)\} \cdot I_{pho}(V) \qquad (5\text{-}24)$$

In eq. (5-24), the normalized voltage dependence $I_{pho}(V)$ of photocurrent is assumed to be the same as the result of 0.5 m in Fig. 5-6. The calculated efficiency is shown in Fig. 5-7(d). In this case, the maximum efficiency of 15 % was obtained at E_{opt} = 1.3 eV.

Through these calculations, the theoretical efficiency of a pin a-Si solar cell was estimated to be 12.5 % in sunlight of AM-1, 100 mW/cm^2,

where the optical bandgap (E_{opt}), W, L_p and g_{min} are 1.7 eV, 0.5 μm, 0.15 μm, and 3×10^{16} $cm^{-3}eV^{-1}$, respectively.

5-4. Calculation of Theoretical Conversion Efficiency for Multi-Bandgap Amorphous Solar Cells

5-4-1. Cell structures

The results in the previous section indicate that the theoretical limit in the efficiency of the single-bandgap amorphous solar cell is estimated to be 15 % in sunlight of AM-1. This means that the energy loss of 85 % cannot be avoided in the conventional cell structure. Most of the energy loss comes from the incomplete use of the incident light, and it is important to change the cell structure to improve the use of light. As for the crystalline solar cell, the multi-bandgap structure was proposed for the effective use of light,[9)] but the problems of lattice matching and inverse junction restrict the realization of the structure.

On the other hand, amorphous materials has a large structural flexibility and the problem of lattice matching can be easily solved. In the case of crystalline solar cells, there are inverse junctions which are, for example, np junction in pn pn pn .....type multi-bandgap solar cells. The inverse junctions may generate inverse photovoltage in the crystalline solar cells, resulting in the decrease of conversion efficiency. In the case of the a-Si solar cells, the problem of inverse junction is also overcome, because the abrupt junction formed by a heavily-doped thin p-n structure has ohmic characteristics caused by the effect of recombination caused by large density of gap states in a-Si.

With the above mentioned consideration, multi-bandgap amorphous solar cells, shown in Fig. 5-8, are discussed. In this figure, two (a)

or three (b) p-i-n amorphous solar cells which have different E_{opt} are stacked in series. More than three p-i-n cells can be also stacked.

5-4-2. Calculation method

In this section, the calculation method for optimizing each E_{opt} in the multi-bandgap structure is described.

A three-bandgap amorphous solar cell is considered as an example, where the second i-layer is assumed to have E_{opt} of 1.7 eV which corresponds to practical a-Si. The photocurrents i_{ph1}, i_{ph2} and i_{ph3}, produced in each cell of Fig. 5-8 (b), can be written as follows (See Appendix D):

$$I_{ph_1} = \int_{\lambda_0}^{\lambda_1} I_a(\lambda)\{1 - e^{-\alpha_1(\lambda)W_1}\}\eta_1(\lambda)\, d\lambda , \tag{5-25}$$

$$I_{ph_2} = \int_{\lambda_0}^{\lambda_2} I_a(\lambda)\{1 - e^{-\alpha_2(\lambda)W_2}\} e^{-\alpha_1(\lambda)W_1} \eta_2(\lambda)\, d\lambda , \tag{5-26}$$

$$I_{ph_3} = \int_{\lambda_0}^{\lambda_3} I_a(\lambda)\{1 - e^{-\alpha_3(\lambda)W_3}\} \times e^{-\alpha_1(\lambda)W_1} e^{-\alpha_2(\lambda)W_2} \eta_3(\lambda)\, d\lambda , \tag{5-27}$$

In these equations, the absorption edges λ_1, λ_2, and λ_3 are determined by each E_{opt}, and the absortion coefficients α_1, α_2, and α_3 are determined by eq. (5-22), including the effect of low absoprtion properties as follows.

$$\ln\alpha = (h\nu - E_t)/E_{ch} + \ln\alpha_{at\ h\nu = E_t} \quad (h\nu < E_t), \tag{5-28}$$

where E_{ch} (characteristic energy of tail states) and E_t (energy of

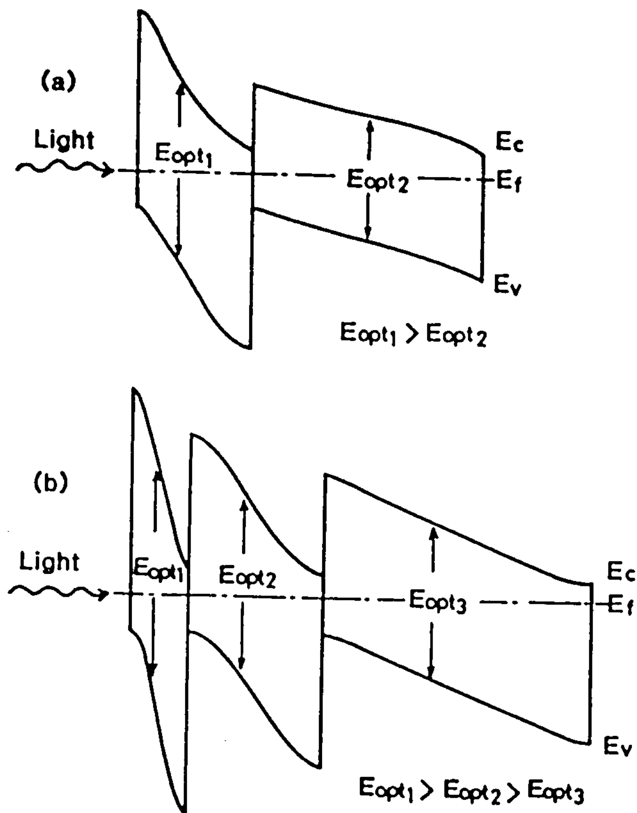

Fig. 5-8. Energy band profiles of multi-bandgap structures in the cases of two cells (a) and three cells (b).

turning point from extended states to tail states in absorption characteristics) are experimentally estimated to be 0.06(eV) and E_{opt} + 0.1(eV), respectively. The $\eta(\lambda)$, λ_0, $N_{in}(\lambda)$ and $R(\lambda)$ are the calculated quantum efficiency, the shortest wavelength of the incident light, the incident photon density (AM-1, 100 mW/cm^2), and the reflection coefficient, respectively. The internal photocurrent (I) is the same in the multi-gap structure, and it can be written as follows.

$$
\begin{aligned}
I &= i_{ph_1} - I_{01}\left\{\exp\frac{q(V_1 + I R_{s1})}{n_1 k T} - 1\right\} - \frac{V_1 + I R_{s1}}{R_{sh_1}} \\
&= i_{ph_2} - I_{02}\left\{\exp\frac{q(V_2 + I R_{s2})}{n_2 k T} - 1\right\} - \frac{V_2 + I R_{s2}}{R_{sh_2}} \\
&= i_{ph_3} - I_{03}\left\{\exp\frac{q(V_3 + I R_{s3})}{n_3 k T} - 1\right\} - \frac{V_3 + I R_{s3}}{R_{sh_3}}, \qquad (5\text{-}29)
\end{aligned}
$$

Where I_{01}, I_{02}, and I_{03} can be determined by eq. (5-20). This equation can be solved by the Newton method (See Appendix E) under the assumptions of $n_1 = n_2 = n_3 = 1.6$, $R_s = 5\ \Omega/cm^2$ and $R_{sh1} = R_{sh2} = R_{sh3} = 10^4\ \Omega/cm^2$. These values are typical values for a-Si solar cells. In the calculation the effect of the inverse junction mentioned before is estimated to be 3 % of I. The solution of these equations gives us the theoretical output characteristics of multi-bandgap amorphous solar cells.

The flow chart of the total calculation process for the multi-bandgap amorphous solar cells is shown in Fig. 5-9.

5-4-3. Optimization of each bandgap

With the above mentioned method, the theoretical efficiency was calculated as a function of E_{opt}.

In the case of the two-junction amorphous solar cell, which is

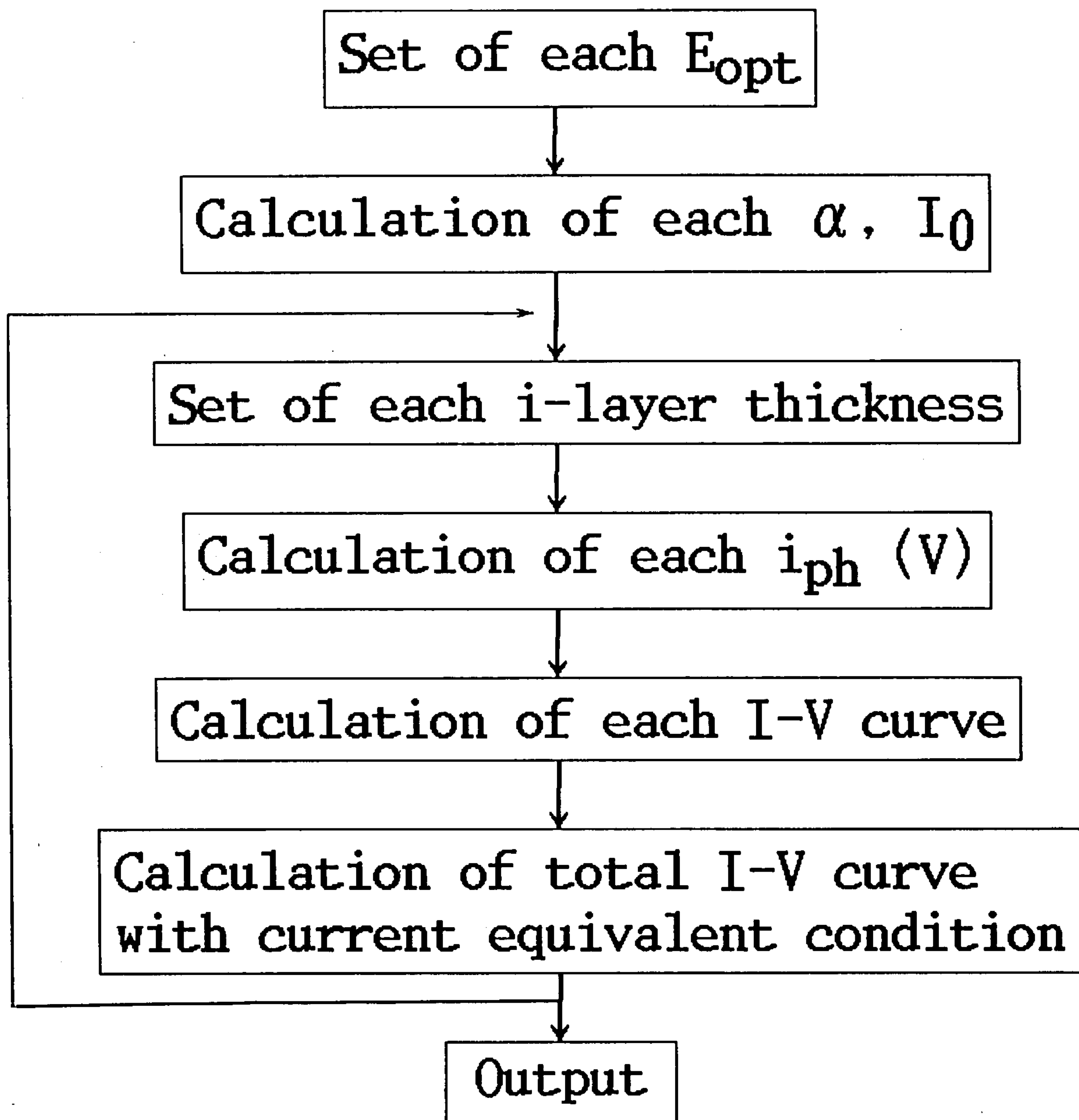

Fig. 5-9 Flow chart for the calculation of the theoretical output characteristics of a multi-bandgap amorphous solar cell.

shown in Fig. 5-8 (a), a contour map of the calculated efficiency as a function of E_{opt1} and $Eopt_2$ is shown in Fig. 5-10. The slope in Fig. 5-10 indicates $E_{opt1} = E_{opt2}$, and the calculated efficiency for the case of $E_{opt1} < E_{opt2}$ was eliminated. In this case, the maximum efficiency of 21 % is obtained for E_{opt1} = 1.75 eV and E_{opt2} = 1.15 eV.

In the case of the three-junction structure, as shown in Fig. 5-8 (b), a similar contour map is shown in Fig. 5-11. In the figure, the second cell has an E_{opt} of 1.7 eV, and the maximum efficiency of 24 % was obtained for E_{opt1} = 2.0 eV and E_{opt3} = 1.45 eV.

5-5. Realization of the Multi-Bandgap Amorphous Solar Cell

5-5-1. Material consideration

There are two ways to change E_{opt} of a-Si film. One way is to vary preparation conditions, and the other is to mix other atoms into a-Si. In the former, the most influential preparation condition is substrate temperature T_s. As shown in Fig. 5-12, E_{opt} changes by about 0.15 eV with T_s. This change in E_{opt} isn't enough to apply this method of changing T_s to the multi-bandgap structure.

In the latter, a-SiC[10] and a-SiN[11] are considered to be large E_{opt} materials, and a-SiGe and a-SiSn are considered to be small E_{opt} materials. Concerning wide-bandgap materials, we can also consider the super structure, because the thickness of the first i-layer is as thin as about 1000 Å in typical multi-bandgap cells. As the photoconductivity of the a-SiC:H/a-Si:H super structure films fabricated by a photo-CVD method is high, as mentioned in Chapter III, it is one of the hopeful candidates as the wide-bandgap material for high-efficiency multi-bandgap cells. Concerning the narrow-bandgap material, a-SiGe:H:F is thought to be also a hopeful candidate, because a high collection efficiency was

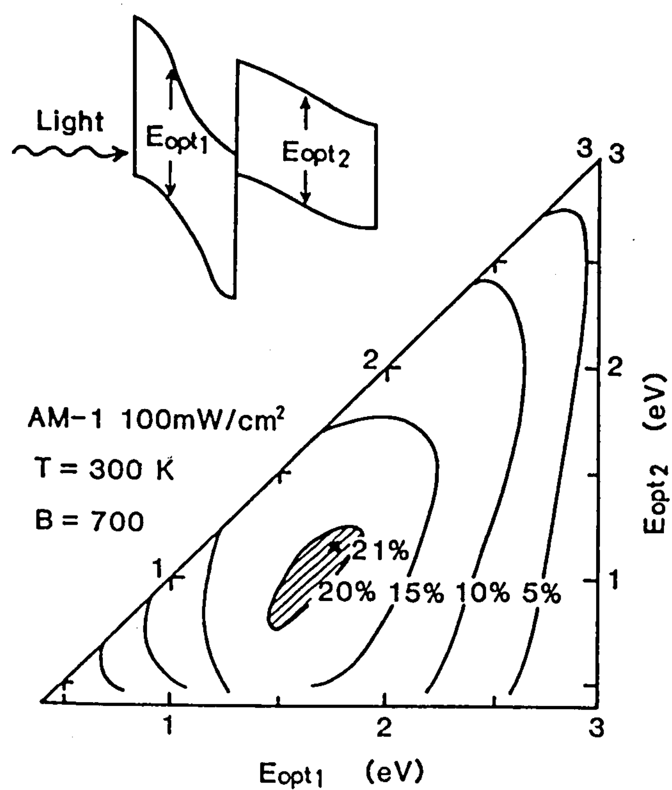

Fig. 5-10. Contour map of calculated conversion efficiency as a function of E_{opt1} and E_{opt2}.

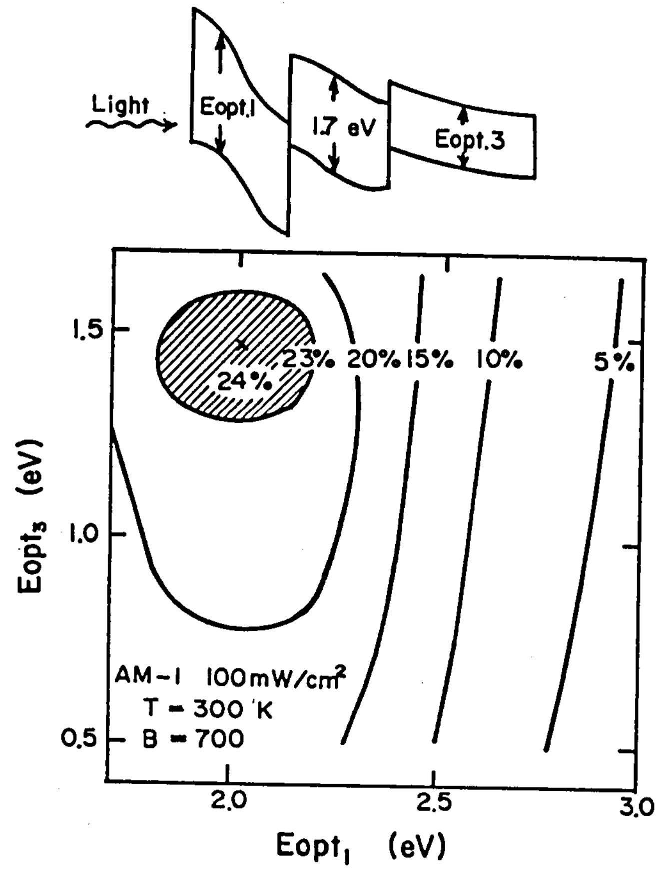

Fig. 5-11. Contour map of calculated conversion efficiency as a function of E_{opt1} and E_{opt3}; $Eopt_2$ = 1.7 eV.

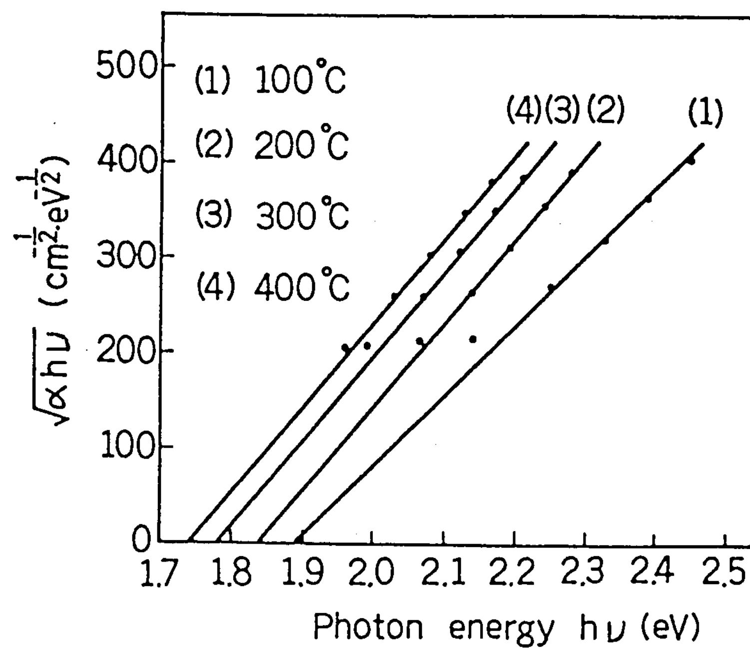

Fig. 5-12. Optical bandgap of a-Si film as a function of substrate temperature.

obtained in the long-wavelength region by this material, as shown in Fig. 4-9 of Chapter IV.

5-5-2. Discussion

The realization of the multi-bandgap structure seems to be possible from the above mentioned results. The structure of the multi-bandgap solar cell is shown in Fig. 5-13. It is optimized by the results calculated in section 5-4. The maximum conversion efficiency of this structure is estimated to be about 24 %. This conversion efficiency is the maximum value obtainable when the properties of the wide-bandgap film and the narrow-bandgap film become the same as those of a-Si film.

The problem of lattice mismatching exists in the case of the multi-bandgap cell of crystalline silicon. This problem, on the other hand, can be avoided in the a-Si cell. So, from the above results, the realization of solar cells whose conversion efficiencies are higher than those of crystalline solar cells is considered possible with amorphous solar cells.

5-6. Summary

Both theoretical and experimental considerations were made concerning an amorphous solar cell, called the "multi-bandgap structure".

The theoretical efficiencies of single bandgap, two-junction, and three-junction amorphous solar cells were calculated, and each E_{opt} of the multi-bandgap amorphous solar cells were optimized. In the three-junction cells, the second i-layer is assumed to have E_{opt} of 1.7 eV which correspons to practical a-Si, and it was shown that a theoretical efficiency of 24 % can be obtained with a multi-bandgap cell which has E_{opt} of 2.0 eV, 1.7 eV and 1.45 eV. The materials were also

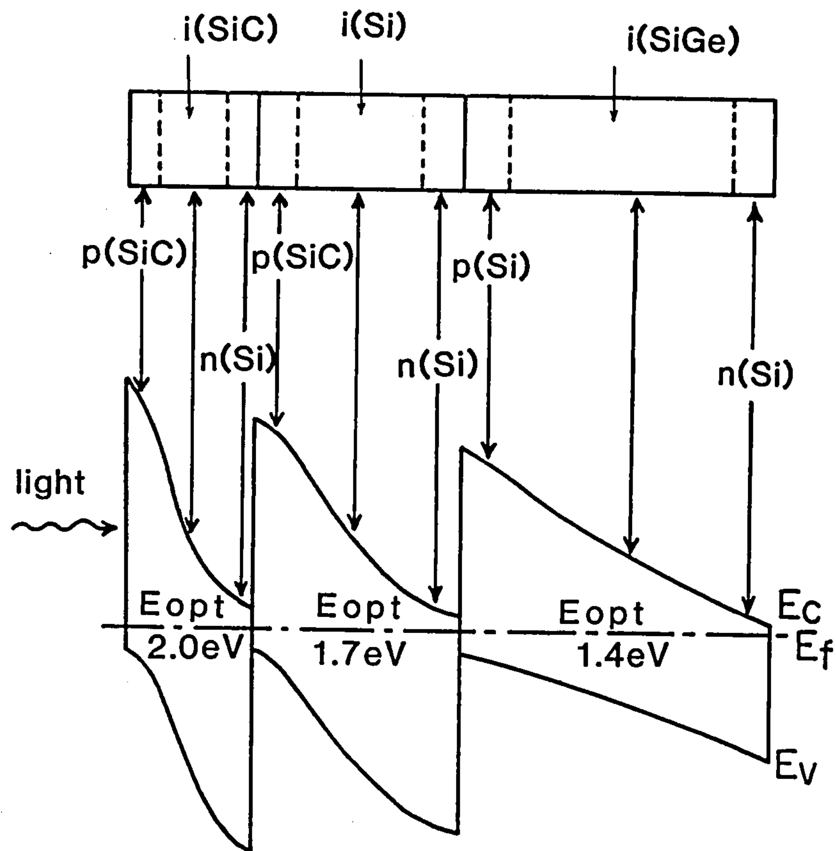

Fig. 5-13. Multi-bandgap cell structure stacked with three cells: an a-SiC cell, an a-Si cell, and an a-SiGe cell. Thickness of each layer is 0.1 μm, 0.3 μm, and 1.0 μm, respectively.

considered for this structure, and the possibility of multi-bandgap amorphous solar cells was shown.

These investigations showed that amorphous solar cells have possibilities of not only their low cost but also for high conversion efficiency compared with the conventional single crystalline solar cell.

References

1) S. Tsuda, T. Takahama, M. Isomura, H. Tarui, Y. Nakashima, Y. Hishikawa, M. Nakamura, T. Matsuoka, H. Nishiwaki, S. Nakano, M. Ohnishi and Y. Kuwano : Jpn. J. Appl. Phys. 26 (1987) 33.

2) Y. Uchida and H. Sakai : Material Research Society Symposia Proc. 70 (Material Research Society, Pittsburgh, 1986) 577.

3) Y. Kuwano, S. Tsuda, and M. Ohnishi : Jpn. J. Appl. Phys. 21 (1982) p.235.

4) W. E. Spear and P. G. LeComber : Philos. Mag. 33 (1976) p.935.

5) M. Shur, W. Czubatyj, and A. Madan : J. Non-Cryst. Solids 35 & 36 (1980) p.731.

6) H. Miyamoto, M. Konagai, and K. Takahashi : Jpn. J. Appl. Phys. 20 (1981) p.1691.

7) W.E. Spear, P. G. LeComber, and A. J. Snell : Philos. Mag. B-38 (1978) 303.

8) Y. Marfaing : Proc. 2nd E. C. Photovolataic Solar Energy Conf., Berlin (1979) p.287.

9) E. D. Jackson : Trans. of the Conference on the Use of Solar Energy, Tucson, Arizona (1955) p.22.

10) Y. Tawada, H. Okamoto, and Y. Hamakawa : Appl. Phys. Lett. 37 (1981).

11) H. Kurata, M. Hirose, and Y. Osaka : Jpn. J. Appl. Phys. 21 (1982) Suppl. 21-2, p.205.

12) G. Nakamura, K. Sato, Y. Yukimoto, and K. Shirahata : Tech. Digest 2nd Photovoltaic Science and Eng. (1980) III p-7.

VI. STUDY ON LIGHT-INDUCED EFFECTS OF A-SI SOLAR CELLS

6-1. Introduction

Recently, a-Si began to receive considerable attention as a new material for use in solar cells, and the best practical conversion efficiency of a-Si solar cells has been improved to be 11.7%.[1] Although the application of a-Si solar cells to consumer electronics has been started,[2] there are several unknown factors in the fundamental properties of a-Si films, and the problem of reliability of film properties still exists. Especially, light-induced degradation in electrical conductivity of a-Si films[3] becomes a large obstruction for practical application of a-Si solar cells to power use.[4]

In this chapter, first, the stability of a-Si solar panels is presented. Then changes in the characteristics of a-Si films and a-Si solar cells caused by light exposure are discussed, Finally, some effective methods to reduce the degradation are mentioned.

6-2. Reliability of a-Si Solar Panels

First, some results on the reliability of a-Si solar panels are described, including fabrication method, module structure, and environmental tests.

6-2-1. Preparation

In general, the conventional glow discharge process for the fabrication of a-Si films and a-Si solar cells uses a single reaction chamber method. In this method the residual dopant gases which remain on the electrodes and walls of the reaction chamber after each deposition cause an intermixing of impurities. This intermixing of impurities

of opposite types results in a deterioration of the film quality and the film reproducibility. In addition, it causes complication in discussion of the light induced effect of a-Si solar cells.

To obtain high quality and reproducibility in a-Si solar cells, a consecutive separated reaction chamber method was developed.[5] In this method, p- and n-type layers are deposited in different reaction chambers. In the following experiments, a-Si films and solar cells were fabricated by the consecutive separated reaction chamber method.

6-2-2. a-Si solar cell modules and panels

A new type of a-Si cell module, an integrated type module, has been developed.[6] In this module, a-Si solar cell units are arranged in a cascade fashion on an insulated substrate. The cell structure for this integrated type module with a size of 10 cm X 10 cm is glass/TCO/p(SiC)-i-n/metal. To take account of the power loss resulting from the resistivity of the transparent conductive oxide (TCO) electrode, each cell is connected at its side boundary, as shown in Fig. 6-1. The module consists of nine cells connected in series in accordance with an optimizing theory.[6]

The glass substrate can be used as the surface protector, and the metal of the back electrode can be used as the back protector. Therefore, the module structure is advantageous with respect to passivation.

6-2-3. Environmental tests

The solar panel has dimensions of 45 cm X 60 cm and consists of 20 integrated type a-Si modules with a size of 10 cm X 10 cm. The modules

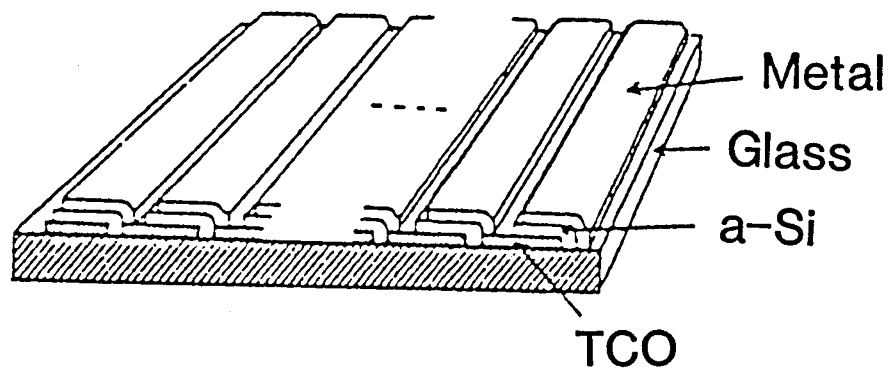

Fig. 6-1. Schematic diagram of the integrated type a-Si solar cell module.

are connected in a parallel line on the a-Si solar panel. This solar panel is composed of glass substrates and epoxy resin. The glass substrates are used as the surface protector and the epoxy resin in used as the back protector, so that the module has high reliability for weather. Figure 6-2 illustrates the results of high temperature and moisture tests on the a-Si solar panel. The conditions of these tests were as follows:(a) in the high temperature test the module was exposed for 2000 hours at 95 °C;(b) in the moisture test the module was exposed for 2000 hours at 60 °C and 95 % relative humidity.

In these tests, the changes in the conversion efficiency of the a-Si solar cell modules were negligible. It is concluded that the a-Si solar cell module has adequate temperature and moisture stability.

Figure 6-3 illustrates the results of an exposure test. In this test, the change in output performance and the visual change in a-Si solar panels were checked. The conversion efficiency of the a-Si solar panels decreased by about 10 % within one month and then became stable. The degradation is thought to be mainly caused by the light induced effect, which is descussed in the following sections.

6-2-4. Light-induced degradation in a-Si power generating system

Based on the above mentioned enviromental tests, a 2 kW photovoltaic power generating system using a-Si solar cells was constructed in April, 1981. Figure 6-4 shows a view of the system. In this electric power generating system, the total number of panels is 513. Nine panels are connected in series as one unit, and 57 series are connected in parallel lines. Of all the solar panels, 171 were installed on the main roof of the experimental model house, 189 on the awnings, and 153 on an adjoining machine room roof. These panels can generate a peak amount of 2 kW.

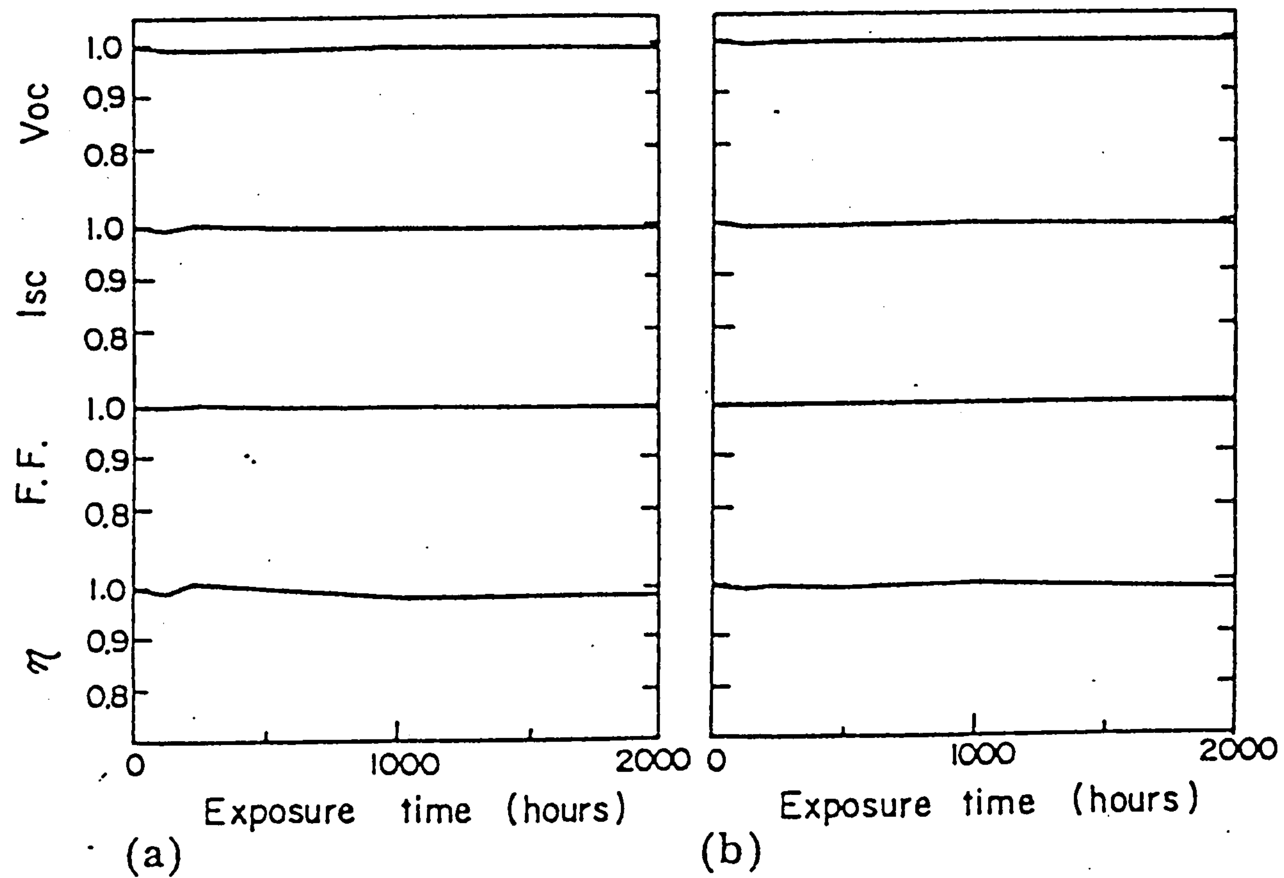

Fig. 6-2. Results of (a) a high temperature test (90 °C) and (b) a moisture test (60 °C, 95 % relative humidity).

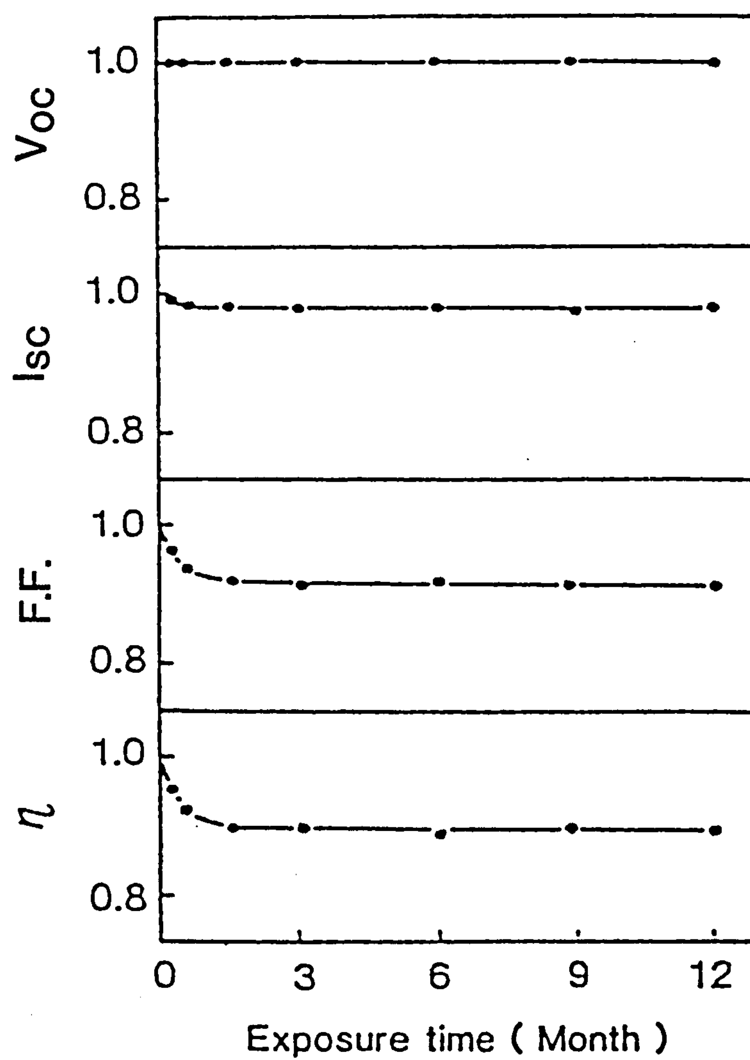

Fig. 6-3. Output characteristics of a-Si solar panels as functions of outdoor exposure time.

Fig. 6-4. Photograph of a 2 kW a-Si power generating system.

Some panels in the power generating system were checked periodically by the indoor measurement for the strict analysis of the light-induced degradation as shown in Fig. 6-5. About a 10 % degradation in the output performance was observed in the initial period of one month, which corresponds to τ_1 of the equation in Fig. 6-5, and then the degradation ratio became small. After one month, the conversion efficiency decreased in proportion to the equation of exp $(-t/\tau_2)$ as the first approximation. The value of the time constant τ_2 was about 410 months in this case.

The fact that this system has functioned stably for a long period proves that the a-Si solar panel has high reliability except for the light-induced degradation. Then the light-induced degradation must be minimized, which is the target of the following study.

6-3. Analysis of the Light-Induced Degradation in a-Si Solar Cells

In this section the light-induced effect in pin a-Si solar cells is discussed. The illuminated current density-voltage (I-V) characteristics of the pin cell before and after light exposure are shown in Fig. 6-6. The pin cell was exposed to sunlight at air mass (AM) 1 (100 mW/cm^2) for 25 hours in an open-circuit condition, which is standard exposure condition in following experiments. The thickness of the i layer of the cell was about 3000 Å and the conversion efficiency was about 5 %. As shown in Fig. 6-6, the open-circuit voltage V_{oc} and short-circuit current density I_{sc} did not change. The conversion efficiency η decreased by about 10 % owing to a decrease in the fill factor F.F. The decrease in η can be recovered by thermal annealing of 150 °C, 2 hours. Staebler et al.[4] have reported that the decrease in η was caused by the decrease in I_{sc} due to light exposure. However, our experiment suggested different results from those of Staebler et al. In order to confirm this

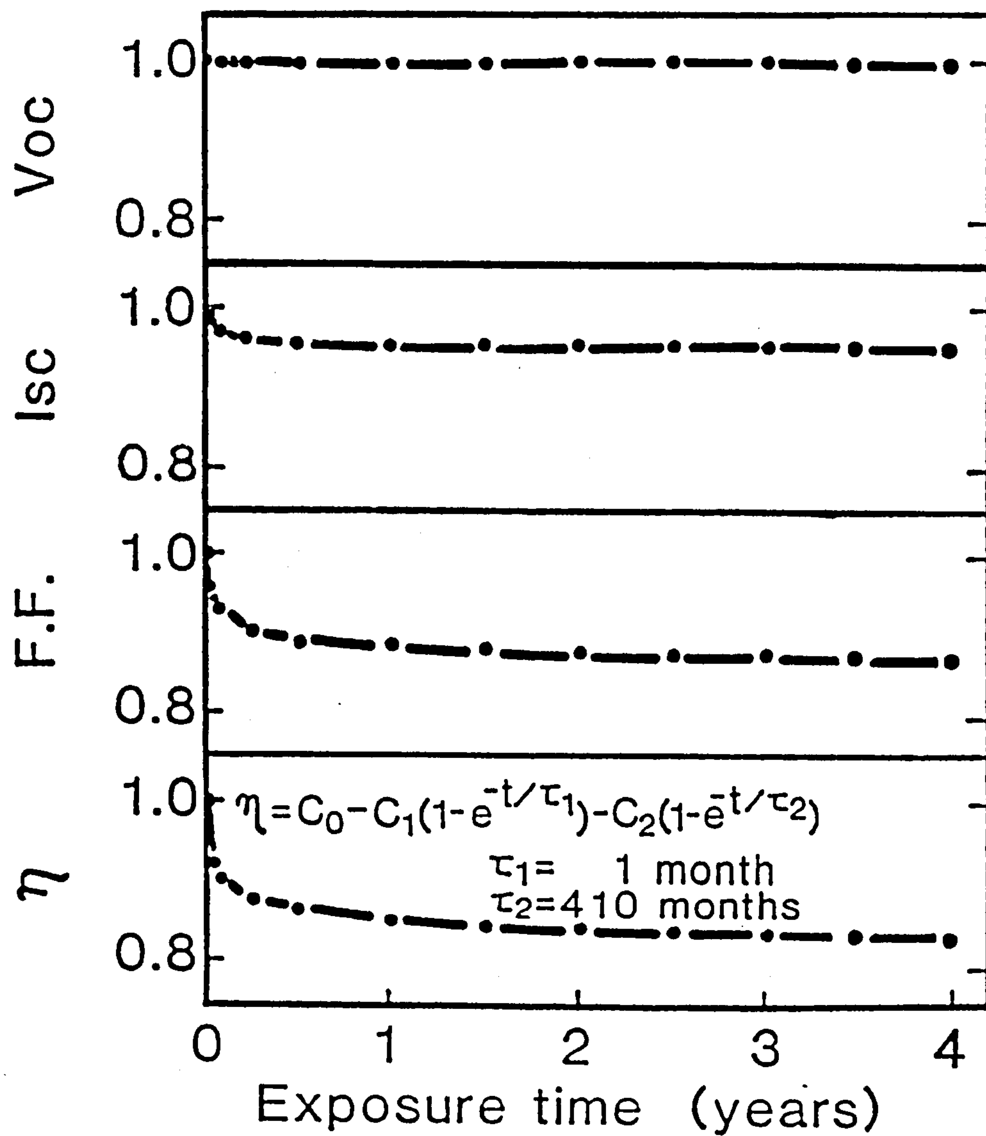

Fig. 6-5 The degradation of the output performance for a 2-kW a-Si power generating system

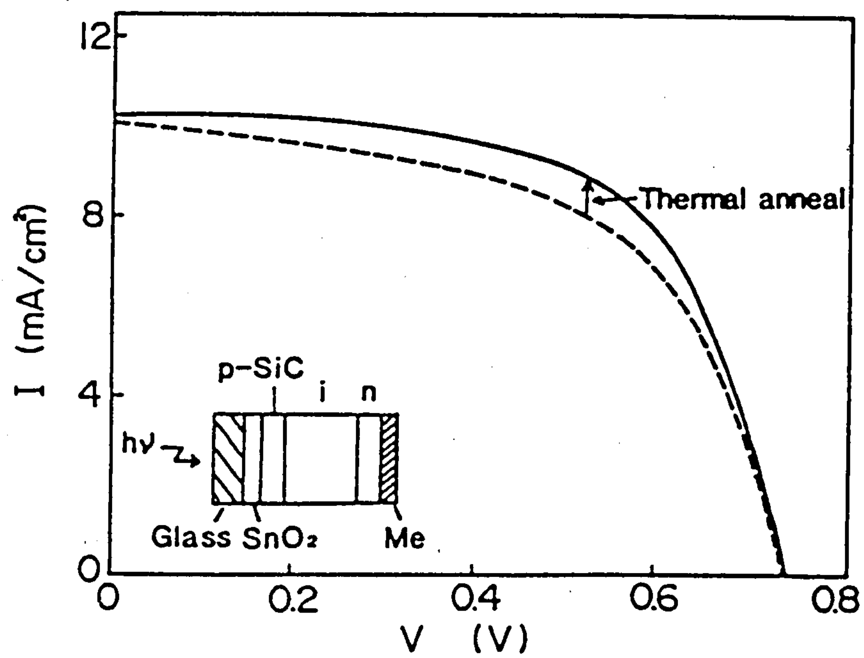

Fig. 6-6. Illuminated I-V characteristics of a p-i-n a-Si cell before (——) and after (----) light exposure at AM1 (100 mW cm^{-2}) for 25 hours.

difference, we measured the collection efficiency and found no change in it, as shown in Fig. 6-7. The change in F.F. is thought to be related with a change in junction properties.

In order to analyse the degradation of the fill factor, the dark I-V characteristics of the cell were investigated. As shown in Fig. 6-8, the shunt current density increased from 10^{-9} to 10^{-5} A/cm^2 and the diode quality factor increased from 1.52 to 2.87 after light exposure. It is believed that these results depend on a change in the current transport mechanism and that the recombination current dominates in this process. The I-V characteristics in the high bias region did not change significantly before and after exposure, and the change in the series resistance was small. Hence, it is supposed that the decrease in the fill factor depends on changes in the junction properties, which cause the increase in the diode quality factor, rather than on the change in the series resistance. In order to confirm this, the dark capacitance-voltage (C-V) characteristics were measured. The frequency dependence of the dark C-V characteristics before and after exposure is shown in Fig. 6-9. As the frequency decreases, the change in capacitance by light exposure increases. In the case of low frequency, increases in capacitance are thought to come from an increase in density of ionized defects of deep level. It is supposed that the defects caused by light exposure cannot respond at a frequency of 100 kHz, because there is no difference in the characteristic before and after exposure at 100 kHz.

As mentioned above, it became clear that the changes in the characteristics of the a-Si pin cell caused by light exposure depend mainly on changes in the junction properties. As the junction properties are affected by internal electric field, the degradation characteristics are thought to be influenced by the thickness W of the i layer. As shown

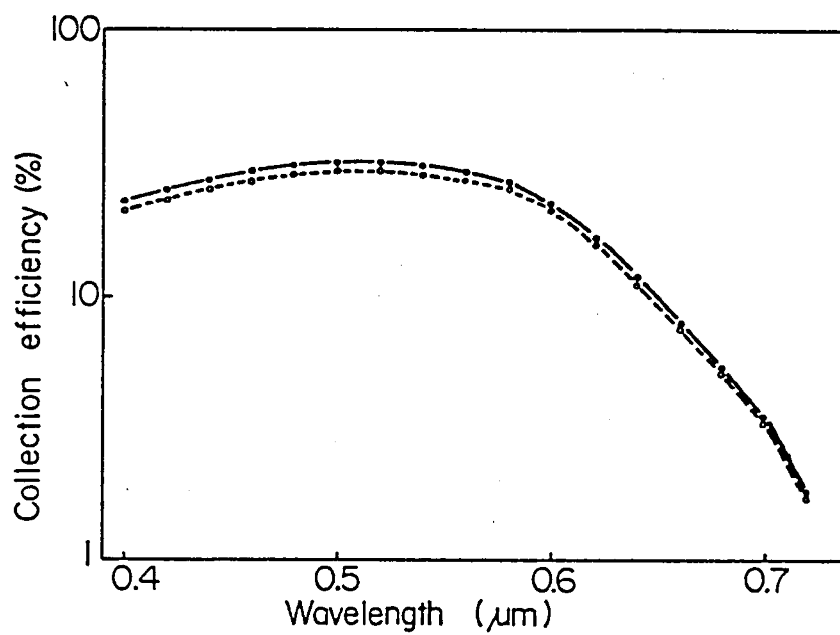

Fig. 6-7. Collection efficiency spectra of a pin a-Si solar cell before (——) and after (----) light exposure.

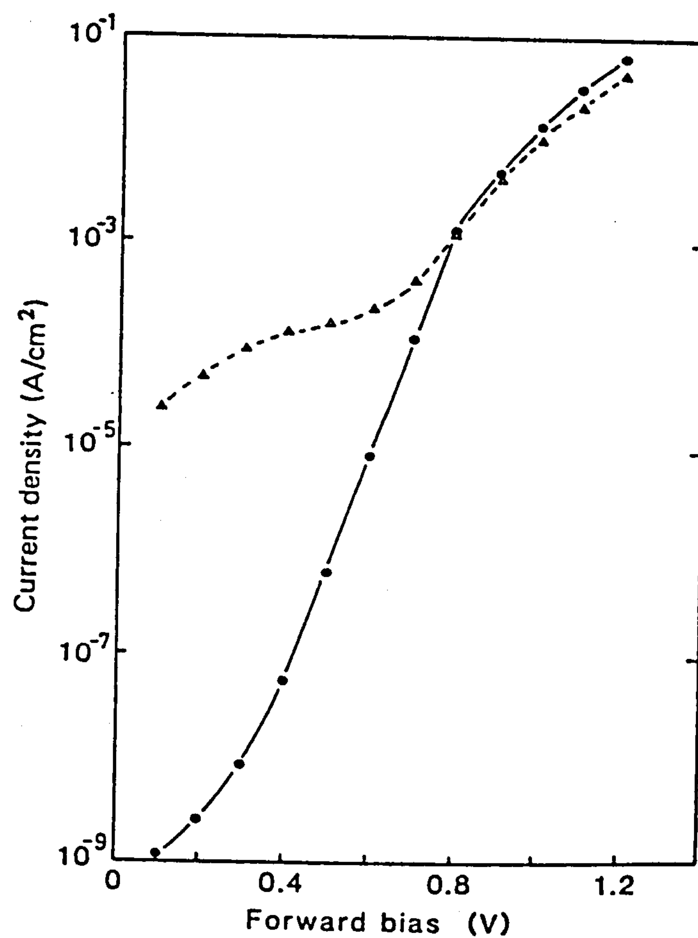

Fig. 6-8. Dark I-V characteristics of the p-i-n cell before (●, n=1.52) and after (▲, n=2.87) light exposure. (n is the diode quality factor.)

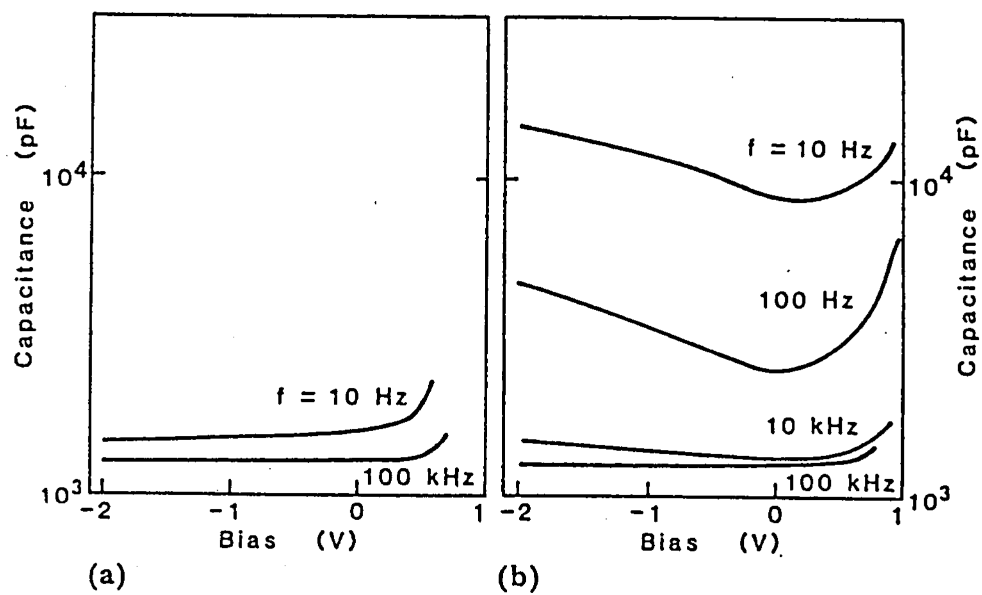

Fig. 6-9. Frequency dependence of the C-V characteristics of the p-i-n a-Si solar cells (a) before (T=296 K) and (b) after light exposure.

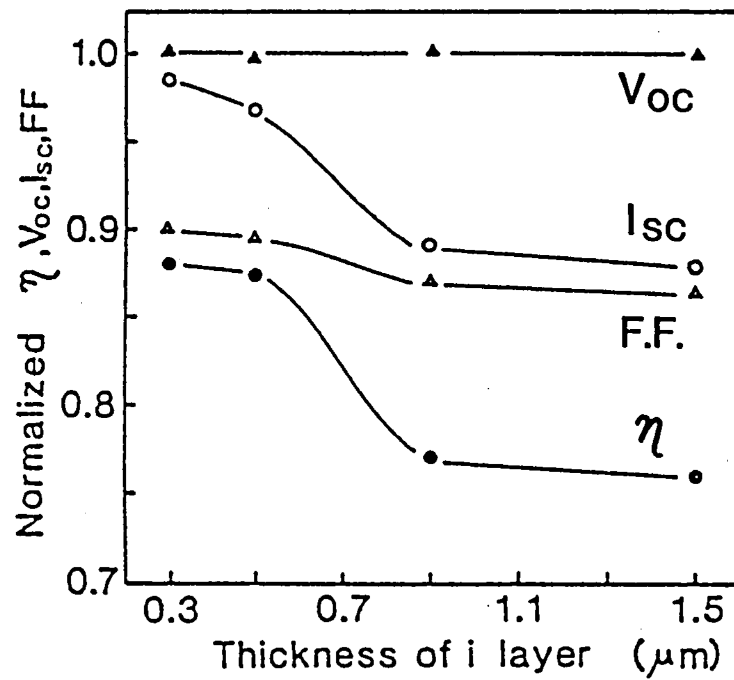

Fig. 6-10. Degradation ratios of the photovoltaic characteristics as functions of i layer thikness (after exposure).

in Fig. 6-10, the degradation of V_{oc} and FF depends slightly on W. In contrast, as W increases, the degradation of I_{sc} is mainly due to the decrease in the collection efficiency in the short-wavelength region. It is believed that this decrease is due to an increase in the size of the low electric field region in the cell, which is caused by shrinkage of the depletion layer, due to the increase in density of ionized defect mentioned before.

The degradation of the photovoltaic characteristics as a function of bias voltage during light exposure was investigated, as shown in Fig. 6-11. The exposure condition was the same as that in the previous experiment shown in Fig. 6-6. A reverse bias caused a decrease in degradation, and forward bias caused an increase in degradation. As this tendency is thought to be related with carrier injection, degradation by the carrier injection was studied in the dark condition. A degradation of 20 % in conversion efficiency was observed after applying a forward voltage of 2 V for 2 hours in the dark condition.

These results show that the degradation is influenced by the amount of carrier recombination. In the reverse bias condition, the internal electric field was strong and the amount of recombination was small. In the forward bias condition the amount of recombination, including the recombination of injected carriers, was large. Thus carrier recombination was thought to create some new carrier traps.

As for the reduction of the light-induced degradation in a-Si solar cells, increase in the internal electric field is effective, because it decreases the carrier recombination. From this viewpoint, the multi-bandgap cell structure is hopeful because the average thickness of the i-layers is small compared with the single-bandgap cell structure.

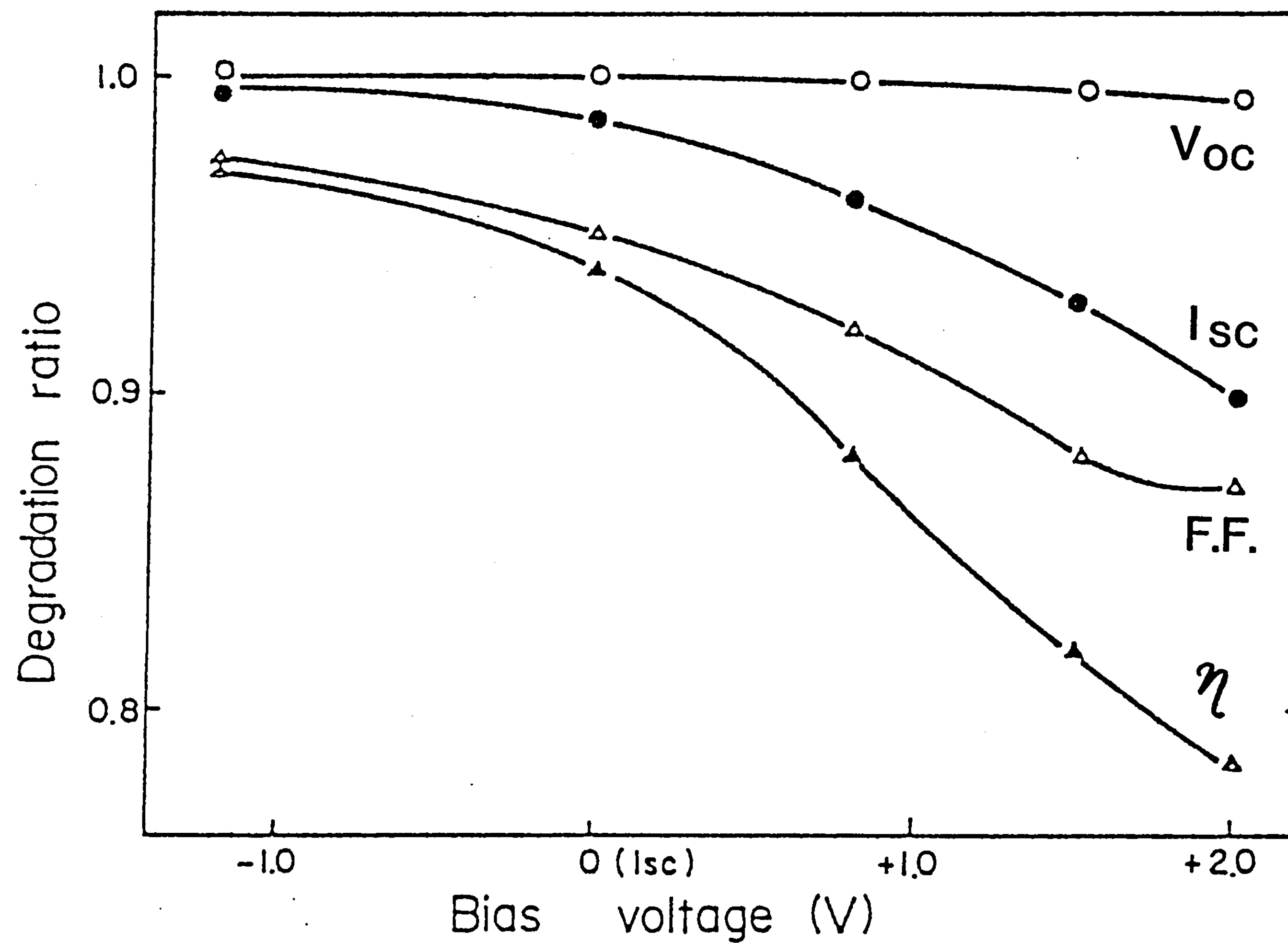

Fig. 6-11. Degradation ratios of the photovoltaic characteristics as functions of the bias voltage. The point of bias voltage of 0 V corresponds to the short circuit condition.

6-4. Effect of Impurities

Changes in the space charge density (N_I) of an Au/a-Si:H/n^+ c-Si Schottky diode were measured by the low-frequency (0.01 Hz) C-V method. The initial values of the space charge density (N_I) and the final value of the increase in N_I by light exposure (N_o) are shown in Fig. 6-12(a), as a function of oxygen concentration. In the figure, ΔN_I means the change in N_I by light exposure. In this experiment, the nitrogen concentration in a-Si films was constant. N_I increased as the oxygen concentration in a-Si films increased with a slope of 1/2. Because N_o increased in the low oxygen concentration region, it can be seen that the oxygen atoms accelerate the light-induced effect in a-Si films. In the high oxygen concentration region, the decrease in N_o with the increase in oxygen concentration seems to be due to a change in Si network caused by excess oxygen.

Nitrogen also had a strong influence on the film properties and light-induced effect, as shown in Fig. 6-12(b). N_I increased in proportion to the square root of the nitrogen concentration in the a-Si films. This result can be explained by the law of mass action[7], the same as in the case of phosphorus doping. Namely, in phosphorus doping, Street proposed a following reaction,[7]

$$P_3 + T_4 \rightleftarrows P_4^+ + D^- \qquad (6\text{-}1)$$

where P_3, T_4, P_4^+, and D^- mean 3-fold coordinated phosphour, 4-fold coordinated silicon, 4-fold coordinated phosphour with a positive charge, and silicon with a dangling bond of a negative charge, respectively. In the case of nitrogen, following equation can be derived,

$$\begin{array}{cc} N_3 + T_4 & \rightleftarrows \; N_4^+ + D^- \\ (N_N - n)(N_{Si}) & (n)(n) \end{array} \qquad (6\text{-}2)$$

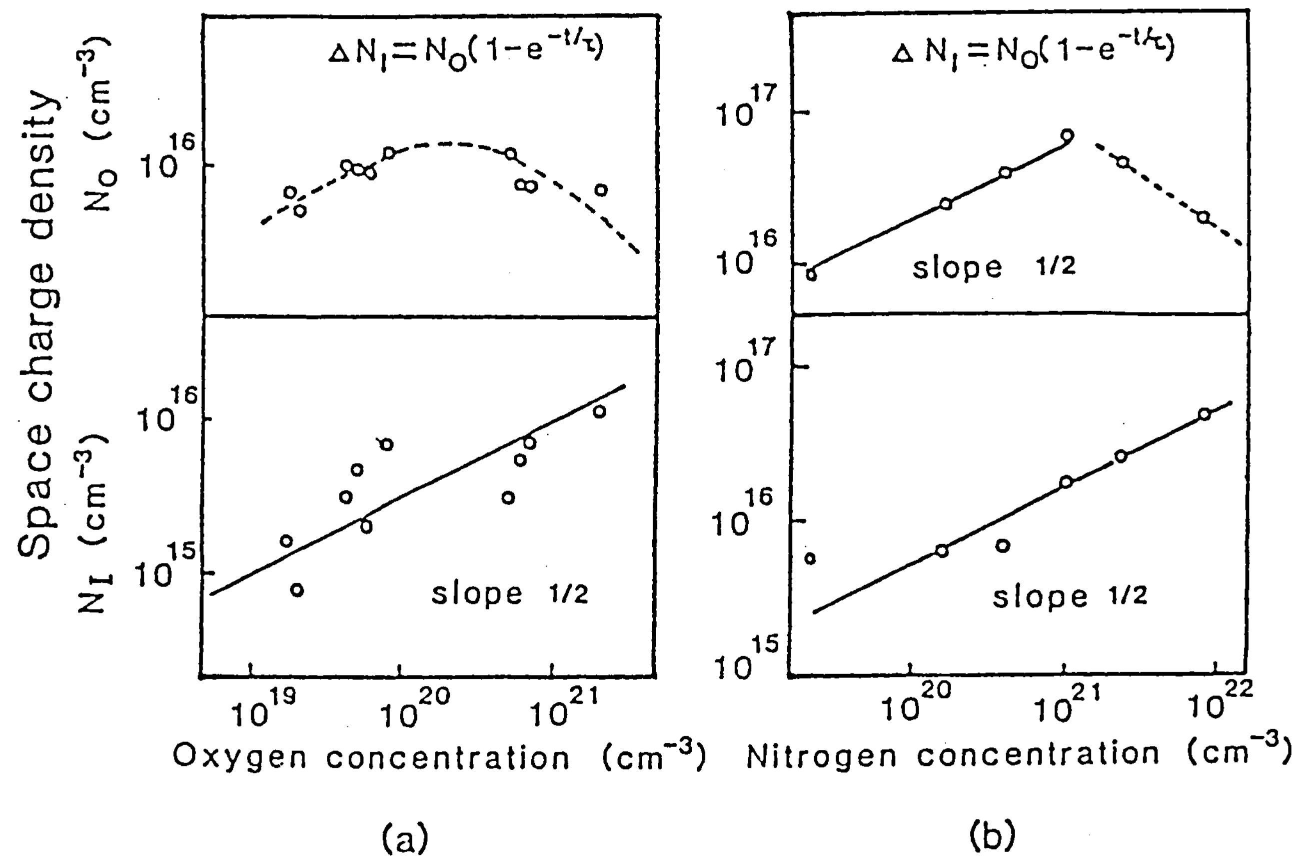

Fig. 6-12. The chages in the N_I and N_o as functions of the nitrogen and oxgen concentration.

Where N_3, N_4, N_N, N_{Si}, and n mean 3-fold coordinated nitrogen, 4-fold coordinated nitrogen with a positive charge, number of nitrogen atoms, number of silicon atoms, and number of N_4 which is equal to number of D , respectively. From the lower part of eq. (6-2), which shows a quantiative relation, following equation is derived,

$$\frac{N_{Si}\,(N_N - n)}{n \times n} = \text{const.} \tag{6-3}$$

Assuming $N_{Si} \gg N_N \gg n$, eq. (6-3) becomes

$$\frac{N_N}{n \times n} = \text{const.} \tag{6-4}$$

Then it is clear that n is proportional to the square root of N_N. In the case of oxygen, the slope of N_0 is a little larger than 1/2, but the tendency is similar. In the both cases, the decrease in N_0 may come from the assumption of $N_{Si} \gg N_N$ (or N_{ox}) $\gg$ n, where N_{ox} means number of oxygen atoms.

Figure 6-12 shows that there is a strong influence of the light-induced effect on impurities in a concentration region of more than 10^{19} cm^{-3}. Then, the light-induced effect in a-Si films with low impurity concentration, deposited in the super chamber, is discussed.

As the photoconductivity of a-Si films strongly affects the performance of a-Si solar cells, it is mainly discussed in the following study. The degradation ratio of the photoconductivity (σ_{ph}/σ_{pho}) as a function of the oxygen concentration is shown in the lower part of Fig. 6-13, where σ_{pho} and σ_{ph} signify the photoconductivity before and after light exposure, respectively. Samples were exposed to AM-1 light (500 mW/cm^{-2}) for 5 hours. When the oxygen concentration decreased from 10^{19} cm^{-3} to 10^{18} cm^{-3}, the degradation ratio of the photoconductivity

decreased to about 1/3. This result implies that the light-induced effect can be reduced through a reduction of the impurities with the super chamber.

On the other hand, the ESR spin density after light exposure did not depend on the oxygen concentrations, as shown in the upper part of Fig. 6-13. This behavior is consistent with Tsai's results.[8] However, from the result of photoconductivity, it is considered that the light-induced effect cannot be estimated only by the spin density. Indeed, a change in the capture cross section of carriers has been reported,[9] and a difference between the light-induced effect on the photoconductivity and that on the ESR spin density is thought to come from a change in capture cross section or from the energy level of defects created by light exposure, because the photoconductivity is influenced by the capture cross section and the energy level of defects.

In the ESR measurement, one can only estimate the density of dangling bonds of electrically neutral. As for charged states, oxygen is thought to cause an increase in the space charge density after light exposure. Therefore, there is a possibility that oxygen causes an increase in the ionized dangling bonds, such as D^+ (positively charged) and D^- (negatively charged), which may influence the value of the photoconductivity shown in Fig. 6-13.

The increase in the ESR spin density after light exposure is thought to come from bond breaking of weak Si-Si bonds.[11] As mentioned above, carrier recombination causes light-induced degradation, therefore, it supplies some energy to break weak Si-Si bonds. The origin of weak Si-Si bonds is not clear, but impurities, such as oxygen and nitrogen, are thought to be a candidate for the origin. In fact, as described in Chapter II, reduction of impurities decreases the density of tail states,

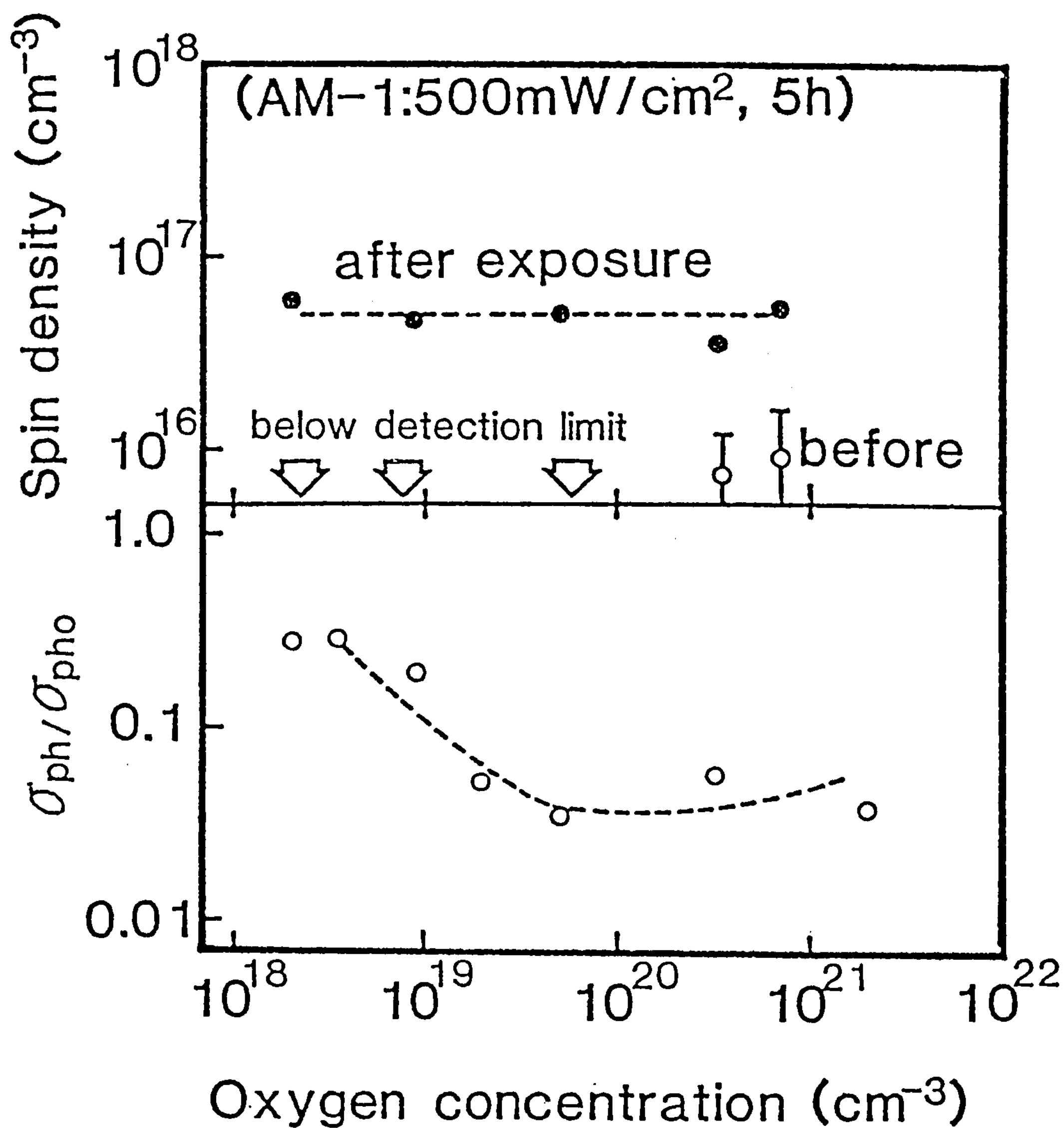

Fig. 6-13. ESR spin density and normalized photoconductivity (σ_{ph}/σ_{d}) as functions oxygen concentrations in a-Si films.

which suggests change in Si network.

The effect of impurity reduction on the light-induced degradation of solar cell performance was also investigated. It was found that the degradation ratio of the conversion efficiency of a-Si solar cells by light exposure can be reduced from 23 % to 12 % by the reduction of oxygen concentration from 1.8×10^{20} cm^{-3} to 1.8×10^{19} cm^{-3}.[10)]

In conclusion, reduction of impurities, which can be achieved by the super chamber method as described in Chapter II, is one of the effective methods for the prevention of the light-induced degradation in a-Si films.

6-5. Summary

Reliability of a-Si solar cells was studied and a 10 % decrease in conversion efficiency was observed at the initial period of one month. Then the light-induced degradation of a-Si solar cells was systematically investigated, and it was found that the degradation ratio increases with the increase in the i-layer thickness which corresponds to the decrease in internal electric field. It was also found that the degradation is accelerated by the carrier injection with the forward bias voltage in the dark. As both the decrease in the internal electric field and the increase in the carrier injection cause the increase in carrier recombination, these results show that the carrier recombination causes the degradation. It was suggested that the multi-bandgap cell structure is effective for the prevention of the light-induced degradation of a-Si solar cells. Concerning the a-Si film itself, the effect of impurities was studied. It was shown that the reduction of impurities by the super chamber method is effective for the prevention of the light-induced effect of a-Si films.

References

1) S. Tsuda, T. Takahama, M. Isomura, H. Tarui, Y. Nakashima, Y. Hishikawa, N. Nakamura, T. Matsuoka, T. Fukatsu, M. Ohnishi, S. Nakano and Y. Kuwano : Jpn. J. Appl. Phys. 26 (1987) 33.

2) Y. Kuwano, M. Ohnishi, S. Nakano, T. Fukatsu, H. Nishiwaki and S. Tsuda : Proc. 4th E. C. Photovoltaic Solar Energy Conf., Stresa, Italy (D. Reidel Publishing Co., Dordrecht, 1982) p.704.

3) D. L. Staebler and C. R. Wronski : Appl. Phys. Lett. 31 (1977) 292.

4) D. L. Staebler, R. S. Crandall and R. Williams : Appl. Phys. Lett. 39 (1981) 733.

5) Y. Kuwano, M. Ohnishi, S. Tsuda, Y. Nakashima and N. Nakamura : Jpn. J. Appl. Phys., 21(1982) 413.

6) Y. Kuwano, S. Tsuda, M. Ohnishi, H. Nishiwaki, H. Shibuya, S. Nakano and T. Imai : Jpn. J. Appl. Phys., Suppl. 2, 20(1981) p.213.

7) R. A. Street : Phys. Rev. Lett. 49 (1982) 1187.

8) C. C. Tsai, M. Stutzmann and W. B. Jackson : AIP Conf. Proc. No. 120 (Am. Inst. Phys., New York, 1984) p.242.

9) N. Nakamura, S. Tsuda, T. Takahama, M. Nishikuni, K. Watanabe, M. Ohnishi and Y. Kuwano : AIP Conf. Proc. No. 120 (Am. Inst. Phys., New York, 1984) p.303.

10) S. Tsuda, N. Nakamura, K. Watanabe, M. Nishikuni, M. Ohnishi, S. Nakano, Y. Kishi, H. Shibuya and Y. Kuwano : Tech. Digest Int'l PVSEC-1, Kobe, Japan (1984) p.213.

11) M. Stutzmann : AIP Conf. Proc. No. 157 (AM. Inst. Phys., New York, 1987) p.235.

VII. CONCLUSIONS

In this thesis, a series of systematic studies has been made to improve the performance of amorphous silicon (a-Si) solar cells through the approaches of fabrication process, materials, and cell structures.

Concerning the fabrication process, a separated UHV (ultra-high vacuum) reaction chamber, called a super chamber, has been newly developed to improve the properties of a-Si films by the reduction of impurities. As for materials, super structure a-SiC/a-Si films were fabricated by the photo-CVD method for the first time, as a high-quality wide-bandgap material which improves the short-wavelength collection efficiency. Also concerning materials, hydrogenated-and-fluorinated amorphous silicon germanium (a-SiGe:H:F) was systematically investigated as a high-quality narrow-bandgap material which improves the long-wavelength collection efficiency. As for cell structures, theoretical considerations were made on amorphous solar cells, especially on the multi-bandgap cells, which combine a wide-bandgap material and a narrow-bandgap material. With regard to reliability, the origin of light-induced degradation in a-Si films was discussed, and the multi-bandgap cell structure and impurity reduction by the super chamber were indicated as effective methods of preventing the degradation.

In Chapter II, properties of a-Si films and solar cells fabricated by the super chamber were studied. A background pressure of 10^{-9} Torr, which is two to three orders of magnitude lower than that obtained with a conventional separated reaction chamber, was achieved, and a gas leakage level of 10^{-7} Torr l/sec was also achieved. Exhausted gases were investigated with GMA (gas mass analyzer), and there were no signs of N_2, H_2O and so on, which did appear in the GMA spectra of the conventional

chamber. The a-Si films deposited in the super chamber were systematically studied. Impurity concentrations of oxygen, nitrogen, and carbon measured by an ion microanalyzer were 2×10^{18} cm^{-3}, 1×10^{17} cm^{-3}, and 2×10^{18} cm^{-3}, respectively. These values were three to ten times of magnitude lower than these in a-Si films deposited with the conventional separated reaction chamber. The ESR spin density and the hole diffusion length of a-Si films deposited in the super chamber were 2×10^{15} cm^{-3} and 1 μm, respectively, which were about two times as good as those of a-Si films deposited in the conventional separated reaction chamber. A conversion efficiency of 11.7 % was obtained for an a-Si solar cell fabricated with the super chamber method.

In Chapter III, a-Si/a-SiC super structure films prepared with the photo-CVD method for the first time were investigated as a new wide-bandgap material. The accuracy of the structure of the a-Si/a-SiC super structure film was confirmed by AES and Bragg reflection of X-ray. The thickness fluctuation of the interfaces of the film was estimated to be 7 Å. The quantization effect was observed in the dependence of the optical bandgap and the B-value on the thickness of the well layer. It was found that the photoluminescence intensity of super structure films prepared with the photo-CVD method was about four times larger than that of similar films prepared with the glow discharge method. It shows the superiority of the photo-CVD method for the preparation of super structure films compared with the glow discharge method. The carrier transport mechanism vertical to the interfaces of the super structure film was thought to be mainly tunneling transport in dark from I-V characteristics. A new type of solar cells using the super structure as the p-layer has also been developed for the first time. A remarkable increase in the collection efficiency in the short wavelength region was

observed, and a conversion efficiency of 10.5 % was obtained for a glass/TCO/p-super structure/in/metal/a-Si solar cell.

In Chapter IV, a-SiGe:H:F films were systematically investigated as a high-quality narrow-bandgap material. Microcrystalline-Ge can be obtained when the ratio of the gas flow rate $GeF_4/(SiF_4 + GeF_4)$ is more than 0.7 %; μc-Si can be observed in a-SiGe when substrate temperature T_s is more than 220 °C. As for the optimum reaction condition, T_s is 180 °C and the composition ratio of Si and Ge is 0.4:0.6. Using the optimum reaction condition, a rectification ratio greater than 10^7 was obtained for an a-SiGe:H:F Schottky diode at a bias of 1 V. A collection efficiency of 32 % was obtained at a wavelength of 800 nm with a p(a-SiC:H)-i(a-SiGe:H:F)- n(a-Si:H) diode.

In Chapter V, theoretical considerations were made concerning the multi-bandgap a-Si solar cell, which combines a wide-bandgap material and a narrow-bandgap material. The theoretical efficiencies of single-junction, two-junction, and three-junction amorphous solar cells were calculated, and each optical bandgap E_{opt} of the multi-bandgap amorphous solar cells was optimized. It was shown that a theoretical efficiency of 24 % can be obtained with a multi-bandgap cell which has E_{opt} of 2.0 eV, 1.7 eV and 1.45 eV.

In Chapter VI, changes in the characteristics of a-Si solar cells caused by light exposure were studied. The degradation of the conversion efficiency of pin a-Si solar cells caused by light exposure depends on the thickness of the i layer. As the thickness of the i layer is increased, the collection efficiency in the short-wavelength region decreases and the short circuit current density decreases, and the conversion efficiency decreases with light exposure. A decrease in the fill factor was commonly observed, and in such cases the n value and the

shunt current density increased, which suggested a change in junction properties. The light-induced degradation of the photoconductivity of a-Si films deposited in the super chamber was much smaller than that of a-Si films deposited in the conventional chamber. This result indicates that the light-induced effect has a strong correlation with impurities, such as oxygen and nitrogen, in a-Si films. As effective countermeasures of the light-induced effect at present, reduction of impurities by the super chamber and applying the multi-bandgap cell structure were proposed, which are also effective for improving performance.

APPENDIX A FERMI INTEGRAL

In this appendix, derivation of eq.(5-9) in Chapter V is explained.

For the first term of eq.(5-8), the Fermi integral of eq.(5-5) can be written as follows:

$$P_1^+ = \int_{-\infty}^{\infty} \frac{g_{min1} \exp(-\varepsilon/UE_{01})}{1+\exp\{((\varepsilon_f-\phi)-\varepsilon)/kT\}} \, d\varepsilon$$

$$= g_{min1} \int_{-\infty}^{\infty} \frac{\exp(-a\varepsilon)}{1+c\cdot\exp(-b\varepsilon)} \, d\varepsilon \tag{A-1}$$

where

$$a = \frac{1}{UE_{01}}, \quad b = \frac{1}{kT}, \quad c = \exp\frac{\varepsilon_f-\phi}{kT}$$

Then

$$P_1^+ = \frac{g_{min1}}{a} \int_{-\infty}^{\infty} \frac{dx}{1+c\cdot x^{-b/a}} \qquad (x=\exp(-a\varepsilon))$$

$$= \frac{g_{min1}}{a\,c^{a/b}} \int_{-\infty}^{\infty} \frac{dz}{1+z^d} \qquad (z = x\cdot c^{a/b}) \quad (d=b/a) \tag{A-2}$$

Equation (A-2) is one of the Mellin transformation integrals, where the general form of the Mellin transformation integral is as follows:

$$\int_0^{\infty} x^{\alpha-1} F(x) \, dx$$

In the case of eq.(A-2), $\alpha = 1$ and $F(x) = (1 + x^d)^{-1}$, then the solution of eq.(A-2) can be written as follows:

$$P_1^+ = \frac{g_{min}}{a\,c^{a/b}} \cdot \frac{\pi}{d} \operatorname{cosec} \frac{a\pi}{b}$$

$$= g_{min1}\, kT\pi \frac{\exp\left(\frac{\phi-\varepsilon_f}{UE_{01}}\right)}{\sin\left(\frac{kT}{UE_{01}}\pi\right)} \tag{A-3}$$

For the second term of eq.(5-8) and both terms of eq.(5-7), they can be calculated on the analogy of the calculation from eq.(A-1) to eq.(A-3). Considering the band bending $\Delta \varepsilon$, finally, eq.(5-9) can be derived.

APPENDIX B STEP-BY-STEP METHOD

Here, step-by-step method for determination of potential energy distribution is explained.

Poisson's equation, as presented in eq.(5-10) of Chapter V, can be expressed by polynominal expansion as follows,

$$\Delta \psi = \frac{e}{\varepsilon \varepsilon_0} \left(\frac{1}{2} \rho_n \Delta x_n^2 + \Delta x_n \sum_{i}^{n-1} \rho i \Delta x i \right) \qquad \text{(B-1)}$$

Where $\Delta \psi$ means energy intervals into which potential energy ψ is equally divided, and Δx_n and ρ_n mean nth distance and electric charge, respectively, as shown in Fig. B-1. In the step-by-step method, first, the initial slope $\Delta \psi / \Delta x_1$, is assumed, and then second distance Δx_2 is calculated by eq.(B-1). This procedure is continued until whole potential energy distribution is obtained. The advantage of this method is that an analytical equation is not required for electric charge. But there is some ambiguity to set the initial value of $\Delta \psi / \Delta x_1$, which may cause some error in the result.

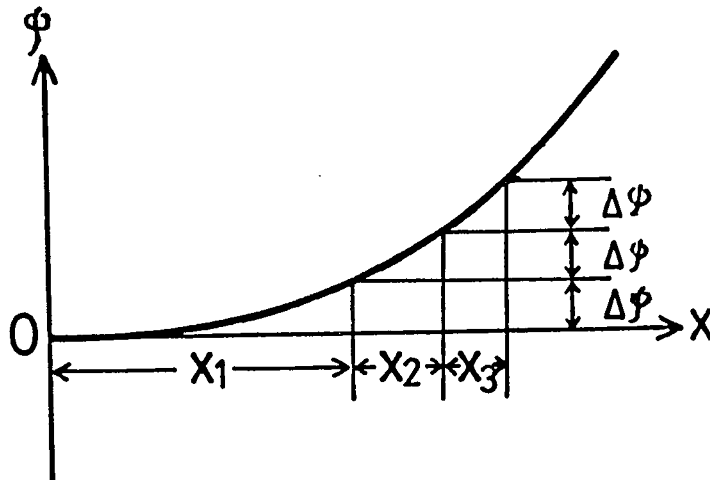

Fig. B-1 Principle of step-by-step method.

APPENDIX C SOLUTION OF CONTINUITY EQUATION

In this appendix, derivations of eqs.(5-15), (5-16) and (5-17) in Chapter V are explained.

Assuming the absence of rear reflection, absorbed photon density N_{s1} in the surface depletion region of the width W_s in Fig. 5-5 can be written as follows:

$$N_{s1}(\lambda)=N_{in}(\lambda)[1-\exp\{-\alpha(\lambda)W_s\}] \qquad \text{(C-1)}$$

where $N_{in}(\lambda)$ and $\alpha(\lambda)$ are incident photon density and absorption coefficient of a-Si, respectively. Then assuming that the rear reflection coefficient is unity and that only one reflection occurs at the rear surface, absorbed photon density $N_{s2}(N)$ in W_s for reflected photons at the rear surface can be written as follows:

$$\begin{aligned} N_{s2}(\lambda) &= N_{in}(\lambda)\exp\{-\alpha(\lambda)(W_s+W_n+W_b)\}\cdot\exp\{-\alpha(\lambda)(W_n+W_b)\} \\ &\quad \cdot[1-\exp\{-\alpha(\lambda)W_s\}] \\ &= N_{in}(\lambda)\exp\{-\alpha(\lambda)(W_s+2W_n+2W_n)\} \\ &\quad \cdot[1-\exp\{-\alpha(\lambda)W_s\}] \end{aligned} \qquad \text{(C-2)}$$

where W_n and W_b are widths of neutral region and rear depletion region in Fig. 5-5, respectively. Then, with the above mentioned assumptions, total absorbed photon density N_s can be written as follows:

$$\begin{aligned} N_s=\int\{N_{s1}(\lambda)+N_{s2}(\lambda)\}d\lambda=\int & N_{in}(\lambda)[1+\exp\{-\alpha(\lambda)(W_s+2W_n+2W_b)\}] \\ & \times[1-\exp\{-\alpha(\lambda)W_s\}]d\lambda \end{aligned} \qquad \text{(C-3)}$$

On the analogy of the calculation for $N_s(\lambda)$, total absorbed photon density N_b in W_b can be written as follows.

$$N_b = \int N_{in}(\lambda)\ \exp\{-\alpha(\lambda)(W_s+W_b)\}[1+\exp\{-\alpha(\lambda)W_b\}] \times [1-\exp\{-\alpha(\lambda)W_b\}]\, d\lambda \tag{C-4}$$

As carrier recombination in the regions of W_s and W_b can be neglected, eqs.(5-15) and (5-17) can be derived by multipling e by eqs.(C-3) and (C-4), respectively, where e is electron charge.

In the region of W_n, one must consider the carrier recombination. Steady state continuity equation for minority carriers (holes) can be written as follows:

$$D_p \frac{d^2n}{dx^2} - \frac{n}{\tau_p} + g(\lambda, x) = 0 \tag{C-5}$$

where D_p, n, τ_p are diffusion coefficient, carrier density, and life time of holes, respectively. Assuming that generation probability is unity, the generation term $g(\lambda, x)$ for the region between x to x + dx can be written as follows:

$$g(\lambda, x) = \frac{d}{dx}\{N_{n1}(\lambda, x) + N_{n2}(\lambda, x)\} \tag{C-6}$$

where $N_{n1}(\lambda, x)$ and $N_{n2}(\lambda, x)$ are absorbed photon densities at position x for the absence of rear reflection and for reflected photons at the rear surface, respectively. On the analogy of the calculations for $N_{s1}(\lambda)$ and $N_{s2}(\lambda)$, $N_{n1}(\lambda, x)$ and $N_{n2}(\lambda, x)$ can be written as follows:

$$N_{n1}(\lambda, x) = N_{in}(\lambda)\ \exp\{-\alpha(\lambda)W_s\}\ \exp\{-\alpha(\lambda)\cdot x\} \tag{C-7}$$

$$N_{n2}(\lambda, x) = N_{in}(\lambda)\ \exp\{-\alpha(\lambda)(W_s+W_n+2W_b)\} \times \exp\{-\alpha(\lambda)(W_n - x)\} \tag{C-8}$$

From eqs.(C-6), (C-7) and (C-8), $g(\lambda, x)$ can be expressed as follows:

$$g(\lambda,x)=N_{in}(\lambda)\ \alpha(\lambda)\ \exp\{-\alpha(\lambda)W_S\}\,[\exp-\alpha(\lambda)x + \exp\{-2\alpha(\lambda)(W_n+W_b)\}\cdot\exp\{\alpha(\lambda)x\}] \qquad \text{(C-9)}$$

Boundary conditions for eq.(C-5) are assumed as follows:

$$n\,|_{x=0} = 0 \qquad \text{(C-10)}$$

$$D_p \frac{dn}{dx}\Big|_{x=Ws} = S\cdot n\Big|_{x=Ws} \qquad \text{(C-11)}$$

where S means surface recombination velocity at $x = W_s$. A genaral solution for eq.(C-5) with eq.(C-9) can be written as follows:

$$n = A_{\cosh}\left(\frac{x}{Lp}\right) + B_{\sinh}\left(\frac{x}{Lp}\right) - \frac{\alpha F\tau}{\alpha^2 Lp^2 - 1}[\,\mathrm{exg}\{-\alpha(\lambda)x\} + C\ \exp\{-\alpha(\lambda)x\}\,] \qquad \text{(C-12)}$$

where A and B are integral constants, and $L_p(=\sqrt{D_p\tau_p})$ is diffusion length. F and C in eq.(C-12) can be written as follows:

$$C=\exp\{-2\alpha(\lambda)(W_n+W_b)\} \qquad \text{(C-13)}$$

$$F = N_{in}(\lambda)\alpha(\lambda)\ \exp\{-\alpha(\lambda)W_S\} \qquad \text{(C-14)}$$

From eqs.(C-10), (C-11), and (C-12), A and B can be determined, and eq.(5-16) can be derived from a following equation.

$$I_n(V)=\int\left(qD_p\frac{dn}{dx}\Big|_{x=0}\right)d\lambda \qquad \text{(C-15)}$$

APPENDIX D EXPLANATION OF PHOTOCURRENTS

In this appendix, meanings of eqs.(5-25), (5-26), and (5-27) in Chapter V are explained.

Equation (5-25) is re-written as follows:

$$i_{ph_1} = \int_{\lambda_0}^{\lambda_1} I_a(\lambda)\{1 - e^{-\alpha_1(\lambda)W_1}\}\ \eta_1(\lambda)\ d\lambda \tag{D-1}$$

In this equation, $I_a(\lambda)$ is expressed by eq.(5-19), and the term $\{1 - e^{-\alpha_1(\lambda)W_1}\}$ means a ratio of absorbed photon density to incident phton density in the first cell of a multi-bandgap structure shown in Fig. 5-8 (b). $\eta_1(\lambda)$ is quatum efficiency of the first cell.

$$i_{ph_2} = \int_{\lambda_0}^{\lambda_1} I_a(\lambda)\{1 - e^{-\alpha_2(\lambda)W_2}\}\ e^{-\alpha_2(\lambda)W_2}\ \eta_2(\lambda)\ d\lambda \tag{D-2}$$

In this equation, each term can be explained on the analogy of eq.(D-1), except for the term $-e^{-\alpha_2(\lambda)W_1}$ which means absorbed photon density in the first cell.

Equation (5-27) can be also explained on the analogy of eq.(D-2).

APPENDIX E NEWTON METHOD FOR CALCULATION OF I-V CHARACTERISTICS

In this appendix, the Newton method which is used in the calculation of I-V characteristics in Chapter V is explained.

The illuminated I-V characteristics of solar cells can be written as follows (from eqs.(5-1), (5-2) and (5-3)):

$$I = I_{ph} - I_o \{\exp \frac{q(V+IR_S)}{nkT} - 1\} - \frac{V+IR_S}{Rsh} \qquad \text{(E-1)}$$

Basic equation for the Newton method can be written as follows:

$$I_{n+1} = I_n - \frac{f(I)}{f'(I)} \qquad \text{(E-2)}$$

where

$$f(I) = I_{ph} - I_o \{\exp \frac{q(V+IR_S)}{nkT} - 1\} - \frac{V+IR_S}{Rsh} - I \qquad \text{(E-3)}$$

$$f'(I) = \frac{q}{nkT} \; I_o R_S \exp \frac{q(V+IR_S)}{nkT} - \frac{R_S}{Rsh} - 1 \qquad \text{(E-4)}$$

In the calculation of I-V characteristics, first, an initial value of I(= I_0; n = 0) is set, then the next value of I_1(n = 0+1), which is closer to the solution than I_0 can be calculated with eq.(E-2). This produce is repeated until $|I_{n+1} - I_n| < 1/1000 \cdot I_n$.

LIST OF PUBLICATION

I. Full Papers

1) S. Tsuda, N. Nakamura, K. Watanabe, T. Takahama, H. Nishiwaki, M, Ohnishi and Y. Kuwano : Solar Cells 9 (1983) 25.

2) S. Tsuda, H. Tarui, H. Haku, H. Dojyo, K. Watanabe, Y. Hishikawa, N. Nakamura, Y. Nakashima, T. Takahama, H. Nishiwaki, T. Fukatsu, S. Nakayama, M. Ohnishi, S. Nakano and Y. Kuwano : Jpn. J. Appl. Phys. 25 (1986) 1795.

3) S. Tsuda, H. Tarui, T. Matsuyama, T. Takahama, S. Nakayama, Y. Hishikawa, N. Nakamura, T. Fukatsu, M. Ohnishi, S. Nakano and Y. Kuwano : Jpn. J. Appl. Phys. 26 (1987) 28.

4) S. Tsuda, T. Takahama, M. Isomura, H. Tarui, Y. Nakashima, Y. Hishikawa, N. Nakamura, T. Matsuoka, T. Fukatsu, M. Ohnishi, S. Nakano, and Y, Kuwano : Jpn. J. Appl. Phys. 26 (1987) 33.

II. Conference Proceedings

1) S. Tsuda, N. Nakamura, Y. Nakashima, H. Tarui, H. Nishiwaki, M. Ohnishi and Y. Kuwano : Jpn. J. Appl. Phys. 21 (1982) Suppl. 21-2, p.251.

2) S. Tsuda, H. Tarui, M. Ohnishi, S. Sakai, K. Uchihashi, T. Matsuoka, S. Nakano, S. Kiyama, H. Kawata and Y. Kuwano : J. Non-Crystalline Solids 59&60 (1983) 1135.

3) S. Tsuda, N. Nakamura, K. Watanabe, M. Nishikuni, M. Ohnishi, S. Nakano, Y. Kishi, H. Shibuya and Y. Kuwano : Tech. Digest. Int. PVSEC-1, Kobe, Japan (1984) 213.

4) S. Tsuda, Y. Nakashima, H. Haku, H. Tarui, S. Nakano, M. Ohnishi, Y. Kishi and Y. Kuwano : Proc. Int. Conf. Solar & Wind

Energy Applications (1985) B-p.29.

5) S. Tsuda, H. Tarui, H. Haku, Y. Nakashima, Y. Hishikawa, S. Nakano and Y. Kuwano : J. Non-Crystalline Solids 77&78 (1985) 845.

6) S. Tsuda, N. Nakamura, M. Nishikuni, K. Watanabe, T. Takahama, Y. Hishikawa, M. Ohnishi, Y. Kishi, S. Nakano and Y. Kuwano : J. Non-Crystalline Solids 77&78 (1985) 1465.

7) S. Tsuda, T. Takahama, H. Tarui, K. Watanabe, N. Nakamura, H. Shibuya, S. Nakano, M. Ohnishi, Y. Kishi, Y. Kuwano : Proc. IEEE Photovoltaic Specialists Conf. (1985) 1295.